Stony Brook University

Fenton Chemistry and Disease –

The Role of Particle-Derived Reactive Oxygen Species in Pathogenesis

A Dissertation Presented

by

Andrea Dawn Harrington

to

The Graduate School

in Partial Fulfillment of the

Requirements

for the Degree of

Doctor of Philosophy

in

Geosciences

Stony Brook University

May 2013

Stony Brook University

The Graduate School

Andrea Dawn Harrington

We, the dissertation committee for the above candidate for the

Doctor of Philosophy degree, hereby recommend

acceptance of this dissertation.

Dr. Martin A.A. Schoonen – Dissertation Advisor
Professor, Department of Geosciences

Dr. Styliani-Anna E. Tsirka – Co-Advisor
Professor, Department of Pharmacological Sciences

Dr. Troy Rasbury - Chairperson of Defense
Professor, Department of Geosciences

Dr. Richard J. Reeder
Professor, Department of Geosciences

Dr. Sanford R. Simon
Professor, Departments of Biochemistry and Cell Biology and Pathology

This dissertation is accepted by the Graduate School

Charles Taber
Interim Dean of the Graduate School

Abstract of the Dissertation

Fenton Chemistry and Disease –

The Role of Particle-Derived Reactive Oxygen Species in Pathogenesis

by

Andrea Dawn Harrington

Doctor of Philosophy

in

Geosciences

Stony Brook University

2013

Reactive Oxygen Species (ROS) are vital to the normal functioning of the immune system in the human body. However, when a foreign material enters the system the highly regulated balance between pro- and anti-oxidants can be disrupted, especially if the material itself can generate ROS. One way a material can generate ROS is through Fenton chemistry. The hypothesis that Fenton chemistry is an important factor in many exposure related diseases is experimentally tested using an array of complementary acellular and cellular *in vitro* techniques. The acellular experiments focused on determining the particle-derived formation of ROS upon dispersion in aqueous solutions, under biologically applicable conditions. The cellular experiments consisted of challenging human lung epithelial cells (A549 cell line) with varying amounts of earth and synthetic material in order to determine an inflammatory stress response (ISR). Defined as the cellular upregulation of ROS normalized by cellular viability, the ISR is a gauge of particle toxicity. The protocol is designed to not only capture the effect that low and high exposures have on cells, but also the effect of particle exposure on cells over time. This dissertation underlines the necessity of using an interdisciplinary approach to determine the impact of

geomaterials on human health and highlights the role that a material's structure, chemistry, oxidation state and complexity have in pathogenesis.

The results reported in this dissertation not only suggest that Fenton chemistry plays a role in inflammation-based diseases but also highlights the deleterious nature of ferrous minerals, pyrite in particular. The initial acellular oxidative dissolution studies demonstrated pyrite's ability to generate ROS and its relatively short biopersistence (a two micron pyrite particle will dissolve in about three years). Taken together it begins to explain the correlation between the prevalence of Coal Workers' Pneumoconiosis (CWP) among miners who are exposed to coal with high pyritic sulfur contents and why no pyrite is found in the autopsied lungs of these deceased miners. The extreme ISR of human lung epithelial cells exposed to pyrite (1,100 fold higher than the control) compared to standard reference materials (ISR generated by San Joaquin NIST soil with baseline trace element concentrations is 3 fold higher than the control and Montana NIST soil with highly elevated trace element concentrations is 11 fold higher than the control) confirms the inflammatory nature of pyrite and experiments with coals containing variable pyritic sulfur contents support the correlation with the prevalence of CWP in miners.

While an elevated ISR is generally attributable to both an upregulation of cellularly derived ROS and low cellular viability, the drivers for toxicity are complex. The design of the ISR experiments not only allowed for the base determination concerning a material's toxicity, it also allowed for different pathways of toxicity to be observed, highlighting the ability of a material to upregulate cellular ROS (indicator of future apoptosis) and/or generate necrotic cellular death. Subsequent experiments concerning the toxicity of mineral ores, Fenton metals, and natural dust samples underscore the importance of this integrated approach. Copper-sulfide ore minerals generate extreme ISR values (chalcopyrite rivaled pyrite at 860 fold higher than control), which resulted from both an upregulation of ROS and necrotic cell death. However, the ISR generated by the lead sulfide ore mineral galena (32 fold greater than the control) stems solely from necrotic cell death. Conversely, the ISR generated by manganese-doped goethite is predominately due to a cellular upregulation in ROS.

There are two factors that modulate a material's toxicity, the reactivity of the material and its components and total particle burden. Based on our research, a material that is considered inert will generate an ISR value that is around 2 to 4 fold greater than the control. This response is based solely on the presence of the foreign particles. This process is evidenced by our research

into the cause of lung illnesses among soldiers returning from Iraq. While the ISR experiments were able to narrow the dusts' minimal inflammatory nature to the carbonate phases and associated elements (e.g., manganese), the stress is only achieved after increasing the particle loading by more than a factor of 10 (over typical ISR exposure values). Given the extremely high PM2.5 concentrations in the Greater Middle East, the origin of the toxicity is likely predominately due to "particle overload," which causes impairment or cessation of the body's main defense mechanisms, phagocytosis and efferocytosis.

This dissertation is dedicated to my nieces:
Leah, Kiana, Rena, and Aria.

You can accomplish almost anything through persistence and believing in yourself.
Just keep in mind that an easy road is often a boring road.

The Road Not Taken

TWO roads diverged in a yellow wood,
And sorry I could not travel both
And be one traveler, long I stood
And looked down one as far as I could
To where it bent in the undergrowth;

Then took the other, as just as fair,
And having perhaps the better claim,
Because it was grassy and wanted wear;
Though as for that the passing there
Had worn them really about the same,

And both that morning equally lay
In leaves no step had trodden black.
Oh, I kept the first for another day!
Yet knowing how way leads on to way,
I doubted if I should ever come back.

I shall be telling this with a sigh
Somewhere ages and ages hence:
Two roads diverged in a wood, and I—
I took the one less traveled by,
And that has made all the difference.

- Robert Frost 1920

Table of Contents

List of Tables……..…… ix
List of Figures……..…… x
Publications……..…. xv
Acknowledgements……..xvi
1. Introduction……..1
1.1. Overview of Dissertation…….. 1
1.1.1. Medical Geology……1
1.1.2. Fenton Chemistry and Disease……...2
1.2. Organization of Dissertation……3
2. Pyrite-driven Reactive Oxygen Species Formation in Simulated Lung Fluid:
Implications for Coal Workers' Pneumoconiosis……... 5
2.1. Background……...5
2.2. Experimental Methods……..8
2.2.1. Batch Experiments……..… 8
2.2.2. Fluorescence Assay Procedure…….. 11
2.3. Results……...12
2.4. Discussion……13
2.5. Conclusions……...16
3. Quantification of particle-induced inflammatory stress response:
a novel approach for toxicity testing of earth materials…….. 27
3.1. Background……...27
3.2. Experimental……31
3.2.1. Culturing and Plaiting the A549 Human Lung Epithelial Cell Line……. 31
3.2.2. Inflammatory Stress Response Measurements…….. 31
3.2.3. Mineral Sample Preparation and Soil Standards……... 32
3.3. Results……...33
3.4. Discussion……35
3.5. Conclusions……...37
4. Inflammatory Stress Response in A549 Cells as a Result of Exposure to Coal:
Evidence for the Role of Pyrite in Coal Workers' Pneumoconiosis Pathogenesis…… 45
4.1. Introduction……...45
4.2. Materials and Methods……..48
4.2.1. Mineral Sample Preparation and Soil Standards……... 48
4.2.2. Culturing and Plating the A549 Human Lung Epithelial Cell Line……...48
4.2.3. Inflammatory Stress Response Measurements…….. 49
4.3. Results……...49
4.4. Discussion……50
4.5. Conclusions……...51
5. Metal-Sulfide Mineral Ores, Fenton Chemistry and Disease: Particle Induced
Inflammatory Stress Response in Lung Cells…… 57
5.1. Introduction……...57
5.1.1.Selected Metal-sulfides……...58
5.1.2. Particle Toxicity……58
5.2. Materials and Methods……..60

5.2.1. Mineral Sample Preparation……... 60
5.2.2. Acellular Hydroxyl radical and Hydrogen Peroxide Formation……61
5.2.3. Culturing and Plating the A549 Human Lung Epithelial Cell Line……...62
5.2.4. Inflammatory Stress Response Measurements…….. 63
5.3. Results……...63
5.3.1. Acellular ROS formation……... 63
5.3.2. Cellular Response…….. 64
5.3.2.1. Zinc Sulfides……... 65
5.3.2.2. Copper Sulfides……...65
5.3.2.3. Lead Sulfide……66
5.3.2.4. Iron Arsenic Sulfide……66
5.4. Discussion……66
5.5. Conclusions……...69
6. Manganese, Fenton Chemistry and Disease: Particle Induced Inflammatory Stress Response in Lung Cells……...76
6.1. Introduction……...76
6.2. Background……...77
6.3. Materials and Methods……..78
6.3.1. Mineral Synthesis and Sample Preparation …….. 78
6.3.2. Reactive Oxygen Species Formation……79
6.3.2.1. Adenine decomposition…….. 79
6.3.2.2. APF…….. 80
6.3.3. Culturing and Plating the A549 Human Lung Epithelial Cell Line……...80
6.3.4. Inflammatory Stress Response Measurements…….. 80
6.4. Results……...81
6.5. Discussion……82
6.6. Conclusions……...84
7. The role of Iraqi dust in inducing lung injury in United States soldiers: Initial findings of an *in vitro* study……..92
7.1. Introduction……...92
7.2. Materials and Methods……..94
7.2.1. Dust Sample Acquisition, Characterization and Treatment……...94
7.2.2. Particle-derived Reactive Oxygen Species Formation ……..... 94
7.2.3. Culturing and Plating the A549 Human Lung Epithelial Cell Line……95
7.2.4. Inflammatory Stress Response Measurements…….. 95
7.3. Results……...96
7.4. Discussion……97
7.5. Conclusions……...99
8. General Conclusions and Future Directions…… 108
References……113

List of Tables

Table 2.1. Composition of Simulated Lung Fluid*……..18

Table 2.2. Composition of Survanta® (beractant)*#.....19

Table 2.3. Speciation of ferrous iron in SLF and H_2O……20

Table 2.4. Lifespan of a pyrite particle based on dissolution rates for varying conditions*…...21

Table 2.5. Calculated mean lifetime of a 1μm diameter particle in water*…… 22

Table 3.1. Certified NIST elemental analysis of standard reference material…… 39

Table 4.1. Certified NIST elemental and surface area analysis of standard reference Material…… 52

Table 6.1. Metal salts and minerals investigated…… 85

List of Figures

Figure 2.1.Sulfate formation over time in batch experiments with pyrite. Batch oxidative dissolution experiments in which the sulfate formations between slurries of pyrite in water or SLF are compared. At two different points in time during the experiment with SLF, Survanta® was added as indicated by the dashed vertical lines. The temperature and pH were kept at 37°C and 7.4, respectively. Each symbol is the average concentration of triplicate analyses of sulfate; error bars for the average of the triplicate measurements are smaller than symbols used in graph. See text for more experimental details…….....23

Figure 2.2. Hydrogen peroxide formation/degradation over time in batch experiments with pyrite. Hydrogen peroxide concentration throughout the course of batch oxidative dissolution experiments of pyrite performed in water and SLF, respectively. Note that Survanta® was added in two separate doses in the experiment with SLF, see arrows……...… 24

Figure 2.3. Comparison of hydroxyl radical formation under a variety of conditions with water or simulated lung fluid. Fluorescence assay experiments evaluating the production of hydroxyl radicals in water and SLF without fatty acids or proteins under varying conditions. The formation of hydroxyl radicals in the experiment performed in water with a pyrite loading of 10 g/L is not represented since maximum detection limits were exceeded……..25

Figure 2.4. Persistence of pyrite as a function of size. The lifespan of pyrite particles of varying sizes in water versus SLF based on the dissolution rates determined in this study and the calculation scheme put forth by Lasaga 1984. To place the size of the particles in the context of exposures coal miners might experience, the relative mass frequency of particles found in the air of underground coal mines is shown in the left panel of the figure. The calculated results for pyrite particles with a size up to 10 μm are expanded in the inset on the lower right. Particles between 10 and 20 μm are abundant in air collected in active parts of underground coal mines……26

Figure 3.1. Schematic of 96-well microplate for cellular study. The arrangement for all microplates in this study is shown. The positioning of control wells, assay distribution and particle loadings are highlighted. For each material tested two identical plates were evaluated at the same time. Hence, for a given mineral and loading, the ROS level and cell viability was determined in 8 replicate wells…… 40

Figure 3.2. ROS upregulation, cell viability and ISR of A549 cells generated by glass beads. The cellular response to glass with increasing particle loading is presented with three different figures, all normalized to a control. (a) ROS upregulation, (b) cell viability, and (c) ISR – ROS upregulation divided by cell viability. For some data points, the error bars are hidden by the symbols…… 41

Figure 3.3. Microplate evolution over time. Microplate image displays the cellular response to acid treated pyrite over the course of the experiment. Two identical microplates are shown. The layout of the microplates follows the experimental designed presented in Figure 1. The changes in color on the right side of the microplate is due to development of the assay and becomes

darker as cell viability / cell numbers increase. The lack of color in the wells with the highest amount of pyrite indicates low cell viability……42

Figure 3.4. ISR of A549 cells generated by six materials with varying surface reactivities. The ISR generated by the six study materials are represented, with the cell viability for each in the inset. (a) Glass, (b) anatase, (c) San Joaquin Valley soil, (d) Montana soil, (e) untreated pyrite, and (f) acid treated pyrite. For some data points, the error bars are hidden by the symbols. * See Additional Data Files for clarification……..…… 43

Figure 3.5. Evolution of ISR over time. The ISR over time generated by all the materials at the highest particle loading (0.002 m^2/mL) are represented. For some data points, the error bars are hidden by the symbols……. 44

Figure 4.1. Schematic of 96-well microplate for cellular study. The arrangement for all microplates in this study is shown. The positioning of control wells, assay distribution and particle loadings are highlighted. For each material tested two identical plates were evaluated at the same time. Hence, for a given mineral and loading, the ROS level and cell viability was determined in 8 replicate wells…… 53

Figure 4.2. ROS upregulation, cell viability and ISR of A549 cells generated by unreactive coal samples. The cellular response to the three coal samples with increasing particle loading are presented, all normalized to a control. The samples, NIST 1635, 2682b and 2692b have the lowest pyritic sulfur contents……...54

Figure 4.3. ROS upregulation, cell viability and ISR of A549 cells generated by reactive coal samples. The cellular response to the two coal samples with increasing particle loading are presented, all normalized to a control. The samples, NIST 2684b and 2685b have the highest pyritic sulfur contents…….. 55

Figure 4.4. Evolution of ISR over time generated by NIST coal samples. The ISR generated over time by all the coal samples at the highest particle loading (0.002 m^2/mL) are represented. For some data points, the error bars are hidden by the symbols……..56

Figure 5.1. Kinetic analysis of reactive metal-sulfide ore minerals. Fluorescence measurements quantifying H_2O_2 + $^{\cdot}OH$ production in an acellular system (phosphate buffered solution at a pH of 7.4) taken as a function of time for galena, arsenopyrite and chalcopyrite are represented. Material loading was at 10 m^2/L……. 71

Figure 5.2. ISR of A549 cells generated by eight metal-sulfide ore minerals. The ISR generated by the eight study materials are represented, with cell viability for each in the inset. (a) Sphalerite – Yu Chen Mine (China), (b) sphalerite – Balmat, New York (USA), (c) sphalerite – Picos de Europa (Spain), (d) arsenopyrite, (e) galena, (f) chalcopyrite, (g) bornite, and (h) chalcopyrite. For some data points, the error bars (representing standard deviation of eight replicates) are obscured by the symbols…….. 72

Figure 5.3. Evolution of ISR over time generated by the highest ore mineral particle loadings. The ISR generated over time by all the metal-sulfide ore minerals tested at the highest particle loading (0.002 m^2/mL) is represented. For some data points, the error bars (representing standard deviation of eight replicates) are obscured by the symbols……...…73

Figure 5.4. Evolution of ISR over time generated by the moderate ore mineral particle loadings. The ISR generated over time by all the metal-sulfide ore minerals tested at the moderate particle loading (0.001 m^2/mL) is represented. For some data points, the error bars (representing standard deviation of eight replicates) are obscured by the symbols…… 74

Figure 5.5. Evolution of ISR over time generated by the low ore mineral particle loadings. The ISR generated over time by selected metal-sulfide ore minerals tested at a low particle loading (0.00025 m^2/mL) is represented. For some data points, the error bars (representing standard deviation of eight replicates) are obscured by the symbols……...75

Figure 6.1. XRD data of iron and manganese oxide minerals. XRD data of manganese, iron phases investigated in this study. Normalized intensity is offset for clarity along the y-axis. Phases G1 through G4 correspond to pure goethite with increasing manganese content in the structure (0%, 5%, 10% and 15% Mn for G1 through G4, respectively). The structural changes resulted from the increasing Mn content can be documented by the decreasing FWHM of the peaks located around 21.3 and 26.4˚ 2Q, as well as increased separation of the peak dublet between 36 and 37 degrees 2theta from 0.53 degrees in sample G1 (36.25 and 36.78˚ 2Q) to 1.04˚ in sample G4 (35.84 and 36.88˚ 2Q). Sample G5 is a mixture of hausmannite and a manganese oxalate artifact from the synthesis procedure. Oxalate peaks are marked with an asterisk……. 86

Figure 6.2. ISR of A549 cells generated by metal salt solutions. The ISR generated by the three metal salt solutions are represented, with cell viability for each in the inset. (a) Iron sulfate, (b) iron and manganese sulfate, and (c) manganese sulfate. For some data points, the error bars (representing standard deviation of eight replicates) are obscured by the symbols…… 87

Figure 6.3. ISR of A549 cells generated by synthetic iron and manganese oxide minerals. The ISR generated by the five synthetic iron and manganese oxide mineral species are represented, with cell viability for each in the inset. (a) G1 – goethite, (b) G2 – 5% manganese in goethite, (c) G3 – 10% manganese in goethite, (d) G4 – 15% manganese in goethite, and (e) G5 – hausmannite. For some data points, the error bars (representing standard deviation of eight replicates) are obscured by the symbols…….. 88

Figure 6.4. Evolution of ISR over time generated by metal salt solutions. The ISR generated over time by the metal salt solutions at two contaminant concentrations are represented. (a) 2 mM and (b) 1 mM concentrations of iron sulfate, iron and manganese sulfate, and manganese sulfate. For some data points, the error bars (representing standard deviation of eight replicates) are obscured by the symbols…… 89

Figure 6.5. Evolution of ISR over time generated by synthetic iron and manganese oxide minerals. The ISR generated over time by the five synthetic iron and manganese oxide mineral species at two contaminant concentrations. (a) 0.01 m^2/mL and (b) 0.002 m^2/mL concentrations of goethite, 5% manganese in goethite, 10% manganese in goethite, 15% manganese in goethite, and hausmannite. For some data points, the error bars (representing standard deviation of eight replicates) are obscured by the symbols……..… 90

Figure 6.6. Degradation of adenine by synthetic iron and manganese oxide minerals. The degradation of adenine (absorbance at 260 nm) by synthetic iron and manganese oxide minerals is used as a proxy for hydroxyl radical formation are represented. (a) adenine, (b) adenine and ethanol and (c) adenine and hydrogen peroxide…….. 91

Figure 7.1. SEM images of dust samples. Scanning electron microscope images of (a) Irradiated Camp Victory, Iraq, dust and (b) Fort Irwin, CA, dust……... 100

Figure 7.2. ˙OH generated by dust samples. ˙OH generated by Camp Victory, Iraq dust and Fort Irwin, CA dust. Concentrations are based on a 24 hour incubation in phosphate buffered solution at a pH of 7.4 with APF. Data represented as total ˙OH formed and also normalized by weight and surface area of the particles……... 101

Figure 7.3. ˙OH+H_2O_2 generated by dust samples. ˙OH+H_2O_2 generated by Camp Victory, Iraq dust and Fort Irwin, CA dust. Concentrations based on a 24 hour incubation in phosphate buffered solution at a pH of 7.4 with APF and HRP. Data represented as total ˙OH + H_2O_2 formed and also normalized by weight and surface area of the particles…… 102

Figure 7.4. ISR of A549 cells generated by Camp Victory, Iraq dust sample. The ISR generated by Camp Victory, Iraq dust over a range of particle loadings and times points. Inset displays the ISR generated by Camp Victory dust at low particle loadings. For some data points, the error bars are hidden by the symbols……. 103

Figure 7.5. ISR of A549 cells generated by the irradiated and acid treated dust samples. ISR generated by the four study materials are represented, with the cell viability for each in the inset. (a) Irradiate Camp Victory, Iraq dust, (b) Irradiated Fort Irwin, CA dust, (c) Acid Treated Camp Victory, Iraq dust, and (d) Acid Treated Fort Irwin, CA dust. For some data point, the error bars are hidden by the symbols……... 104

Figure 7.6. ISR of A549 cells generated by standard reference material. ISR generated by the three reference materials are represented, with the cell viability for each in the inset. (a) Glass beads, (b) NIST San Joaquin Valley soil (#2709), and (c) NIST Montana soil (#2710). For some data point, the error bars are hidden by the symbols……... 105

Figure 7.7. Evolution of ISR over time generated by elevated dust loadings. The temporal evolution of the ISR generated by elevated particle loadings (0.025 m^2/mL) for Camp Victory and Fort Irwin dust samples. Also represented are the dust samples there were treated with acid to remove carbonate phases. For some data points, the error bars are hidden by the symbols... 106

Figure 7.8. Evolution of ISR over time generated by elevated standard reference material loadings. The temporal evolution of the ISR generated by elevated particle loadings (0.025 m^2/mL) for reference material samples: glass beads, NIST San Joaquin Valley Soil (#2709) and NIST Montana Soil (#2710). For some data points, the error bars are hidden by the symbols...107

Figure 8.1. Particle Induced ROS formation. A schematic representing a particle's ability to directly and/or indirectly generate ROS in the body……... 112

Publications

Harrington AD, Smirnov A, Tsirka SE and Schoonen MAA (submitted) Manganese, Fenton Chemistry and Lung Disease – The Inflammatory Stress Response Generated by Manganese Substituted Goethite. *Occupational and Environmental Medicine*

Harrington AD, Tsirka SE and Schoonen MAA (submitted) Metal-Sulfide Mineral Ores, Fenton Chemistry and Disease – The Role of Particle Induced Reactive Oxygen Species in Generating an Inflammatory Stress Response in Lung Cells. *Geochimica et Cosmochimica Acta*

Harrington AD, Szema AM, Tsirka SE and Schoonen MAA (submitted) The role of Iraqi dust in inducing lung injury in U.S. soldiers – Initial findings *Journal of Occupational and Environmental Medicine*

Harrington AD, Tsirka SE and Schoonen MAA (accepted) Inflammatory Stress Response in A549 Cells as a Result of Exposure to Coal: Evidence for the Role of Pyrite in Coal Workers' Pneumoconiosis Pathogenesis. *Chemosphere*

Harrington AD, Tsirka SE and Schoonen MAA (2012) Quantification of particle-induced inflammatory stress response: a novel approach for toxicity testing of earth materials. *Geochemical Transactions*, **13**(4):1-10. DOI:10.1186/1467-4866-13-4

Harrington AD, Hylton S and Schoonen MAA (2012) Pyrite-driven Reactive Oxygen Species Formation in Simulated Lung Fluid: Implications for Coal Workers' Pneumoconiosis. *Environmental Geochemistry and Health*, **34**(4): 527-538. DOI:10.1007/s10653-011-9438-7

Szema AM, Schmidt MP, Lanzirotti A, **Harrington AD**, Lyubsky S, Reeder RJ, Schoonen MA (2012) Titanium and iron in lung of a soldier with nonspecific interstitial pneumonitis and bronchiolitis after returning from Iraq. *Journal of Occupational and Environmental Medicine*, **54**(1): 1-2. DOI:10.1097/JOM.0b013e31824327ca

Schoonen MAA, **Harrington AD**, Laffers R and Strongin DR (2010) Role of Hydrogen Peroxide and Hydroxyl Radical in Pyrite Oxidation by Molecular Oxygen. *Geochimica et Cosmochimica Acta*, **74 (**17): 4971-4987. DOI:10.1016/j.gca.2010.05.028

Acknowledgements

I would like to thank….

… my advisor, Dr. Martin A.A. Schoonen, for his support and guidance over the last 4+ years. Your confidence in my abilities made me a believer and your relaxed nature gave me room to grow and explore. I cannot convey my appreciation enough.

… my Pharmacology advisor, Dr. Stella E. Tsirka, for not only allowing me to use her lab, but for making me feel like a part of it. Your advice and care has not only helped me get through this process but kept my academic cynicism at bay.

… my family for their love and support. It has been a rough ride at times and knowing you are standing behind me has been helpful. A special thanks to my parents and sisters, with a very special thanks to my twin sister Jane (Harrington) Valenti who motivates and inspires me to be the best person I can be.

… my friends, new and old, for their constant reassurance and cheerleading. A special thanks to Victoria Kichuk, Jessical (Poole) Geden, Hoa Nguyen, Laura (Kubista) Harrington, Katie Smith, Francis McCubbin, Lisa Stallings, Millicent Schmidt, Caitlin Young, and Heidi Jensen.

… my husband, Dr. Alexander Smirnov, for his unending patience, support, and understanding. Falling in love my first week of graduate school was certainly not the plan, but without you, my last week of graduate school would not contain a doctoral hooding ceremony.

Chapter 1
Introduction

1.1.Overview of Dissertation

The purpose of this introductory chapter is to provide a brief overview of the field of study, the scope of the thesis, and present the organization of the thesis.

1.1.1. Medical Geology

The scientific field of medical geology, while new in its present form, is actually a re-emerging area of scientific interest. For more than 2,000 years, cultures around the World noted both the beneficial and deleterious nature of earth materials [1-9]. Historically, studies related to exposure to natural materials were correlative and took the form of epidemiology. While epidemiology remains an important research strategy, present-day medical geology is an interdisciplinary collaboration between geologists, biomedical researchers and health science professionals that aim to understand the role of earth materials in diseases. Current studies into the deleterious nature of natural materials can range from, but are not limited to: the biopersistence of a material, the role of structure and composition on reactivity, and the biological processes interrupted due to exposure.

Geoscientists have mostly focused on the role of mineral structure and composition on toxicity as well as the overall biodurability of the material. Most biodurability studies have been performed in water, but more recently experiments have been conducted in simulated body fluids. On the basis of biodurability studies, the lifetime of a particle deposited in the body can be estimated [10-12]. There has also been an increased interest in understanding the mechanisms that lead to reactive oxygen species (ROS) formation when minerals or, more broadly, earth materials are dispersed in water. Conversely, biologists, primarily concerned with the end result of disease formation, used cell lines and animals to determine cellular stress and tissue damage caused by exposure to particulate matter, including minerals [13, 14]. Both approaches are valid for disease prevention and treatment. However, due to the lack of communication between the two fields, until recently materials used by biologist were not well characterized or normalized properly and the fluids used by geoscientists lacked complexity. Consequently, progress in

determining a particle's toxicity has been hindered, resulting in a deficient understanding of particle-induced pathogenesis.

The emergence of new technologies has fostered data sharing and international collaborations; however, new technologies also drive the need for exposure research by further necessitating the mining of metals, the development of tools that distribute large amounts of dust into the air and the advance of nanomaterials [15]. For the most part, the relatively stricter safety regulations protect workers and the surrounding communities, but this is not always the case. Large scale contaminant exposures due to ignorance, negligence, or simply accidents occur numerous times a year worldwide, while exposures to nonpoint source pollution or even natural hazardous materials occur daily [16]. The research presented in this dissertation is highly interdisciplinary and focuses on exposure to geomaterials. By utilizing geochemical and pharmacological techniques, the role a material's structure, chemical composition, oxidation state, and complexity can have in generating stress in the body is better understood, thus allowing for insights into the underlying cause of pathogenesis.

1.1.2. Fenton Chemistry and Disease

The bulk of my research is focused on the role of Fenton metals, iron in particular, on pathogenesis [17, 18]. Even though the reaction was first described in 1894, the highly oxidative product in the reaction was not determined to be hydroxyl radicals until 1934 [19, 20]. The oxidative capabilities of a system containing ferrous iron and hydrogen peroxide continue to be an area of interest due to its health and remediation implications and a large body of research has been has been published on this topic since [12, 18, 21-23]. The sequence of reactions describing the interaction of ferrous iron with dissolved oxygen, including the Fenton reaction (Equation 3), are noted below:

$$Fe^{2+} + O_2 \rightarrow Fe^{3+} + O_2^{\cdot -} \qquad \text{Eqn. 1}$$

$$Fe^{2+} + O_2^{\cdot -} + 2H^+ \rightarrow Fe^{3+} + H_2O_2 \qquad \text{Eqn. 2}$$

$$H_2O_2 + Fe^{2+} \rightarrow Fe^{3+} + {}^{\cdot}OH + {}^{-}OH \qquad \text{Eqn. 3}$$

$$3H_2O_2 + 2Fe^{3+} \rightarrow 2Fe^{2+} + 2H_2O + 2O_2 + 2H^+ \qquad \text{Eqn. 4}$$

Reactions 1 through 3 represent the stepwise reduction of dissolved oxygen with iron as the electron donor. Equation 4 recycles ferric iron to ferrous iron. Collectively this set of reactions is often referred to as Fenton chemistry. Due to its abundance and high reactivity, the

focus of Fenton research has been on catalysis by ferrous iron. However, besides iron, metals like chromium, copper, vanadium and manganese have been shown to generate ROS, although the reaction mechanisms are not well understood [18, 24, 25]. Given the number of metals that are known to generate hydroxyl radicals, Equation 3 can be generalized to [23]:

$$H_2O_2 + M^{n+} \rightarrow M^{(n+1)+} + {}^{\cdot}OH + {}^{-}OH \qquad \text{Eqn. 5}$$

where M is a metal cation which can donate one electron and be stable at this new oxidation state [23]. By acting as a reducing agent, Equation 5 represents one of the ways metals can interact with oxygen species. When in the oxidized state, the metal has the potential to act as a one electron oxidizing agent (Equation 4). However, the shift in electrons and protons that occurs in Fenton chemistry can also occur in the absence of any metal species and as part of the body's immune system [24, 26, 27].

Inflammation in the body occurs when there is an imbalance between pro- and anti-oxidants [27]. It is, therefore, postulated that, after exposure to particulate matter, metal mediated ROS formation within the body may contribute to pathogenesis. However, some studies indicate that there is not a direct correlation between oxidative stress and particle-derived ROS formation [28]. Given this, when evaluating the hazardous nature of a material, it is important to not only determine its ability to directly generate ROS but also the biological response to it. Not only will this help determine the hazard level of a material, it will also help identify the origin of its toxicity.

1.2. Organization of Dissertation

This dissertation is comprised of six main chapters that are focused on the role of particle-derived ROS in pathogenesis. Each chapter represents a distinct project, which can be viewed as standalone papers. Chapters 2, 3 and 4 focus on the role of pyrite in the pathogenesis of coal workers' pneumoconiosis (CWP). Chapter 5 investigates the inflammatory nature of common ore minerals. Chapter 6 utilizes metal salts and manganese doped goethite in order to determine the inflammatory nature of manganese. Chapter 7 investigates the role that natural dust exposure has on the development of lung illnesses among United States soldiers returning from deployment in Iraq. Finally, chapter 8 offers an overview of the dissertation, highlighting the overall conclusions and future directions of the research.

Chapter 2 evaluates if ROS form as byproducts in the oxidative dissolution of pyrite in simulated lung fluid (SLF) under biologically applicable conditions and determines the persistence of pyrite in SLF. This study also addresses the importance of performing this type of experiment under biologically applicable conditions as opposed to in water. This paper has been published in Environmental Geochemistry and Health in 2011.

Chapter 3 introduces a new technique for assessing particle toxicity, the inflammatory stress response (ISR). Aside from the detailed outline of the experimental protocol, the utility of the technique was demonstrated by studying two soil reference materials provided by NIST, anatase powder, glass beads and pyrite. This suite of materials represents relatively inert materials (glass beads and anatase), moderately reactive materials (soils), and a highly reactive material (pyrite). This work is published in Geochemical Transactions, an Open Access journal, as a methods paper.

Chapter 4 elucidates the importance of the pyrite content of coal in causing CWP. The ISR generated by five natural coal samples containing variable pyritic sulfur contents is determined. This work is in review.

Chapter 5 focuses on the inflammatory nature of eight metal-sulfide ore minerals or accessory ore minerals and their ability to directly generate ROS. By utilizing the ISR toxicity marker, the importance of evaluating the chemistry, oxidation states and structure of a material when assessing risk management is highlighted.

Chapter 6 explores the role of a lesser known Fenton metal, manganese, in generating an ISR. Aside from using metal salts, goethite samples doped with varying concentration of manganese are synthesized. The importance of oxidation state in toxicity is highlighted, as well as the importance of using ISR as a measure of toxicity.

Chapter 7 reports on the inflammatory nature of a natural dust sample obtained near a burn pit in Camp Victory, Iraq. This material is compared to another dust sample of similar chemistry and mineralogy obtained from Fort Irwin, California. The role of particle overload in pathogenesis is discussed in the context of lung illnesses of United States soldiers after deployment in Iraq.

Chapter 2

Pyrite-driven reactive oxygen species formation in simulated lung fluid: Implications for Coal Workers' Pneumoconiosis

Andrea D. Harrington[1]*, Shavonne Hylton[1] and Martin A.A. Schoonen[1]

[1]Department of Geosciences, Stony Brook University, Stony Brook, NY 11794-2100.

Manuscript published in Environmental Geochemistry and Health

2.1. Background

Coal mining represents an occupational health burden that is likely to increase globally. Even with the emergence of alternative energy resources, coal continues to be a major energy supply worldwide and its demand and production are still on the rise. Currently 45% of the electricity in the United States is derived from coal-burning power plants[29]. The 2003 Basic Energy Sciences Advisory Committee forecasts that by the year 2050 the energy requirements for Earth's population will double. Most of this increased energy demand will likely be met with fossil fuels, and coal in particular. More specifically, according to the United States Energy Information Administration, world coal consumption will increase by 49% from 2006 to 2030 (127.5 quadrillion Btu to 190.2 quadrillion Btu) [30]. Much of the recent increase in production to meet the growing global energy demand has come by expansion of coal mining in Asia. Whereas in the United States coal mining has been transformed into a highly mechanized operation, coal mining in less developed countries, such as China, is a labor intensive operation.

The most prevalent work-related ailment among coal miners is Coal Workers Pneumoconiosis (CWP). Coal miners account for no more than 0.02% of the US population, but represent half of the pneumoconiosis deaths during the last decade of the 20th century [31], which points to the high prevalence of CWP among coal miners. Originally thought to be a variant of silicosis, CWP has recently been linked to pyrite. An epidemiological study has demonstrated a correlation between the Bioavailable Iron (BAI) content in coal and the prevalence of CWP in miners [15]. BAI is defined as the amount of iron released over a three

hour period in 10 mM phosphate solution at room temperature and a pH of 4.5 [15, 32]. The results of a recent experimental study suggest that the pyrite content of the coal, which can be as high as 5% by weight, is the underlying factor that causes the relationship between BAI and the prevalence of the disease [11]. Furthermore, a study conducted in Great Britain showed that tissue recovered from pneumoconiotic lungs of deceased coal miners has abnormally high amounts of iron-enriched material [33], consistent with the notion that exposure to iron minerals associated with coal plays a role in the pathogenesis of CWP. Pyrite and pyrite-bearing coal have recently been shown to spontaneously generate ROS when placed in water [34, 35]. On the basis of these results and additional research with pyrite-bearing coal, it has been suggested that the inhalation of iron-bearing dust may be responsible for a chronic elevated level of reactive oxygen species (ROS) production in lung tissue. This, in turn, may contribute to the pathogenesis of the disease [11]. However, these conclusions were based on experiments conducted in water. The goals of this study are to determine the oxidative dissolution rate of pyrite in simulated lung fluid (SLF) and to evaluate if pyrite particles can generate ROS in SLF.

Simulated lung fluid is a proxy for the extracellular fluid lining the surface of the alveolar epithelium [36-38]. This area of the lungs accumulates all of the respirable particulates and it is the primary environment for dissolution before phagocytosis can occur (for phagocytosis to occur a particle must be less than 15 to 20μm in size [39]) [10]. While phagocytosis is the primary method of clearance for respirable particles, "particle overload" can occur if the inhalation rate is greater than the alveolar clearance rate [40, 41]. Under conditions of particle overload, the clearance rate due to phagocytosis can be slowed or halted [42]. Hence, it is useful to experimentally determine the rate of dissolution of environmentally relevant particles, such as pyrite, in SLF. On the basis of experimentally determined dissolution rates it is possible to estimate the total time it takes to dissolve a particle of a given size upon inhalation.

A range of SLF formulations with different levels of complexity have been used in studies designed to evaluate the persistence/dissolution of particulate matter. Gamble's description of the composition of extracellular lung fluid is the basis for the formulation of SLF used here and in most other studies [43]. There are two different approaches to approximate natural extracellular lung fluid. One approach is to use a solution that is principally sodium chloride with both additional inorganic (bicarbonate, ammonium, phosphate) and organic components (glycine and citrate). The solution is kept at 37°C and buffered at pH 7.4 by

bubbling a 5% CO_2-air gas mixture through it. The drawback of this approach is that it does not capture the complexity of lung fluid as it lacks proteins, fatty acids, antioxidants, and other complex biomolecules. This shortcoming is overcome in the second approach by adding various complex biomolecules to the "simple" SLF.

A simple SLF is often used, however, to study the biopersistence of particulate matter *in vitro* [10, 43-51]. It has been shown that the absence of proteins and antioxidants has no marked effect on the dissolution rate of natural or man-made contaminants [46, 50], as long as the temperature and pH are kept at biologically relevant conditions. For example, the dissolution rate of talc at 37°C and a pH of 7.4 does not change when the fluid is varied from a very simple phosphate buffered solution to a more complex SLF [50]. In the present study, the rate of pyrite oxidative dissolution was determined in both a simple SLF (see Table 1) and one with added proteins and fatty acids. While a simple SLF formulation does not capture the full complexity of natural lung fluid, its simplicity makes it possible to evaluate the full extent to which particulates can generate ROS. The addition of more complex biomolecules provides additional pathways for superoxide, hydrogen peroxide, and hydroxyl radical to react, which decreases the steady state ROS concentrations. For example, as demonstrated in this study, the addition of a mixture of proteins and fatty acids (beractant, Survanta®); Table 2) lowers the hydrogen peroxide concentration in an experiment in which pyrite was dispersed in SLF lacking complex biomolecules.

The formation of ROS in pyrite slurries is a byproduct of oxidative dissolution of pyrite in air-saturated fluids. The equations below represent simplified reactions known to occur in natural waters. Although the systems complexity increases *in vivo*, the simplified reaction paths remain applicable. The oxidant can either be molecular oxygen (Equation 1) and/or dissolved ferric iron (Equation 2). Dissolved ferric iron can be formed in a pyrite slurry by the oxidation of ferrous iron (Equation 3).

$$2FeS_2 + 7O_2 + 2H_2O \rightarrow 2Fe^{2+} + 4SO_4^{2-} + 4H^+ \qquad \text{Eqn. 1}$$

$$FeS_2 + 14\,Fe^{3+} + 8H_2O \rightarrow 15Fe^{2+} + 2SO_4^{2-} + 16H^+ \qquad \text{Eqn. 2}$$

$$2Fe^{2+} + 1/2O_2 + 2H^+ \rightarrow 2Fe^{3+} + H_2O \qquad \text{Eqn. 3}$$

The oxidative dissolution of pyrite allows for iron to be released into solution as ferrous iron. When ferrous iron interacts with dissolved molecular oxygen, the Haber-Weiss reaction

mechanism sequence is initiated. This reaction sequence leads to the formation of hydrogen peroxide with superoxide acting as an intermediate (Equations 4 and 5).

$$Fe^{2+} + O_2 \rightarrow Fe^{3+} + {}^{\cdot}O_2^{-} \quad \text{Eqn. 4}$$

$$Fe^{2+} + {}^{\cdot}O_2^{-} + 2H^{+} \rightarrow Fe^{3+} + H_2O_2 \quad \text{Eqn. 5}$$

The existence of hydrogen peroxide allows for the formation of another ROS, hydroxyl radical, via the Fenton reaction (Equation 6). The fate of hydrogen peroxide depends, however, on the relative availability of ferrous and ferric iron. While a reaction with ferrous iron leads to the formation of hydroxyl radical, a reaction with ferric iron leads to decomposition of hydrogen peroxide into water and oxygen (Equation 7). In this respect, ferric iron acts similar to catalase [52].

$$H_2O_2 + Fe^{2+} \rightarrow Fe^{3+} + OH^{-} + {}^{\cdot}OH \quad \text{Eqn. 6}$$

$$3H_2O_2 + 2Fe^{3+} \rightarrow 2Fe^{2+} + 2H_2O + 2O_2 + 2H^{+} \quad \text{Eqn. 7}$$

It is expected that pyrite oxidative dissolution in SLF differs from pyrite oxidative dissolution in water, because dissolved phosphate has been shown to slow the rate of pyrite oxidative dissolution [53] and carboxylic acids have been shown to sorb onto its surface [54]. Sorption of carboxylic acids could affect the reaction mechanism and dissolved carboxylic acids may suppress the concentration of hydroxyl radical by complexing ferrous iron and preventing the Fenton reaction (Equation 6) or by scavenging the radical.

2.2. Experimental Methods

2.2.1. Batch Experiments

Batch oxidative dissolution experiments were performed on slurries of pyrite (Huanzala, Peru) in a 250 mL, glass, magnetically stirred vessel equipped with a water jacket (Ace Glass ™). The vessel was fitted with a cover containing four ports to allow for insertion of a pH probe, a dissolved oxygen probe, a titrant buret, a gas inlet and outlet, and a sampling tube. Both *in situ* and *ex situ* measurements were performed. The *in situ* measurements – temperature, dissolved oxygen and pH – were used in real time to keep the conditions in the mineral slurry saturated with air, at pH 7.4, and at 37˚C. The *ex situ* measurements – hydrogen peroxide, ferrous iron and sulfate – were used to determine the rate of pyrite oxidative dissolution and to determine the concentration of hydrogen peroxide throughout the course of the experiments.

X-ray fluorescence spectroscopy (Bruker S4 Pioneer) showed that the pyrite used in these experiments contained little to no impurities. Before use, the pyrite was crushed in an agate mill and sieved to less than 38 μm in order to obtain a suitable size fraction. The starting material was subsequently cleaned using a 0.1 M HCl solution to remove iron hydroxide and/or iron oxy-hydroxide patches from the surface and stored under vacuum in an anaerobic glovebag. The specific surface area of the pyrite, determined with a Quantachrome NOVA 5-point BET analyzer, was 1.923 m^2/g. The average diameter is estimated on the basis of the specific surface measurement to be 0.62 μm.

The temperature of the reaction vessel was controlled via a constant-temperature circulating water bath equipped with a thermostat-controlled heater. Kept at 37°C, the experiment was further monitored using a dissolved oxygen probe equipped with a thermistor (HACH™ LDO probe). This same probe's primary use was to continuously monitor the dissolved oxygen (DO) content in the slurry. The pH was monitored using a Titroline Alpha™ pH-stat equipped with a single junction, gel-filled electrode (Fisher™). The electrode was calibrated with standard NIST-traceable pH buffer solutions before the start of the experiment.

In order to evaluate the effect of SLF on the oxidative dissolution rate of the pyrite, separate replicate batch experiments were conducted with deionized (DI) water and SLF. In both experiments, molecular oxygen was the oxidant (some ferric iron is likely to have formed in the system, but at the pH of the experiments (7.4) very little dissolved ferric iron is expected to be present). The vessel was charged at the start of each experiment with 170 mL of the desired liquid (DI H_2O or SLF), which was allowed to warm to 37°C and reach a pH of 7.4 before the pyrite was added (~1 hour). The DO content was also allowed to stabilize at ~6.5 mg/L, which represents saturation at the temperature of the experiments. Although considered a high dose, a pyrite loading of 0.004 m^2/mL was used for each experiment (353 mg/170 mL) allowing for comparison with previous work. The reaction vessel was covered with aluminum foil throughout the experiment to block out the effect of light on pyrite oxidative dissolution, which has been shown to increase the oxidative dissolution rate [55]. Samples were taken over the course of the experiment for iron, sulfate and hydrogen peroxide analyses.

For the majority of the experiments performed in SLF, the pH was kept constant using the buffering capacity of the SLF in conjunction with CO_2. The CO_2 was delivered to the system via a tank containing 10% CO_2 in compressed air and fed into the system using a bubbler. The

flow rate of the CO_2 gas was adjusted so that the pH of the fluid was maintained within ± 0.1 of 7.4. Fresh SLF was prepared before each experiment using the procedure of Bauer et al. [10] which is a simple SLF [51]. Briefly, individual sodium dihydrogen phosphate monohydrate, sodium citrate dihydrate, sulfuric acid, ammonium chloride and calcium chloride solutions were made. The latter two intermediate solutions were filtered using 0.22 µm membrane slip-on filter before being added to the final container. The above solutions were mixed with a solution of sodium chloride, sodium bicarbonate, sodium carbonate and glycine in a calibrated glass flask. Given the short duration of the experiments, formaldehyde—a bactericide—was not added to the SLF as prescribed by Bauer et al (Table 1) [10]. The reagents used were of the highest quality, although we cannot exclude that they contain some trace amounts of metal. However, given their consistent use throughout the course of the experimental process and their trace levels compared to the amount of iron released by the pyrite, their presence is not expected to affect the conclusions. All SLF solutions were used within 24 hours of preparation. The SLF solutions were stored in the dark at 4˚C between preparation and use in the experiments. The effect of a more complex SLF solution on the pyrite oxidative dissolution rate was evaluated by adding two separate 6 µg/mL aliquots of Survanta® to a batch experiment with the simple SLF [56]. By determining the rate of sulfate formation before and after the additions of Survanta® we were able to calculate the pyrite oxidative dissolution rate in simple SLF and the rate with added proteins and fatty acids, while all other conditions in the experiment remained constant. The airflow into the reaction vessels was kept at 120 mL/minute. For experiments performed with DI water at 37°C, a 0.1 M NaOH solution was automatically titrated into the vessel to maintain the pH within a desirable range (7.4 ± 0.4). Tank gas was not used for these experiments; air was simply bubbled through the system via an air pump (Secondnature Challenger I). The air stream from the pump was first passed through a KOH solution to remove CO_2, which is necessary to keep the pH under control.

The concentration of hydrogen peroxide was determined in aliquots withdrawn from the vessel using the leuco crystal violet (LCV) method as previously reported [34], with some minor modification to compensate for the high buffering capacity of the SLF used in the experiments. In short, this modified method consists of pipetting 500 µL Na EDTA into a polystyrene cuvette (the EDTA is added to prevent the decomposition of hydrogen peroxide in the sample via the Fenton reaction by chelating free iron). Next, 100 µL of HRP and LCV reagent are added,

followed by a pH buffer, KH_2PO_4, to ensure the pH is at/near the optimal range of 4.2. Finally, 700 µL DI water was added. This mixture of reagents was prepared in the cuvettes before a 500 µL sample was withdrawn by syringe from the vessel for hydrogen peroxide analysis. The sample was filtered using a 0.22 µm membrane slip-on filter before adding it to the reagents in the cuvette. After incubation in the dark for ten minutes, the absorbance of the purple complex was measured using a HACH DR/4000 UV/vis spectrometer at a wavelength of 590 nm. Standards were made in order to determine the concentration of hydrogen peroxide in the samples. The concentration of dissolved ferrous iron remaining in the slurry at the end of the experiment was quantified by means of a HACH DR/4000 UV/vis spectrometer, using Hach™ Ferrozine method (Hach™ method 8147). The samples were analyzed for sulfate, a proxy for pyrite dissolution, using an automated ion chromatograph (Dionex™ DX 500) equipped with an AS4A-SC column.

2.2.2. Fluorescence Assay Procedures

The effect of SLF on the formation of hydroxyl radical was determined in a separate set of experiments apart from the batch experiments described above. The experiments followed a previously published protocol for the determination of hydroxyl radical in mineral slurries [57]. Natural pyrite from Huanzala, Peru, was purchased from Wards, crushed in an agate mill, sieved to less than 38 µm and stored under anoxic conditions until use. Using a five-point N_2 adsorption BET, the specific surface area of the pyrite was determined to be 1.25 m^2/g. The average particle size was one micron based on the specific surface area measurement. SLF was prepared as described above. The slurries (one in water and one in SLF) were spiked with the fluorogenic probe 3'-(p-aminophenyl) fluoroscein (APF) [58] at a concentration of 10 µM. For the experiments performed without pyrite, the same concentration of APF was injected as well as a 10 mM solution of ferrous ammonium sulfate heptahydrate or a 10 mM solution of ferric sulfate pentahydrate (one in water and one in SLF each). The slurries/samples were subsequently incubated for 24 hours at 25˚C. During the incubation periods the slurries were placed on a Barnstead/Thermolyne Labquake rotating mixer to keep the minerals in suspension.

After the incubation period, all samples were measured in 4-ml methylcrylate fluorescence cuvettes on a Turner Barnstead spectrofluorometer with excitation and emission wavelengths of 490 nm and 520 nm, respectively. Samples were calibrated against a standard

calibration curve with known amounts of hydrogen peroxide, APF, potassium phosphate buffer at pH 7.4, and HRP. APF was purchased from Invitrogen. All other chemicals were obtained from Fisher Scientific, except for Type II horseradish peroxidase, which was acquired from Sigma. All chemicals were of the highest available purity. The SLF, hydrogen peroxide, HRP and phosphate buffer solutions were prepared in Easy Pure 18.3 MΩ-cm, UV-irradiated, ultra-filtered water and stored in the dark at 4° C.

2.3. Results

A comparison between the oxidative dissolution rates of pyrite in water versus SLF was performed on the basis of net sulfate formation per unit time. The starting SLF solution contains some sulfate, hence the comparison of oxidative dissolution rate of pyrite in SLF and water is based on the rate of sulfate formation over time, or net sulfate formation per unit time. The net sulfate formation rate is calculated based on a linear regression of sulfate concentrations determined in triplicate of samples withdrawn from the vessel over the course of the experiment. The regression analysis shows that the oxidative dissolution of pyrite in SLF is twice as slow (51%) as compared to its oxidative dissolution rate in water (Figure 1). The addition of Survanta® has no effect on the rate of pyrite oxidative dissolution in SLF (Figure 1). This indicates that SLF with or without fatty acids and proteins exerts an important inhibitory effect on the oxidative dissolution of pyrite.

While the oxidative dissolution rate in SLF appears to be suppressed when compared to water, the hydrogen peroxide content in SLF is nearly twice as high initially (Figure 2). Preliminary experiments with SLF without Survanta® showed a steady state hydrogen peroxide concentration that was twice as high as the steady state concentration in an equivalent experiment with water. In the experiment with SLF presented in Figure 2, Survanta® was added before a steady state concentration in hydrogen peroxide was established. After the addition of Survanta®, the hydrogen peroxide concentration dropped rapidly, well below the level seen in the experiment with water.

Experiments using APF show that on average the hydroxyl radical concentration was 78% higher in experiments with water compared to experiments with simple SLF (Figure 3).

2.4. Discussion

The results show a significant decrease in pyrite oxidative dissolution rate combined with a higher initial concentration of hydrogen peroxide, but a lower concentration of hydroxyl radical in SLF compared to water. The slower pyrite oxidative dissolution in SLF is not unexpected, since the presence of phosphate inhibits pyrite oxidative dissolution, particularly at pH 4 and higher [53]. Given the phosphate concentration in SLF (1.2 mM), one would expect a significant suppression of the oxidative dissolution rate. Besides phosphate, organic components in SLF may also contribute to the diminished oxidative dissolution rate; for instance, glycine adsorbs to sulfur defects sites on the pyrite surface [59]. It is somewhat surprising that the additions of Survanta® – a natural surfactant – to simple SLF did not have an effect on the oxidative dissolution rate of pyrite, which is a surface-controlled process. However, this result is consistent with earlier work on the dissolution of talc in simple and more complex SLF [50]. The study with talc did not show a significant difference in dissolution rate between the two conditions. Hence, the results obtained in this study indicate that the complexity of the surfactant-free SLF is sufficient to determine biopersistence of pyrite in the lungs.

The steady state concentration of hydrogen peroxide appears to be strongly influenced by the solution composition. Hydrogen peroxide is formed in the first two-electron transfer step from the pyrite surface to molecular oxygen [52]. In addition, hydrogen peroxide is formed from superoxide when dissolved ferrous iron is oxidized by molecular oxygen. So the rate of formation of hydrogen peroxide in a pyrite slurry depends on the rate of pyrite oxidative dissolution as well as the direct one-electron reaction of molecular oxygen and dissolved ferrous iron. The steady state concentration of hydrogen peroxide is a balance between its formation and its decomposition. Hydrogen peroxide decomposition may either proceed via the Fenton reaction, which requires ferrous iron, or via a reaction with ferric iron producing water and oxygen [52]. Hence, the amount of iron in solution and its speciation is a key factor in determining the concentration of hydrogen peroxide in these experiments at any given time.

On the basis of the stoichiometry of pyrite (FeS_2), it is expected that the rate of iron release is half that of the rate of sulfate release. For example, upon completion of the experiment performed in SLF the total concentration of sulfate was 1165 μM, which means that the total concentration of ferrous iron released is expected to be 328 μM (this is half of the increase in sulfate over the course of the experiment, noting that 509 μM sulfate is present at the start of the

experiment because SLF contains some sulfate salt). However, the measured number was more than a factor of 10 less at 25.7 μM. This much lower dissolved iron content is a good indication that a significant amount of iron has been sequestered as Fe(III)-OH patches on the pyrite surface. The presence of these patches has been established in several studies using different techniques [60, 61]. Rather than passivating the pyrite surface, the Fe(III)-OH patches are known to be the major conduits for electron transfer between molecular oxygen and pyrite [62, 63] and are thought to play a role in the decomposition of hydrogen peroxide formed in the oxidative dissolution of pyrite (Schoonen et al, 2010). The development of the patches over time is likely responsible for the drop in hydrogen peroxide after the initial burst in the experiment with water and the section of the experiment with SLF in the absence of Survanta® (see Figure 2).

Several components in the SLF may be influencing the relative rates of the two hydrogen peroxide decomposition reactions through complexation of dissolved iron. Earlier work has shown that hydrogen peroxide can be stabilized in pyrite slurries by adding EDTA, a strong Fe(II) chelator [35]. Citrate, which is present in SLF used here, also forms strong complexes with ferrous iron. This notion is supported by a speciation calculation conducted with the program PHREEQCI [64]. In experiments performed in water, 98% of the ferrous iron is present as Fe^{2+}; while in experiments performed in simple SLF, 23% of the ferrous iron is present as Fe^{2+} and 64.5% is present as $FeCitrate^{-}$ (see Table 3). The high concentration of phosphate in SLF may inhibit the decomposition of hydrogen peroxide with ferric iron as reactant. This reaction is likely to take place on Fe(III)-OH patches on the pyrite surface that form as oxidative dissolution progresses. These patches are also the preferred sites for phosphate sorption. Hence, adsorption of SLF-derived phosphate is likely to slow down the decomposition of hydrogen peroxide to water and molecular oxygen. It is not clear, however, why the addition of Survanta® promotes the decomposition hydrogen peroxide (Figure 2). The addition of Survanta® triggers a rapid decrease of the hydrogen peroxide concentration, but it remains unclear whether this is due to a decrease of hydrogen peroxide formation or an increase in its decomposition.

Chelation of ferrous iron could also explain the lower concentration of hydroxyl radical in the experiments with simple SLF. By chelating ferrous iron, the hydrogen peroxide is partially stabilized and less hydroxyl radical is formed. Another factor that is difficult to evaluate is the possibility that some hydroxyl radical may have reacted with organic components present in SLF, generating other radicals for which APF is not sensitive. For example, glycine is known to

react with hydroxyl radical [65, 66]. This reaction then may have suppressed the hydroxyl radical concentration as reported by the APF probe. The only way to evaluate this is to conduct a series of Electron Spin Resonance experiments, which would determine the type and approximate concentrations of radical(s) present. However, this is outside the scope of the present study.

The results of this research allow one to constrain the lifetime of inhaled pyrite particles and evaluate their possible role in CWP pathogenesis. On the basis of the oxidative dissolution rate of pyrite in SLF (Table 4 and Figure 1), the length of time an individual pyrite grain could be expected to persist in the lungs is determined based on the dissolution kinetics model by Lasaga [67] (Figure 4). Predictably, fine-grained pyrite particles will dissolve in a shorter period of time. For example, a one micron particle is expected to be dissolved in about 1.5 years. By contrast, a particle with a diameter of 10 μm is projected to take more than a decade to dissolve. Approximately 80% of the airborne particles in an underground coal mine are larger than 10 μm, which is the cutoff for a particle to be considered respirable [68]. Pyrite in coal is typically present as micron or submicron particles embedded in the coal [69, 70]. So a lifespan on the basis of a one micron particle is more realistic. However, in gold and base-metal mines where pyrite is also common, the crystal size of pyrite in the rock is typically well above one micron. Hence, frequent exposure to coal dust, or other mined material, containing pyrite is expected to lead to a buildup of pyrite in the lung. The implication of the work reported here is that exposure to coal dust will lead to inhalation of pyrite particles that will slowly dissolve over the time scale of years. Research into the iron content of coal miner's pneumoconiotic lung tissue supports these timescales in that the tissue contained abnormally high amounts of iron but no pyrite [33]. Since autopsies usually occur years after retirement all of the pyrite should be dissolved, leaving only iron.

The persistence of respirable pyrite particles on timescales of years may promote a chronic level of inflammation with pyrite-derived hydrogen peroxide and ferrous iron producing the highly reactive hydroxyl radical. Other mineral components in coal, such as quartz, may contribute as well to the pathogenesis of CWP, but none of these particles produce hydrogen peroxide and hydroxyl radical in the quantities seen with pyrite [71]. Quartz and other minerals present in coal are, however, more persistent due to their very slow dissolution rate. This is illustrated with calculations of the lifespan of one micron particles of pyrite compared to that of one micron quartz particles (Table 5). Note that these calculations are based on dissolution rates

in pure water, not SLF, so data in Table 5 represent a minimum life span. The reactivity of other minerals linked to occupational lung ailments, chrysotile (white asbestos) and forsterite (olivine; used in glassmaking), are also presented in Table 5 for comparison. One micron asbestos particles are projected to be dissolved in less than a year, while one micron forsterite and quartz particles will not be dissolved in a human lifetime. There is clearly a need to conduct dissolution experiments in SLF so that more accurate estimates of the persistence of minerals important in occupational health can be obtained.

It is important to recognize that while this study addresses some of the complexity of inhalation exposure of pyrite associated with coal; it does not take into account the contribution of cellular responses to the exposure. For example, it is well known that epithelial cells will produce hydrogen peroxide in response to exposure to particulate matter. The hydrogen peroxide produced via this cellular mechanism will be in addition to any hydrogen peroxide produced by the minerals themselves. This also raises the specter of a synergy between pyrite and biopersistent minerals, such as quartz contained in coal. Both quartz and pyrite may trigger the cells to produce hydrogen peroxide, but pyrite promotes the formation of hydroxyl radical within the cells, which can contribute to the pathogenesis of CWP. We are currently studying the cellular response of epithelial cells to exposures of coal with different levels of pyrite.

2.5. Conclusions

The oxidative dissolution rate of pyrite in SLF with or without proteins and fatty acids has been determined for the first time. The addition of proteins and fatty acids to SLF does not affect the oxidative dissolution rate. The rate in SLF is about a factor of two slower than the rate of pyrite oxidative dissolution measured in air-saturated water. Not only does the SLF lead to a slower dissolution rate, it also changes the concentration of hydrogen peroxide and hydroxyl radical in solution. Chelation of iron is thought to be responsible for the stabilization of hydrogen peroxide, leading to higher initial concentrations than in experiments with water. Over time the concentration of hydrogen peroxide decreases; addition of beractant (Survanta®) to SLF leads to a rapid decrease of hydrogen peroxide in pyrite slurries. The initial stabilization of hydrogen peroxide also explains the lower hydroxyl radical concentrations observed in experiments with SLF. The pyrite oxidative dissolution rate data in SLF suggests that pyrite particles with a size of one micron are expected to persist for more than a year in the lung. Thus frequent inhalation

exposure to pyrite can lead to the buildup of a source of reactive ferrous iron that likely contributes to the pathogenesis of CWP.

Table 2.1. Composition of Simulated Lung Fluid*

Components	Concentration (mM)
Na^+	150.7
Ca^{2+}	0.197
NH_4^+	10.0
$H_2CNH_2CO_2H$ (glycine)	5.99
Cl^-	126.4
SO_4^{2-}	0.5
HCO_3^-	27.0
HPO_4^{2-} , $H_2PO_4^-$	1.2
$[HOC(CH_2CO_2)_2CO_2]^{3-}$ (citrate)	0.2

* Modified Gamble's solution from Bauer [10].

Table 2.2. Composition of Survanta® (beractant)*#

Components	Concentration (mg/mL)	Details
Phospholipids	25	Including 11.0-15.5 disaturated phosphatidylcholine
Triglycerides	0.5-1.75	n/a
Free fatty acids	1.4-3.5	n/a
Protein	< 1	Two hydrophobic, low molecular weight (SP-B and SP-C)

* Suspended in a 0.9% sodium chloride solution

(Drugs.com Updated: 2011 Sepember 19; Cited 2011 September 20] [72]

Table 2.3. Speciation of ferrous iron in SLF and H_2O*

Species	Percent	
	SLF	H_2O
$FeCitrate^-$	64.50	---
Fe^{+2}	23.18	98.16
$FeHPO_4$	10.76	---
$FeH_2PO_4^+$	1.18	---
$FeOH^+$	0.20	1.85
$FeSO_4$	0.19	4.1×10^{-5}
$Fe(OH)_2$	8.3×10^{-5}	1.1×10^{-3}
$Fe(HS)_2$	4.5×10^{-7}	8.8×10^{-6}
$Fe(OH)_3^-$	1.2×10^{-7}	1.1×10^{-6}
FeCitrateH	1.2×10^{-8}	9.6×10^{-12}
$Fe(HS)_3^-$	5.5×10^{-13}	---

* Speciation calculations performed by PHREEQCI [64].

Table 2.4. Lifespan of a pyrite particle based on dissolution rates for varying conditions*

Experiment	Dissolution Rate (mol / m^2 / sec)	Lifespan of a 1 µm Pyrite Particle (years)
Water	8.63×10^{-10}	0.77
"Simple" SLF	3.70×10^{-10}	1.79
SLF with 6 µg/mL Survanta®	4.69×10^{-10}	1.41
SLF with 12 µg/mL Survanta®	4.64×10^{-10}	1.43
Overall SLF[#]	4.38×10^{-10}	1.51

* Experiments kept at 37°C with a pH of 7.4 and the pyrite had a specific surface area of 1.923 m^2/g and sample loading of 0.004 m^2/mL.

[#] The overall dissolution rate of pyrite in "Simple" SLF and the SLF after being dosed with Survanta®. The r^2 value for this line is 0.9867.

Table 2.5. Calculated mean lifetime of a 1μm diameter particle in water*

Mineral	Lifetime (years)
Quartz[a]	17,024
Forsterite[b]	302
Enstatite[c]	5.06
Pyrite	0.77
Chrysotile[d]	0.58
Anorthite[e]	0.03

* Calculation scheme of Lasaga [67] was used

[a] Rimstidt and Barnes [73]

[b] Grandstaff [74]

[c] Schott et al. [75]

[d] Lifetime taken directly from Jurinski [50]. Experiment in a phosphate-buffered saline solution.

[e] Fleer [76]

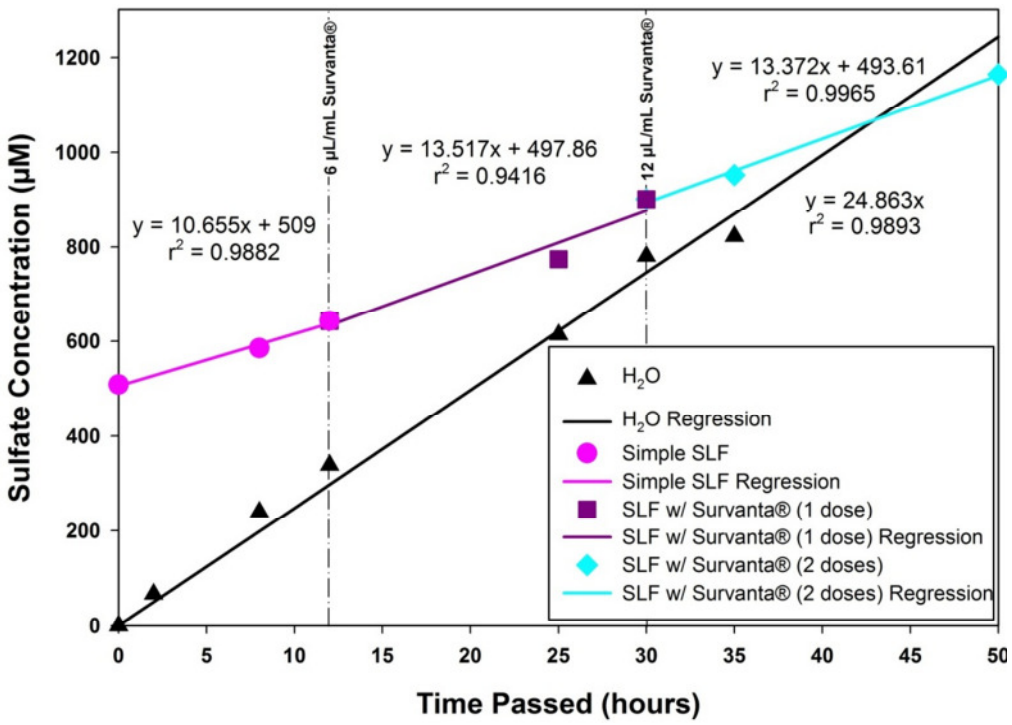

Figure 2.1.Sulfate formation over time in batch experiments with pyrite. Batch oxidative dissolution experiments in which the sulfate formations between slurries of pyrite in water or SLF are compared. At two different points in time during the experiment with SLF, Survanta® was added as indicated by the dashed vertical lines. The temperature and pH were kept at 37°C and 7.4, respectively. Each symbol is the average concentration of triplicate analyses of sulfate; error bars for the average of the triplicate measurements are smaller than symbols used in graph. See text for more experimental details.

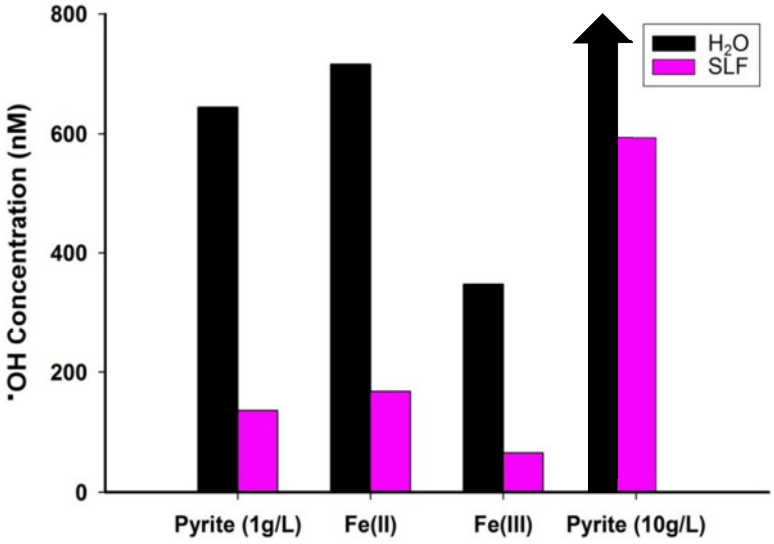

Figure 2.2. Hydrogen peroxide formation/degradation over time in batch experiments with pyrite. Hydrogen peroxide concentration throughout the course of batch oxidative dissolution experiments of pyrite performed in water and SLF, respectively. Note that Survanta® was added in two separate doses in the experiment with SLF, see arrows.

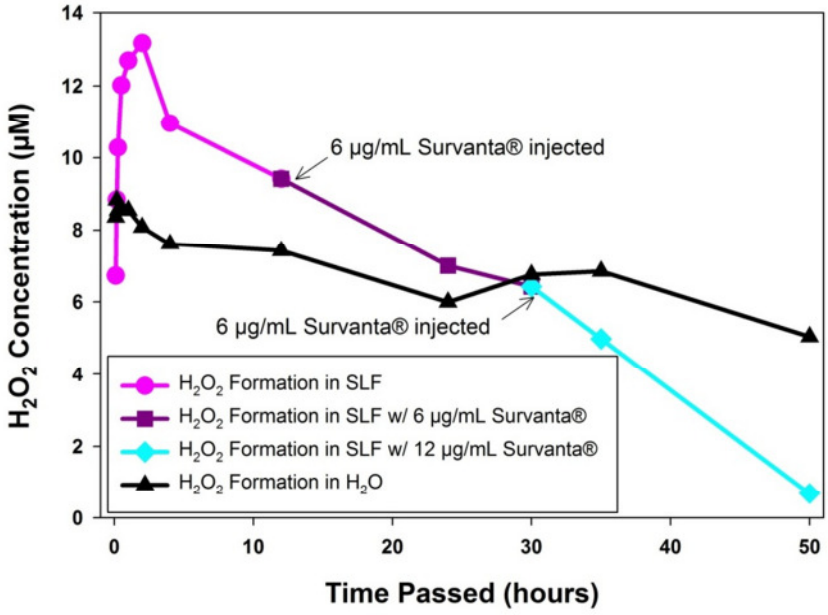

Figure 2.3. Comparison of hydroxyl radical formation under a variety of conditions with water or simulated lung fluid. Fluorescence assay experiments evaluating the production of hydroxyl radicals in water and SLF without fatty acids or proteins under varying conditions. The formation of hydroxyl radicals in the experiment performed in water with a pyrite loading of 10 g/L is not represented since maximum detection limits were exceeded.

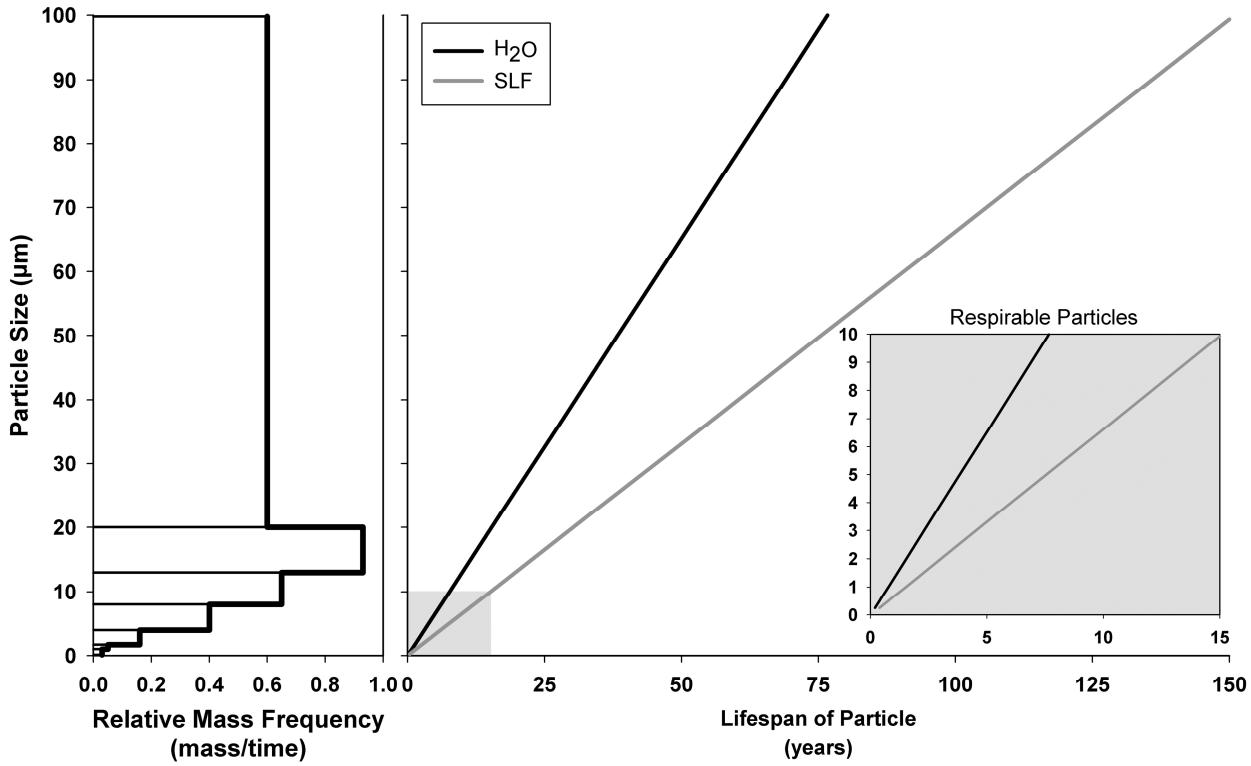

Figure 2.4. Persistence of pyrite as a function of size. The lifespan of pyrite particles of varying sizes in water versus SLF based on the dissolution rates determined in this study and the calculation scheme put forth by Lasaga 1984. To place the size of the particles in the context of exposures coal miners might experience, the relative mass frequency of particles found in the air of underground coal mines is shown in the left panel of the figure. The calculated results for pyrite particles with a size up to 10 µm are expanded in the inset on the lower right. Particles between 10 and 20 µm are abundant in air collected in active parts of underground coal mines.

Chapter 3

Quantification of particle-induced inflammatory stress response: A novel approach for toxicity testing of earth materials

Andrea D. Harrington[1], Stella E. Tsirka[2] and Martin A.A. Schoonen[1]*

[1] Department of Geosciences, Stony Brook University, Stony Brook, NY 11784-2100

[2] Pharmacological Sciences, Stony Brook University, Stony Brook, NY 11794-8651

Manuscript published in Geochemical Transactions

3.1. Background

The inhalation of mineral, coal, and volcanic dust can lead to a spectrum of lung diseases [4, 6, 9, 77-85]. Even in cases where the disease origin is clear (e.g., asbestosis, silicosis and coal workers' pneumoconiosis (CWP)), it is often unclear what role the earth material plays in the mechanism of pathogenesis (disease development). However, a common factor appears to be the upregulation of reactive oxygen species (ROS) in lung cells upon exposure [83, 86-91]. ROS are short-lived intermediate reduction products of molecular oxygen: superoxide ($O_2^{\cdot -}$), hydrogen peroxide (H_2O_2), and hydroxyl radical ($^{\cdot}OH$) [92, 93]. Although their formation is tightly regulated in the cells and tissues [27], the upregulation of ROS levels within lung cells as a result of an exposure to particulate matter can lead to a state of chronic inflammation. This inflammation is thought to pave the way for the development of lung disease [94, 95]. The emphasis of most studies has been in the context of occupational health or extremely high particle exposures, such as in areas affected by deposition of volcanic ash [96]. However, there are growing concerns that chronic exposures to soil and mineral aerosols at particle loading levels much lower than those encountered in mines and other occupational environments where workers are exposed to high loading of particles can lead to public health issues [97-100]. Aerosol-induced upregulation of ROS appears to be a contributing factor in the health burden caused by these exposures with non-occupational particle loadings [97, 99-101]. Given the possible critical role of particle-induced ROS upregulation upon inhalation, it is important to be

able to measure this effect for a wide range of earth materials. Therefore, the aim of this study is to develop a method for determining the upregulation of ROS in epithelial lung cell cultures as a result of exposure to earth materials. The method is focused on epithelial cells because the lung lining is often where diseases such as silicosis, asbestosis, and CWP develop [102, 103].

Earth materials can generate ROS spontaneously when dispersed in aqueous solutions free of cells and/or promote ROS upregulation in cells. It has been demonstrated that some minerals and other earth materials, such as coal, can spontaneously generate hydrogen peroxide and hydroxyl radical when dispersed in water [71, 87, 88, 92, 104-107] or simulated interstitial lung fluid [10, 36-38, 108]. Addition of earth materials to lung cell cultures can trigger an increase in ROS within the cells [109, 110]. Importantly, materials that do not show formation of ROS when dispersed in a cell-free aqueous system may elicit an upregulation of ROS in epithelial cells as part of a cellular response to the presence of a foreign substance.

Two separate mechanisms are involved in the generation of ROS in cell-free mineral slurries. Surface defects may react with water or dissolved molecular oxygen to form radicals. This mechanism is thought to be important in the formation of ROS in quartz slurries. The quartz surface has several types of defects resulting from the homolytic and heterolytic cleavage of the Si-O bond. When exposed to water or molecular oxygen, these surface defects form ROS, see work by Hurowitz and coworkers and Fubine for details [86, 92, 106].

A second mechanism is based on the incomplete reduction of dissolved molecular oxygen through electron transfer reactions with a transition metal (made available via oxidative dissolution of particulates), most often ferrous iron [92]. The reactions relevant in the formation of ROS with ferrous iron are summarized below (Equations 1-4). The ferrous iron can either be aqueous ferrous iron or ferrous iron exposed on mineral surfaces.

$$Fe^{2+} + O_2 \rightarrow Fe^{3+} + O_2^{\cdot -} \qquad \text{Eqn. 1}$$

$$Fe^{2+} + O_2^{\cdot -} + 2H^+ \rightarrow Fe^{3+} + H_2O_2 \qquad \text{Eqn. 2}$$

$$H_2O_2 + Fe^{2+} \rightarrow Fe^{3+} + {}^{\cdot}OH + {}^{-}OH \qquad \text{Eqn. 3}$$

$$3H_2O_2 + 2Fe^{3+} \rightarrow 2Fe^{2+} + 2H_2O + 2O_2 + 2H^+ \qquad \text{Eqn. 4}$$

Metals such as chromium, copper, vanadium, and manganese also generate ROS through the Fenton reaction (Equation 3) [18, 24, 25]. Although the reaction mechanisms for each of the Fenton metals has not been resolved at the same level of detail as with ferrous iron, the Fenton reaction (Equation 3) can be generalized to [23]:

$$H_2O_2 + M^{n+} \rightarrow M^{(n+1)+} + {}^{\cdot}OH + {}^{-}OH \qquad \text{Eqn. 5}$$

where M is a metal cation which can donate one electron and is stable at the higher oxidation state [23].

Epithelial lung cells exposed to particulate matter will upregulate ROS in an attempt to protect the cells against a foreign substance. Hydrogen peroxide release within epithelial lung cells is a non-specific defense mechanism designed primarily to kill pathogens [111], but the response is also triggered when cells encounter particulate matter [112]. Hence, the formation of ROS in cell-free aqueous systems is not a prerequisite for the upregulation of ROS when particles are added to lung cells, but particle-driven ROS formation may lead to enhanced ROS upregulation. The upregulation is expected to be particularly detrimental to cells if the material contains Fenton metals. Hydrogen peroxide produced in the cell will be converted to hydroxyl radical (Equation 5) [92], which will rapidly degrade a wide range of biomolecules leading to dysregulation of the cell and possibly cell death.

Cell death is one of the confounding factors in measuring the upregulation of ROS as a result of an exposure to particulate matter. Without correcting ROS measurements for cell viability, it is possible to incorrectly conclude that the exposure does not lead to ROS upregulation when, in fact, a significant fraction of the cells have died and those that survive have also been challenged and generate a higher ROS concentration. In the present study (see Experimental) we normalize the ROS readings with respect to the cell viability. We measure both ROS production in the cells and the cell viability using two separate assays. We utilize the A549 epithelial cell line, which is frequently used in toxicity studies [113-115]. It was first cultured in 1972 from the cancerous lung tissue of a 58 year old man. These adenocarcinoma human alveolar basal epithelial cells are easily cultured and proliferate quickly [116]. The relative "ease of use" and the fact that 90-95% of lung cancers are thought to originate in epithelial cells make this cell line an apt toxicity media for geoscientists [117, 118].

The two assays used in this cellular study are both routinely used in the biomedical community. The cellularly-derived ROS concentration is determined using 2',7'-dichlorofluoroscein-diacetate (DCFH-DA). This molecule is added to the cell culture and is taken up by living cells. Once in the cell it is converted to DCFH. DCFH reacts with hydrogen peroxide as well as hydroxyl radicals to become fluorescent DCF [119]. The fluorescence associated with the formation of DCF is a measure of ROS production in the living cells. Due to

the transient nature of ROS, it is important to use a probe that does not accumulate over time, but reflects both the rapid production and decay of ROS in the system. The cell viability is determined using 3-(4,5-dimethylthiazol-2-yl)-5-(3-carboxymethoxyphenyl)-2-(4-sulfophenyl)-2H-tetrazolium (MTS) [120], which produces a formazan product in the presence of phenazine methosulfate (PMS). The concentration of formazan product in the system is directly proportional to the number of living cells. This probe does not "predict" future apoptosis or necrosis but indicates the cell viability at the time of the assay measurement. Taken together, we define an indicator of overall "inflammatory stress response" (ISR) that is based on the ROS production normalized to cell viability (Equation 6).

$$ISR = \frac{Cellularly\ Derived\ ROS}{Cell\ Viability} * 100 \qquad \text{Eqn. 6}$$

Apart from using two routine biomedical assays in combination to define ISR, it is also important to use well characterized materials. In the development of this method, a range of natural and synthetic particulate matter was used as test materials. Anatase and silica glass, both synthetic, are often used as control materials to register the minimal cellular response to exposure to particulate matter because these materials are considered to have minimal reactivity. Two readily available reference soils from the National Institute of Science and Technology (NIST) with different metal concentrations (San Joaquin Valley NIST # 2709 and Montana NIST# 2710, see Table1) were used. The San Joaquin Valley soil sample was collected after removing the top 13 cm of soil in a plowed field in the Panoche fan between the Panoche and Cantu creek beds in the San Joaquin Valley. This soil represents a natural material of low reactivity. The Montana soil was collected from the top 10 cm of soil along the Silver Bow Creek in Butte, which is located near a major copper mine. When the creek floods, high concentrations of copper, manganese, and zinc are deposited at the collection site. Given its elevated trace metal content, including Fenton elements (manganese and copper), this soil sample represents a moderately reactive material. In order to determine an upper range of ISR, the mineral pyrite is examined. The treatment of pyrite with acid removes the oxidized iron from the surface, allowing for more rapid ROS formation due to Fenton chemistry. The toxicity of these materials is most easily compared if the measurements are normalized with respect to exposed surface area [121-123]. This requires that the specific surface area of the material is determined and experiments are conducted over a range of particle loadings. Furthermore, it is useful to conduct measurements as a time series to capture the development of ROS over a

period of 24 hours.

3.2. Experimental

3.2.1. Culturing and Plating the A549 Human Lung Epithelial Cell Line

The A549 human lung epithelial cell line was cultured using Ham's F12K Media containing 10% Fetal Bovine Serum (FBS) and 1% 1X Penicillin/Streptomycin (A549 cell growth media). Once confluence was reached in T75 flasks (cells covering entire bottom surface), the cells were passaged (removed from original flask and placed in another to grow in fresh media) at 1 x 10^5 cells/mL using trypsin with Ethylenediaminetetraacetic acid (EDTA) to detach the cells (remove from flask walls). For counting purposes, some of the cells were stained with Trypan blue and quantified using a hemocytometer. Wells in Columns 3-10 of the 96-well microplates were loaded with 8 x 10^4 cells/mL, covered with microplate lid, and allowed to incubate at 37˚C in the A549 cell growth media until confluent (approximately 2 days). Due to background generated by the assays, Columns 1-2 and 11-12 were kept cell free for normalization. All work with cells took place in a sterile hood to avoid airborne bacteria that would affect the results. When not in the hood, the microplate lid was kept on at all times. The incubator provided a controlled environment in terms of temperature, relative humidity and carbon dioxide (CO_2) concentration in air (37˚C, 95% and 5% CO_2 in air, respectively).

3.2.2. Inflammatory stress response measurements

After a two day incubation period, the cell growth medium was discarded by tipping the microplates into a container lined with sterile gauze, while the cells remained attached to the bottom of the plate. All liquid contents were allowed to drain out (approximately two minutes). Columns 1-6 were filled with 200 µL 50 µM DCFH-DA (from Sigma Aldrich) in Hank's Buffered Salt Solution (HBSS) and columns 7-12 were filled with 200 µL HBSS, and then placed in the incubator. During incubation, varying concentrations of the particle/contaminant slurry were created (normalized to surface area) via serial dilutions of a stock solution (i.e., 0.002 m^2 mineral/mL HBSS). After incubating for 20 minutes, all liquid contents of the microplate (DCFH-DA assay and HBSS) were again discarded (using the same approach as above). 200 µL of the contaminant slurry was added to the plates as shown in Figure 1. Rows A and H were kept free of contaminants due to edge effects, which simply put are widespread factors that cause the

degradation of assays during high-throughput screening experiments [124]. Row B was kept free of particles for normalization (control). After slurry addition, 20 µL MTS (from Promega) was added to all wells in columns 7-12. The plate was then placed in the incubator for 20 minutes before the first analysis. Therefore, each microplate had samples for the ROS and the viability assays, five particle loadings, and control wells (Figure 1). For each material tested, two microplates with identical loadings and layouts were evaluated simultaneously. Hence, the data for each particle loading for a given material was the average of eight separate wells, four per microplate.

DCFH-DA is a fluorometric probe used to determine cellularly derived ROS and was analyzed using Thermo Scientific's Fluoroskan Ascent. MTS is a colorometric probe used to determine cell viability and was analyzed using Molecular Devices' SpectraMax 340PC384. The microplates were kept in the incubator at all times other than for analyses. During periods before analysis, microplates were kept in dark using foil. Plates were analyzed at 20 minutes, 40 minutes, 1 hour, 2 hours, 3 hours and 24 hours (upper limit of MTS usability [125]).

To ensure the pH of the slurries remained within a biologically applicable range, measurements were taken in separate, replicate experimental microplates. A Sensorex Combination pH Electrode (½ inch in diameter) attached to a Fisher Scientific Accumet Portable pH meter was inserted into various wells throughout the duration of experiment. Each well was measured once. The pH measurements are estimated to have an uncertainty of 0.1 pH units. Keeping the pH within a biologically applicable range ensures cellular stress and death is derived solely by the foreign species.

3.2.3. Mineral sample preparation and soil standards

All specific surface areas were obtained using a Quantachrome NOVA 5-point BET analyzer using UHP N_2 gas. The silica glass beads obtained from Corpuscular had a specific surface area of 0.326 m^2/g. The mineral anatase (TiO_2) was procured in powder form from the Aldrich Chemical Company with a specific surface area of 9.471 m^2/g. Soil standards #2709 (San Joaquin Valley) and #2710 (Montana), acquired from NIST, had a surface area of 12.284 m^2/g and 9.976 m^2/g, respectively. The only material treated after procurement was the Huanzala pyrite, which was ground and sieved to a size below 38 µm. A portion of the ground pyrite was acid treated using a 0.1 M HCl solution to remove iron (oxy)hydroxide weathering products from

the surface and stored under vacuum in an anaerobic glovebag. The specific surface areas of the untreated and acid washed pyrite were 1.887 m^2/g and 1.923 m^2/g, respectively. The estimated error in the BET measurements is 2.5%. This estimate is based on repeated analyses of a TiO_2 surface area standard provided by Quantachrome.

3.3. Results

Particle-derived ISR was determined for six materials with varying surface reactivities. Figure 2 illustrates the ROS production, the cell viability, and the calculated ISR for the exposure to glass beads. The error bars are calculated ± standard deviations based on the eight replicate measurements for ROS and cell viability (i.e., 4 identical conditions per microplate, two microplates in total), with the errors for the ISR calculated using a standard propagation method. Note that in the case of the glass beads the cell viability increased somewhat with loading, which led to a leveling off of the ISR curve as function of loading. Overall, it is clear that adding more glass beads resulted in an increase in ISR.

Figure 3 shows images of two microplates in which the A549 cells were challenged with acid-washed pyrite. The two plates had identical loadings and layout. The color changes developed over time on the right side of the microplate indicate changes in cell viability, which was determined using the MTS protocol. The intensity of the purple color increased over time as cell viability increased. The lack of the purple color indicates cell death.

The ISR and cell viability for all materials tested in this study are shown in Figure 4. In each panel in Figure 4, the cell viability data are shown as an inset. The ISR over time for all the materials tested is represented in Figure 5. In separate replicate experiments, we determined that the addition of the earth materials itself did not lead to a significant drop in pH within the cell cultures. The cell cultures challenged with the highest loadings of pyrite, expected to be the most reactive material in terms of changing slurry pH, did not deviate from the pH in the control by more than 0.3 pH units.

Anatase and glass beads are relatively inert particulates and these materials are often used in toxicity studies to represent base level responses [126, 127]. These two materials, as well as the San Joaquin Valley soil, showed no drastic decrease in cell viability. The ISR generally increased with particle loading at any given time point for these three materials. Their presence generated up to 450% (anatase) and 350% (glass beads) the ISR compared to measurement of

ISR in cells without any particles added (control). The San Joaquin Valley soil generated a lower ISR (250% at highest loading compared to control). While all three materials are relatively inert, the ISR over time was different for each material. The San Joaquin Valley soil generated the highest ISR within the first 20 minutes, the glass after 40 minutes and the anatase after 3 hours (Figure 5). The ISR in the glass beads and anatase experiments showed a progression toward the maximum levels of quantified stress and then a decrease over time. The data for the San Joaquin Valley soil showed a more erratic pattern with the ISR measured after 20 minutes and 3 hours nearly the same, while the measurements after 40 minutes and 1, 2 hours were lower. As shown in Figure 4c, the error bars for several of the data sets overlap. Hence, it is not possible to extract definitive trends for ISR as a function of time that are representative of the whole "inert" group of materials tested here.

The Montana soil, which is a soil impacted by mining activity that contains high levels of transition metals, caused a significant drop in cell viability over a period of 24 hours (60% viability) along with a significant ROS signal. As a result, the ISR caused by the Montana soil was by a factor of 11 above the control after 24 hours at the highest loading. The Montana soil showed a spike in ISR after 20 minutes, just as the San Joaquin Valley soil, followed by a drop in ISR. A systematic increase in ISR was then measured from 40 minutes to 24 hours after the start of the experiment. This suggests that there was both an acute response that led to elevated ISR, followed by a delayed response that led to elevated ISR. The initial cell response to the insult event generated a burst of ROS, possibly to try and rid the area of foreign substances. A slower process then took over, potentially indicative of cellular adaptation to the stress inducer, and generated a relatively low ISR over the next 21 hours.

The ISR generated by both the treated and untreated pyrite was at least a factor of 40 higher than the peak ISR of the Montana soil and a factor of 100 higher than the peak for anatase. The untreated, or oxidized, pyrite generated an ISR value that was 450-fold higher than the cells without particles after 24 hours. The cell viability was also immediately affected by the presence of this pyrite. At the highest pyrite loading the cell viability is reduced to 1%. At the highest loading, the acid washed pyrite generated an ISR value that was 1,100-fold the control after 2 hours. It is important to note the variation in ISR over time of the two pyrite samples. After 2 hours, the ISR generated by oxidized pyrite was 20% of the level seen at 24 hours. Hence, the ISR in the experiment with oxidized pyrite increased over time. By contrast, the ISR

measured in the experiment with acid washed pyrite decreased by a factor of four between the 2 hour and 24 hour time points for the highest particle loading.

The data for the untreated pyrite after 24 hours contained an anomalously high reading for the 0.001 m^2/mL loading. Labeled as an outlier on Figure 4e, this data point, which is the average of eight separate wells with identical conditions over two microplates, yielded extremely low cell viability readings. When the cell viability values of two the surrounding particle loadings (0.0005 m^2/mL and 0.002 m^2/mL) were used to estimate the cell viability for the 0.001 m^2/mL loading using a weighted average approach, the calculated ISR value was adjusted downward and falls on a curve that shows the expected general increase in ISR with particle loading (See Additional Files for more details). This particular data point underlines the importance of including three separate factors in the experiments. One factor is abundant replication, which is here made possible by using duplicate 96-well plates, leading to eight separate measurements for each condition. The second factor is that the 96-well plates make it possible to experiment with multiple loadings. The last factor is that multiple measurements are made over time allowing for trends to emerge that show an increase in ISR with increased particle loading. Any major deviation from a general increase of ISR with increased particle loading requires a closer examination of both the ROS upregulation and cell viability data.

3.4. Discussion

Utilizing both cell viability and cellular ROS generation assays, a protocol is created for determining ISR induced by earth materials. By measuring the ROS production and cell viability within minutes to hours for a period up to 24 hours, the method provides insight into the development of ISR over time. The dose-response is evaluated by varying the particle loading. For highly reactive particles, it is important to adjust the particle loading so that cell viability remains measurable, as cell viability is the denominator in the ISR term.

All materials tested here show a general increase in ISR with increasing particle loading or dose; however, the development of ISR over time is different for each material. As illustrated by the results for the Montana soil (Figure 4d), an initial burst of ROS formation immediately upon addition of the particles may be followed by a separate, slower process that leads to upregulation of ROS. The standard for toxicity studies is for plates to be analyzed at one time point (commonly 3 hours or 24 hours) after particulate exposure [128-130]. If this approach was

used and the plates were only read at 3 hours, then the ISR for both the oxidized pyrite and acid washed pyrite would be underestimated by 500%. If the plates were only read at 24 hours, then the ISR for the acid washed pyrite would be underestimated by 330%. Due to limitation of the stability of the assays the experiments were terminated at 24 hours [125]. However, in the case of the materials that generate an increasing ISR with time, the ISR is expected to continue to increase. In fact, an ISR is expected to persist until complete particle dissolution. Therefore, the ISR measurements represented here serve as an indication of possible long-term toxicity.

For this new protocol, experiments were conducted on six materials that offer a wide spectrum of responses. The glass beads and anatase showed little effect on cell viability but caused some upregulation of ROS. Although often used to represent baseline stress levels, anatase does generate a measureable amount of ROS [131, 132]. This upregulation likely represents the minimum cellular response to the presence of an otherwise unreactive foreign material. This low ISR was also observed with the San Joaquin Valley soil, which is characterized by NIST as a soil with baseline trace element concentrations. By comparison, the Montana soil is enriched in metals, including possible Fenton metals other than iron (e.g., Cu, Mn, see Table 1) as well as toxic metals that may affect cell viability (e.g., Pb, Zn, As, Cd, see Table 1). The high metal content in the Montana soil is likely the cause for the higher ISR value, which is due to a combination of cell death and ROS upregulation in the remaining cells. .

Pyrite elicited by far the strongest ISR. In earlier work we showed that pyrite is capable of producing ROS when dispersed in water or simulated lung fluid [108]. We speculate that when epithelial cells are exposed to pyrite they form hydrogen peroxide as part of the normal immune defense response. However, the presence of ferrous iron promotes the Fenton reaction, which leads to the formation of hydroxyl radical. The production of hydroxyl radical within the cells is likely the cause for the high degree of cell death in the experiments with pyrite. The surviving cells are compromised and as a result of the normalization with respect to cell viability the ISR rises to very high levels. The difference in the development of the response to acid-washed pyrite and oxidized pyrite is likely due to the presence/absence of ferric oxide patches on the surface. As shown in earlier work [133], the presence of ferric oxide patches on the surface of pyrite leads to the decomposition of hydrogen peroxide to water and molecular oxygen (Equation 4), rather than hydroxyl radical. However, over time dissolved ferrous iron does build up and the Fenton reaction goes forward (Equation 3). Acid washing of pyrite removes any ferric

oxide patches [134, 135]; hence, acid-washed pyrite is expected to very effectively promote the formation of hydroxyl radical in a cell that is producing hydrogen peroxide until the surface become partially covered with ferric oxide patches.

From an occupational health perspective, mine workers who create fresh rock dust containing pyrite are likely to inhale pyrite that would stimulate a burst of hydroxyl radical formation. On the other hand, settlements downwind from pyrite-containing mine tailings might be inhaling dust with oxidized pyrite. Both exposures lead to inflammation, but the exposure to fresh pyrite surfaces will lead to higher levels of inflammation. Furthermore, the data for untreated pyrite data suggest that the ISR would continue to increase with time. Given the form pyrite takes in coal, complete dissolution of a single framboidal pyrite particle would occur within a year [67, 108]. It is unknown whether a short-lived spike in ISR is more important to pathogenesis than a lower more prolonged ISR. However, it must be taken into consideration that these experiments represent a single exposure event. In the case of a coal miner, each inhalation could be exposing the miner to reactive materials. The average adult takes between 12-20 breaths per minutes, so average the coal miner would have approximately 2,000,000 exposures in a year (assuming a 40 hour work week). .

Overall the protocol presented here can be used to characterize a wide range of earth materials in terms of their ability to induce an ISR in cells. Complemented by acellular assays to determine particle-driven ROS formation, chemical analysis, and a well-established provenance of the sample, the protocol presented here can provide a rapid assessment of the ability of the earth material to provoke upregulation of ROS, lead to cell death, and induce inflammation in the remaining cells. The materials tested here are only a small subset of the materials that are of interest from a public health or occupational health perspective.

3.5. Conclusions

The method described here is designed to test the ability of earth materials to cause cell death and upregulate ROS in cells. Both dose-response and temporal changes in ISR can be resolved by the protocol. The method provides the geosciences community an opportunity to contribute to the emerging field of medical geology by combining two well-established assays. Using the method described here along with knowledge of the provenance, composition and

treatment of earth materials is expected to lead to new insights into the effect of earth materials on public and occupational health.

Table 3.1. Certified NIST elemental analysis of standard reference material [136, 137]

Element	San Joaquin Valley Soil	Montana Soil
	Mass Fraction (%)	
Aluminum	7.50 ± 0.06	6.44 ± 0.08
Calcium	1.89 ± 0.05	1.25 ± 0.03
Iron	3.50 ± 0.11	3.38 ± 0.10
Magnesium	1.51 ± 0.05	0.853 ± 0.042
Phosphorus	0.062 ± 0.005	0.106 ± 0.015
Potassium	2.03 ± 0.06	2.11 ± 0.11
Silicon	29.66 ± 0.23	28.97 ± 0.18
Sodium	1.16 ± 0.03	1.14 ± 0.06
Sulfur	0.089 ± 0.002	0.240 ± 0.006
Titanium	0.342 ± 0.024	0.283 ± 0.010
	Mass Fraction (µg/g)	
Arsenic	17.7 ± 0.8	626 ± 38
Cadmium	0.38 ± 0.01	21.8 ± 0.2
Copper	34.6 ± 0.7	2950 ± 130
Lead	18.9 ± 0.5	5532 ± 80
Manganese	538 ± 17	22,124 ± 876
Mercury	1.40 ± 0.08	32.6 ± 1.8
Zinc	106 ± 3	6952 ± 91

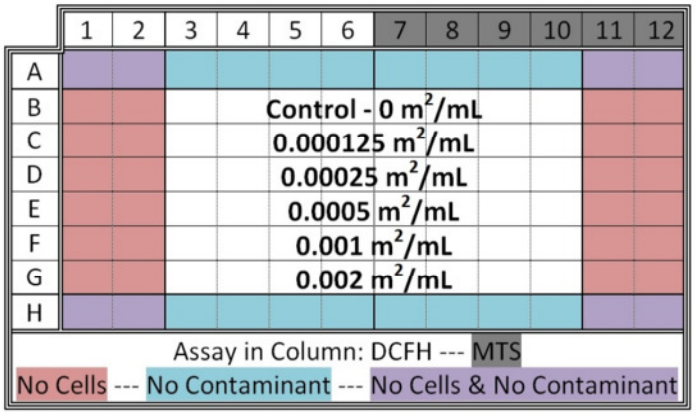

Figure 3.1. Schematic of 96-well microplate for cellular study. The arrangement for all microplates in this study is shown. The positioning of control wells, assay distribution and particle loadings are highlighted. For each material tested two identical plates were evaluated at the same time. Hence, for a given mineral and loading, the ROS level and cell viability was determined in 8 replicate wells.

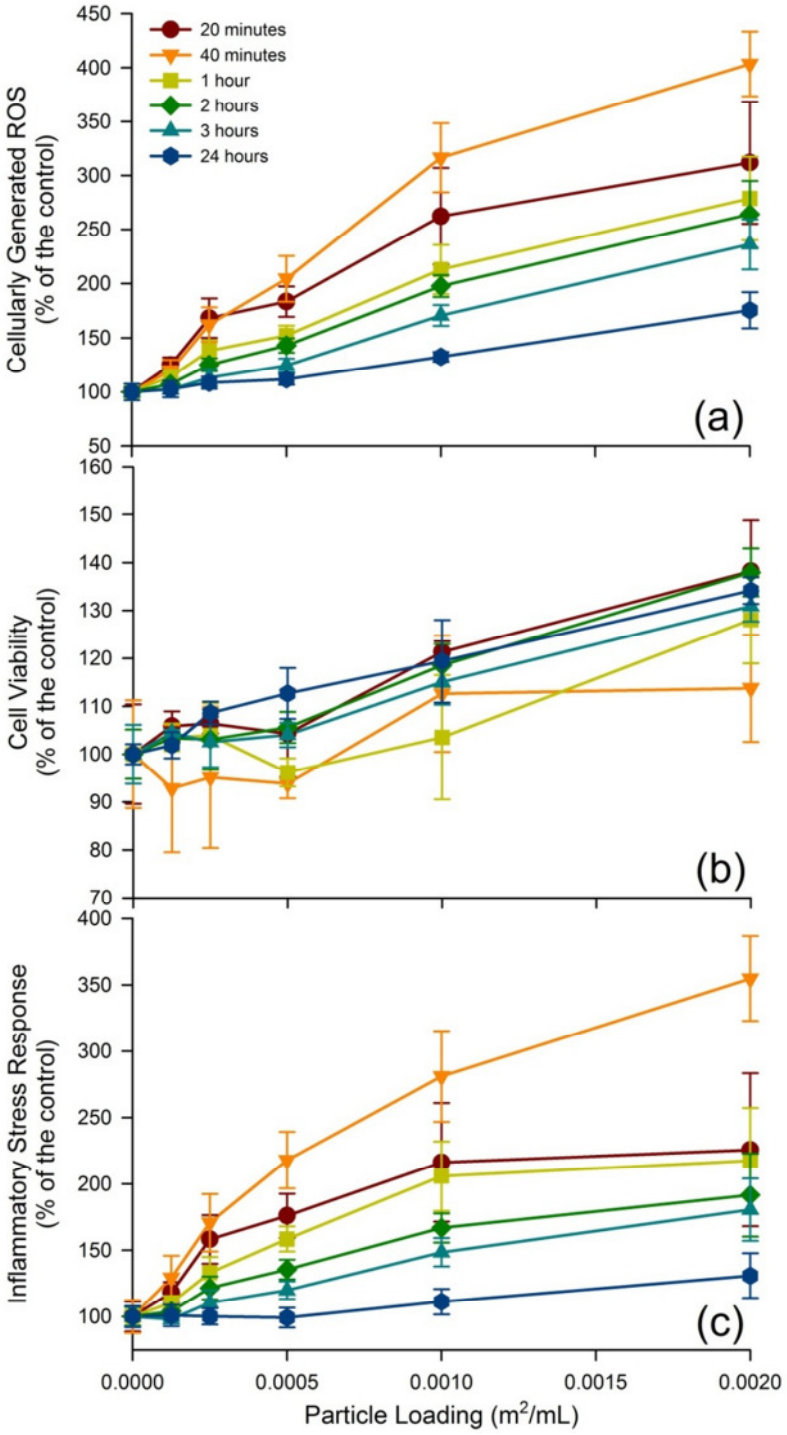

Figure 3.2. ROS upregulation, cell viability and ISR of A549 cells generated by glass beads. The cellular response to glass with increasing particle loading is presented with three different figures, all normalized to a control. (a) ROS upregulation, (b) cell viability, and (c) ISR – ROS upregulation divided by cell viability. For some data points, the error bars are hidden by the symbols.

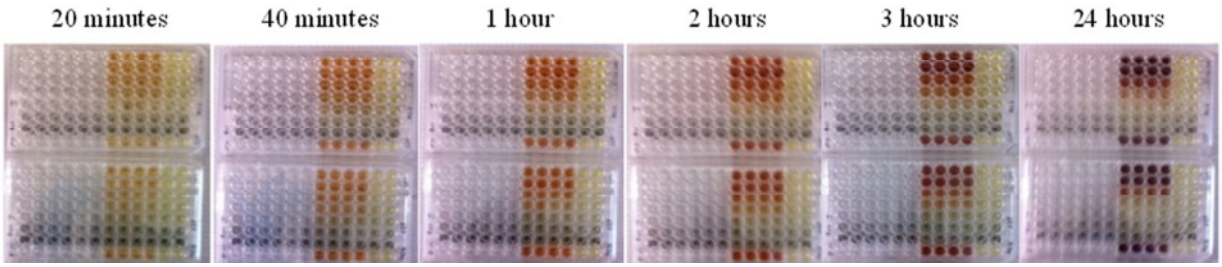

Figure 3.3. Microplate evolution over time. Microplate image displays the cellular response to acid treated pyrite over the course of the experiment. Two identical microplates are shown. The layout of the microplates follows the experimental designed presented in Figure 1. The changes in color on the right side of the microplate is due to development of the assay and becomes darker as cell viability / cell numbers increase. The lack of color in the wells with the highest amount of pyrite indicates low cell viability.

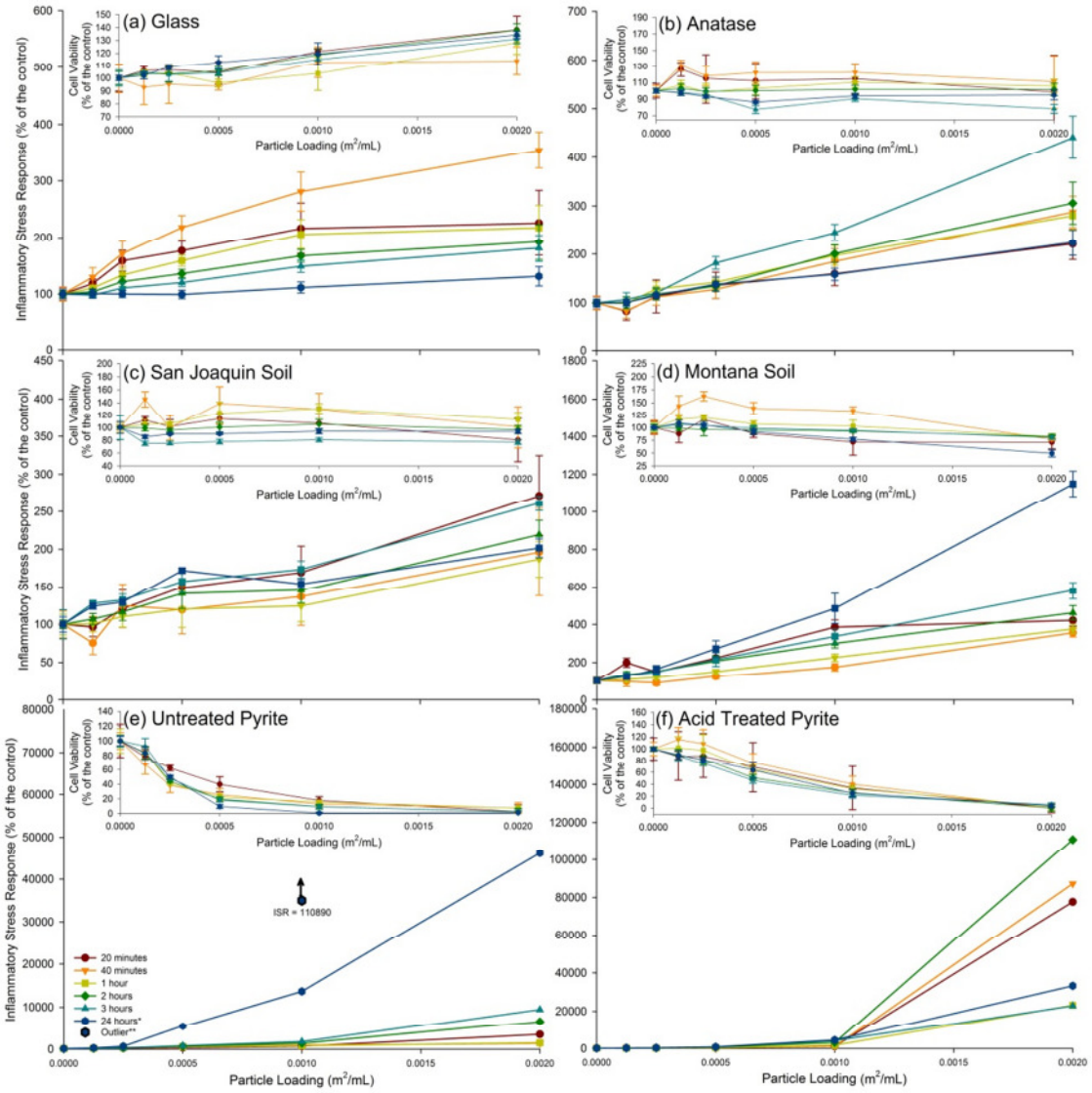

Figure 3.4. ISR of A549 cells generated by six materials with varying surface reactivities. The ISR generated by the six study materials are represented, with the cell viability for each in the inset. (a) Glass, (b) anatase, (c) San Joaquin Valley soil, (d) Montana soil, (e) untreated pyrite, and (f) acid treated pyrite. For some data points, the error bars are hidden by the symbols. * See Additional Data Files for clarification

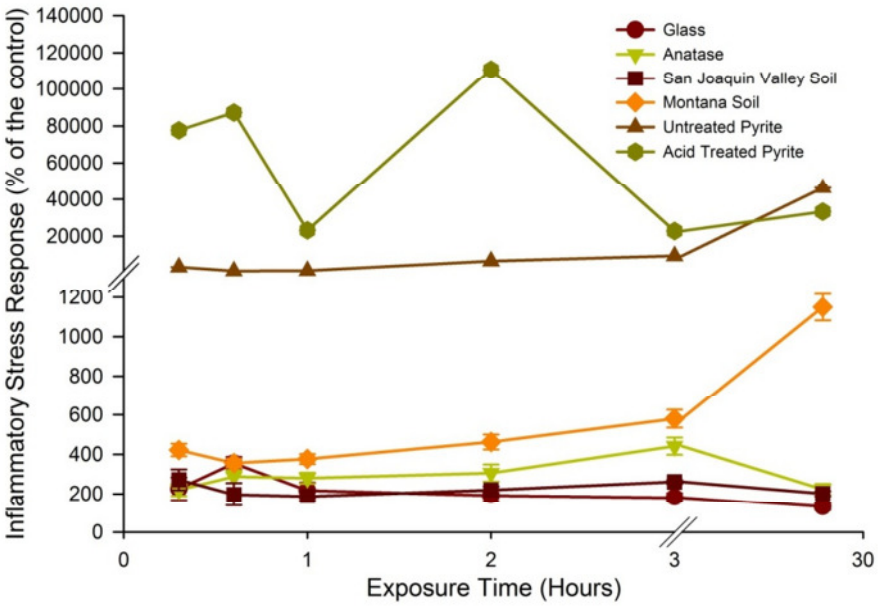

Figure 3.5. Evolution of ISR over time. The ISR over time generated by all the materials at the highest particle loading (0.002 m^2/mL) are represented. For some data points, the error bars are hidden by the symbols.

Chapter 4

Inflammatory Stress Response in A549 Cells as a Result of Exposure to Coal: Evidence for the Role of Pyrite in Coal Workers' Pneumoconiosis Pathogenesis

Andrea D. Harrington[1], Stella E. Tsirka[2] and Martin A.A. Schoonen[1]

[1] Department of Geosciences, Stony Brook University, Stony Brook, NY 11794-2100

[2] Pharmacological Sciences, Stony Brook University, Stony Brook, NY 11794-8651

Manuscript currently in review

4.1. Introduction

Colloquially referred to as black lung disease, coal workers' pneumoconiosis (CWP) is one of the most prevalent occupational diseases in the world. In the last decade of the twentieth century CWP accounted for half of the pneumoconiosis deaths in the United States [31]. Given that coal miners only constitute 0.02% of the total United States workforce, they represent an extraordinary high susceptibility group. Continued mechanization of underground mining and a shift to western coal fields, which contain less pyrite than Appalachian coal, is likely to diminish the prevalence of the disease among coal miners in the United States. However, coal production is rapidly expanding worldwide to satisfy the increasing energy demand. A 49% increase in production is estimated to occur between 2006 to 2030 [30]. Most of this expanded production is in East Asia, where mechanization and safety regulations are lagging those established in the United States. Hence, CWP prevalence is likely to increase worldwide.

Due to the biopersistence of quartz and the symptomatic similarities, CWP was originally classified as a variant of silicosis. However, a recent epidemiological study linked the prevalence of this disease to the presence of the mineral component pyrite in the coal [15]. By examining the occurrence of CWP throughout the United States and analyzing coal samples in respective locations, a strong positive correlation is seen between the incidence of CWP and content of bioavailable iron (BAI) in coal (predominately pyrite; correlation coefficient $r = 0.94$) [15]. In a separate study, a similar strong positive correlation is seen between the occurrence of CWP and

the pyritic sulfur content of coal (correlation coefficient r = 0.91) [11]. Furthermore, the ability of coal samples with variable pyrite contents to generate reactive oxygen species (ROS) was examined in earlier work. It was determined that not only does the amount of hydrogen peroxide increase with increasing pyritic sulfur content, but so does the coal's ability to generate hydroxyl radical (correlation coefficient r = 0.99) [11].

Pyrite generates ROS as a result of incomplete reduction of molecular oxygen as it oxidizes the metal sulfide in air-saturated fluids [35, 92, 108, 133]. Most studies on the oxidative dissolution of pyrite have been conducted in water. However, a recent study shows that the oxidation of pyrite in simulated lung fluid (SLF) also generates ROS [108].

The abiotic generation of ROS occurs in the oxidative dissolution of pyrite because molecular oxygen can only accept a maximum of two electrons in a single elementary electron transfer reaction. Spectroscopic, electrochemical, as well as theoretical studies show that the electron transfer to oxygen takes place at iron groups on the pyrite surface [53, 62, 138-141]. The electron withdrawal at the iron sites leads to the oxidation of sulfur at the surface and the formation of sulfur oxyanions elsewhere on the surface of this semiconducting mineral (Equation 1). The hydrogen peroxide produced in the reaction can then react with ferrous iron derived from the oxidative dissolution of pyrite (Equation 2) to form hydroxyl radical through the Fenton reaction (Equation 3). Besides reacting with hydrogen peroxide, ferrous iron can also react directly with dissolved molecular oxygen and generate superoxide (Equation 4), which can subsequently react with another ferrous iron to generate hydrogen peroxide (Equation 5). This last sequence of reactions is known as the Haber-Weiss reaction mechanism. Hence, both the reaction of dissolved molecular oxygen with the pyrite surface as well as the Haber-Weiss mechanism generate hydrogen peroxide, which then leads to hydroxyl radical. However, a competing reaction exists between ferric iron and hydrogen peroxide that converts hydrogen peroxide in water to dissolved oxygen, rather than hydroxyl radical (Equation 6) [133]. Taken together these reactions (Equations 1-6) promote the formation and decomposition of ROS and allow for the cycling of ferrous and ferric iron in oxygenated aqueous systems.

$$=FeS_2 + O_2 + H_2O \rightarrow H_2O_2 + =FeSSO \qquad \text{Eqn. 1}$$

$$2FeS_2 + 7O_2 + 2H_2O \rightarrow 2Fe^{2+} + 4SO_4^{2-} + 4H^+ \qquad \text{Eqn. 2}$$

$$H_2O_2 + Fe^{2+} \rightarrow Fe^{3+} + OH^- + {}^{\cdot}OH \qquad \text{Eqn. 3}$$

$$Fe^{2+} + O_2 \rightarrow Fe^{3+} + {}^{\cdot}O_2^- \qquad \text{Eqn. 4}$$

$$Fe^{2+} + {}^{\cdot}O_2^{-} + 2H^{+} \rightarrow Fe^{3+} + H_2O_2 \qquad \text{Eqn. 5}$$

$$3H_2O_2 + 2Fe^{3+} \rightarrow 2Fe^{2+} + 2H_2O + 2O_2 + 2H^{+} \qquad \text{Eqn. 6}$$

Besides pyrite-driven ROS formation, in human tissues ROS concentrations will increase as a normal cellular response to exposure to particulate matter, bacteria, and other foreign substances [111, 112]. While alveolar macrophage cells specialize in protecting the body in the case of an inhalation exposure [142], epithelial cells also upregulate ROS (predominately hydrogen peroxide) when challenged [111]. The degree of hydrogen peroxide upregulation is an indicator of cellular stress and can be quantified using the 2',7'-dichlorofluoroscein-diacetate (DCFH-DA) assay. Upon addition to the slurry, DCFH-DA is taken into a healthy cell and converted to DCFH. Once stressed, the cell generates ROS – hydrogen peroxide and hydroxyl radical – and DCFH is hydrolyzed to become fluorescent DCF [119].

Another measure of particle toxicity is the ensuing cellular death. There are a number of different assays that measure cell death or viability. For this study the cell viability assay 3-(4,5-dimethylthiazol-2-yl)-5-(3-carboxymethoxyphenyl)-2-(4-sulfophenyl)-2H-tetrazolium (MTS) is utilized. It works by quantifying the production of phenazine methosulfate (PMS), which generates formazan in the presence of tetrazolium. The concentration of formazan product in the system is directly proportional to the number of living cells. Since any living cell generates PMS regardless of its health status, high values in the MTS assay are only an indicator of immediate cell viability and does not predict future apoptosis.

Since the majority of lung illnesses originate in the epithelial cells lining the lungs [117, 118], the A549 human lung epithelial cell line is utilized here. This cell line, which is frequently used in toxicity studies [113-115], was first cultured in 1972 from the cancerous lung tissue of a 58 year old man. These adenocarcinomic human alveolar basal epithelial cells are easily cultured and proliferate quickly [116].

A previously published protocol describes a new procedure for cellular toxicity determination by utilizing the aforementioned assays in combination utilizing the A549 cell line [143]. Defined as the formation of ROS within the A549 epithelial cell normalized to cell viability measurements, the inflammatory stress response (ISR) allows for a meaningful comparison of ROS generation in different biological replicates of the cell culture experiments and accounts for the presence of cell death as a result of the exposure. By measuring the

upregulation of ROS and the viability of the cells we gain insight into the immediate toxicity of the treatment on the cells as well as the state of the remaining viable cells.

The objective of this paper is to evaluate the hypothesis that the inhalation of coal containing pyrite leads to inflammation in the human lungs. This hypothesis builds on earlier work that shows that pyrite, by itself, can generate ROS in water and SLF [108, 133] as well as upregulate ROS formation in epithelial cells [143]. ROS upregulation in cells results in cellular oxidative stress [83, 86, 89]. Ultimately, chronic cellular stress can lead to tissue damage and disease, such as CWP [144]. In this study, the upregulation of ROS and viability of epithelial lung cells are determined after exposure to several coal reference materials with known amounts of pyrite.

4.2. Materials and Methods

4.2.1. Mineral sample preparation and soil standards

Five coal reference standards were obtained from The National Institute of Standards and Technology (NIST). The coal reference standards (NIST #1635, 2682b, 2692b, 2684b and 2685b) contain different amounts of pyrite (expressed as pyritic sulfur mass fractions), see Table 1. The specific surface area for each of the coal reference standards was determined using a Quantachrome NOVA 5-point BET analyzer using UHP N_2 gas. The results are summarized in Table 1.

4.2.2. Culturing and Plating the A549 Human Lung Epithelial Cell Line

The A549 human lung epithelial cell line was cultured and plated using a previously published procedure [143]. Briefly, cells were plated in Ham's F12K Media containing 10% Fetal Bovine Serum (FBS) and 1% 1X Penicillin/Streptomycin (cell growth media). Once confluence was reached, the cells were passaged at 1 x 10^5 cells/mL using trypsin with EDTA to detach the cells. The cells were then counted using the Trypan blue stain on a hemocytometer. Wells in columns 3 through 10 of the 96-well microplates were loaded with 8 x 10^4 cells/mL, covered with a microplate lid, and allowed to incubate at 37˚C in culturing media for approximately two days until confluent. Due to background signal generated by the assays, columns 1 and 2 as well as 11 and12 were kept cell free for normalization. All work with cells took place in a sterile hood to avoid airborne bacteria that would affect the results. When not in

the hood, the microplate lid was kept on at all times. Temperature, relative humidity and carbon dioxide (CO_2) concentration in air were kept constant (37˚C, 95% and 5% CO_2 in air, respectively) in the incubator.

4.2.3. Inflammatory stress response measurements

Cellular confluence was achieved after incubation in 96-well microplates for two days. The cell growth medium was discarded and a previously published protocol for determining ISR was employed [143]. In brief, after all liquid contents were allowed to drain out (cells remain attached), columns 1 through 6 were filled with 200 µL of 50 µM DCFH-DA (from Sigma Aldrich) in Hank's Buffered Salt Solution (HBSS) and columns 7 through 12 were filled with 200 µL HBSS, and then placed in the incubator. During incubation, four serial dilutions of the contaminant slurries were made. All final dilutions were normalized to surface area. The stock solution contained 0.002 m^2 contaminant/mL HBSS. After incubating for 20 minutes, all liquid contents of the microplate were again discarded. 200 µL of the contaminant slurry was added to the plates as shown in Figure 1. Rows A and H were kept free of contaminants due to edge effects [124]. Row B was kept free of particles for normalization (control). After slurry addition, 20 µL of MTS (from Promega) was added to all wells in columns 7 through 12. The plate was then placed in the incubator for 30 minutes before the first analysis. Since each 96-well microplate contained assays for both cellular generated ROS and cell viability, duplicating the plates allowed for 8 replicates for each loading.

DCFH-DA is a fluorometric probe used to determine cellularly derived ROS and was analyzed using Thermo Scientific's Fluoroskan Ascent. MTS is a colorometric probe used to determine cell viability and was analyzed using Molecular Devices' SpectraMax 340PC384. The microplates were kept in the incubator at all times other than for analyses. During periods before analysis and transport, microplates were kept in the dark using foil. Plates were analyzed at 30 minutes, 1 hour, 2 hours, 4 hours, 8 hours and 25 hours.

4.3. Results

The design of the experiment allowed for six particle loadings (including a control) to be evaluated. In addition, by taking measurements at fixed times for up to 24 hours we are able to record temporal changes in cell viability, ROS production, and, hence, ISR. In a separate study

we applied this protocol to a number of minerals and standard soils [143]. Those earlier results are useful in placing the cellular response to coal in context.

Coal reference material number 1635, which contains no pyrite, generated a relatively linear increase in ISR with particle loading. The peak ISR occurred with the highest particle loading and at the 30 minute time point. This ISR maximum is more than threefold greater than the control. A common temporal trend is exhibited with an initial ISR followed by a drop and then a steady ISR increase [143]. Coal reference material numbers 2682b and 2692b generated the lowest ISR (175 and 251 % of the control, respectively). However, the temporal trends in ISR are different. While coal reference material number 2682b increased steadily with time, number 2692b reacts similar to coal reference number 1635 by first generating a higher ISR followed by a dip and a gradual and steady increase. Of the three coal reference materials, number 1635 is the only one that caused significant cell death (59 % of the viable cells compared to a control at 30 minutes), which subsided with time, although it is responsible for the high ISR. While initially the ISR for coal reference material number 1635 is driven by low cell viability, eventually it is driven by ROS upregulation.

Coal reference material numbers 2684b and 2685b, containing the highest pyritic sulfur contents, generated the greatest ISR (798 and 1426 % of the control). Although number 2685b generated an ISR nearly a factor of two greater than 2684b, the temporal trends of these reference coals are similar. Generating similar ROS upregulation, the disparity in ISR is derived by the greater amount of cell death in the sample containing the most pyritic sulfur (67 versus 43 % of the viable cells when compared to a control at 24 hours)

4.4. Discussion

The 4.6 fold ISR difference between the coal containing no pyrite and coal containing the highest concentration of pyrite supports the hypothesis that the reactivity of pyrite in the coal plays an important role in the pathogenesis of CWP. The much lower ISR for reference material number 1635 is somewhat lower than the stress generated by glass beads and anatase, which are considered relatively inert materials [143]. Therefore, exposure to coal without pyrite generates the same level of response as exposure to inert particulate matter. This is consistent with the fact that there is a low prevalence of CWP among miners who are exposed to coal without pyrite [15].

Coal reference material number 2684b, containing the second highest concentration of pyrite, generated 2.6 fold the ISR of the sample 1635. Coal reference material number 2685b generated nearly twice the ISR as coal reference material number 2684d. It is important to note we have normalized to total surface area and not the surface area of the pyrite within the standard reference material. Therefore, one would not necessarily expect a linear increase in ISR with increase pyritic sulfur contents. The amount of "available" iron, or total iron released in 1.5 mg/L RNA solution over a 7 hour period, would also contribute to Fenton chemistry [11]. The high available iron content of reference material number 2684b (a factor of 17.3 greater than of number 2692b and 62% of number 2685b) likely plays a role in the increased ISR, which may be an indication of the accessibility and reactivity of the pyrite within the coal.

4.5. Conclusion

CWP is a protracted disease caused by chronic inflammation in the lungs induced by inhaled coal particles. This study builds upon and extends earlier acellular [108] [11] and epidemiological work [15] citing pyrite as the major contributing factor in CWP pathogenesis. Specifically, our data shows that epithelial cells challenged with coal containing modest amounts of pyrite (0.52 and 1.15 wt. %) undergo cell death, and the remaining surviving cells show an upregulation of ROS allowing for a dramatically high ISR (798 % and 1426 % compared to a control, respectively). These findings support the notion that pyrite is a key determinant the pathogenesis of CWP.

Table 4.1. Certified NIST elemental analysis of standard reference material

	Standard Reference Material Number[a]				
	1635	2682b	2692b	2684b	2685b
Origin	Erie, CO	Gillette, WY	Holden, WV	Marion, IL	Captina, WV
Coal Type	Subbituminous	Subbituminous	Bituminous	Bituminous	Bituminous
Surface Area (m^2/g)[b]	1.79	4.94	1.35	2.11	1.72
Pyritic Sulfur (mass fraction)[c]	0.00	0.01	0.49	0.52	1.15
Iron Release (µM)[d]	0.00	0.02	0.48	8.31	13.3
Elemental Analysis[e]	Mass Fraction (wt. %)				
Iron	0.239 ± 0.005	0.24	---	1.5	3.9
Sulfur	0.3616 ± 0.0017	0.4917 ± 0.0079	1.170	3.076 ± 0.031	4.730 ± 0.068
	Mass Fraction (µg/g)				
Arsenic	0.42 ± 0.15	1.0	---	3.9	12
Chromium	2.5 ± 0.3	15	---	17	22
Manganese	21.4 ± 1.5	26	---	36	41
Mercury	0.0109 ± 0.0010	0.1088 ± 0.0029	0.1333 ± 0.0041	97.4 ± 4.7	146.2 ± 10.6
Zinc	4.7 ± 0.5	8.6	---	110	17

[a] National Institute of Standards and Technology sample numbers
[b] BET surface area values are for coals as received and used in experiments, not desiccated
[c] dry basis
[d] 0.125 m^2/L coal loadings, total iron [i.e. Fe(II) and Fe(III)] after 7 hours in 1.5 mg/L RNA solution [11]
[e] National Institute of Standards and Technology - Certified Analysis [145-149]

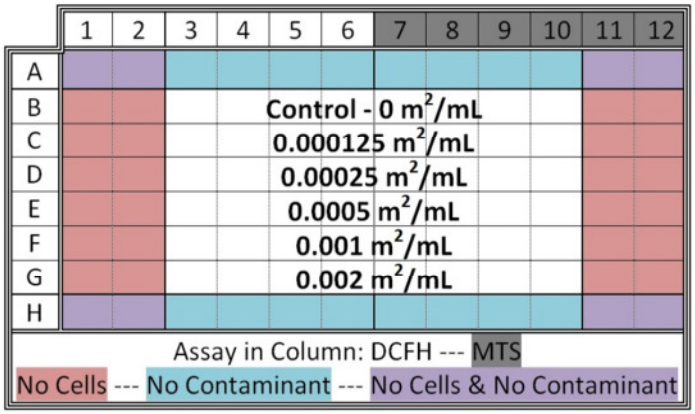

Figure 4.1. Schematic of 96-well microplate for cellular study. The arrangement for all microplates in this study is shown. The positioning of control wells, assay distribution and particle loadings are highlighted. For each material tested two identical plates were evaluated at the same time. Hence, for a given mineral and loading, the ROS level and cell viability was determined in 8 replicate wells.

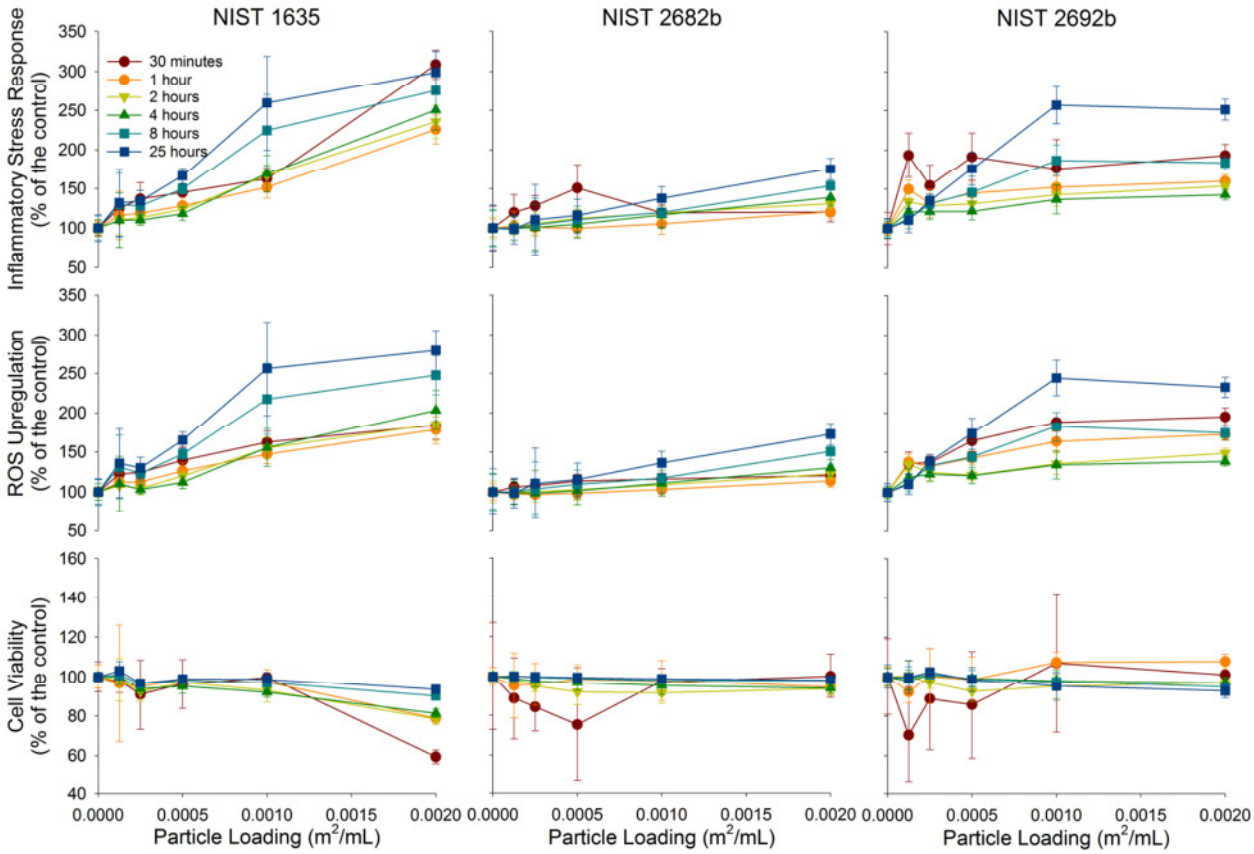

Figure 4.2. ROS upregulation, cell viability and ISR of A549 cells generated by unreactive coal samples. The cellular response to the three coal samples with increasing particle loading are presented, all normalized to a control. The samples, NIST 1635, 2682b and 2692b have the lowest pyritic sulfur contents.

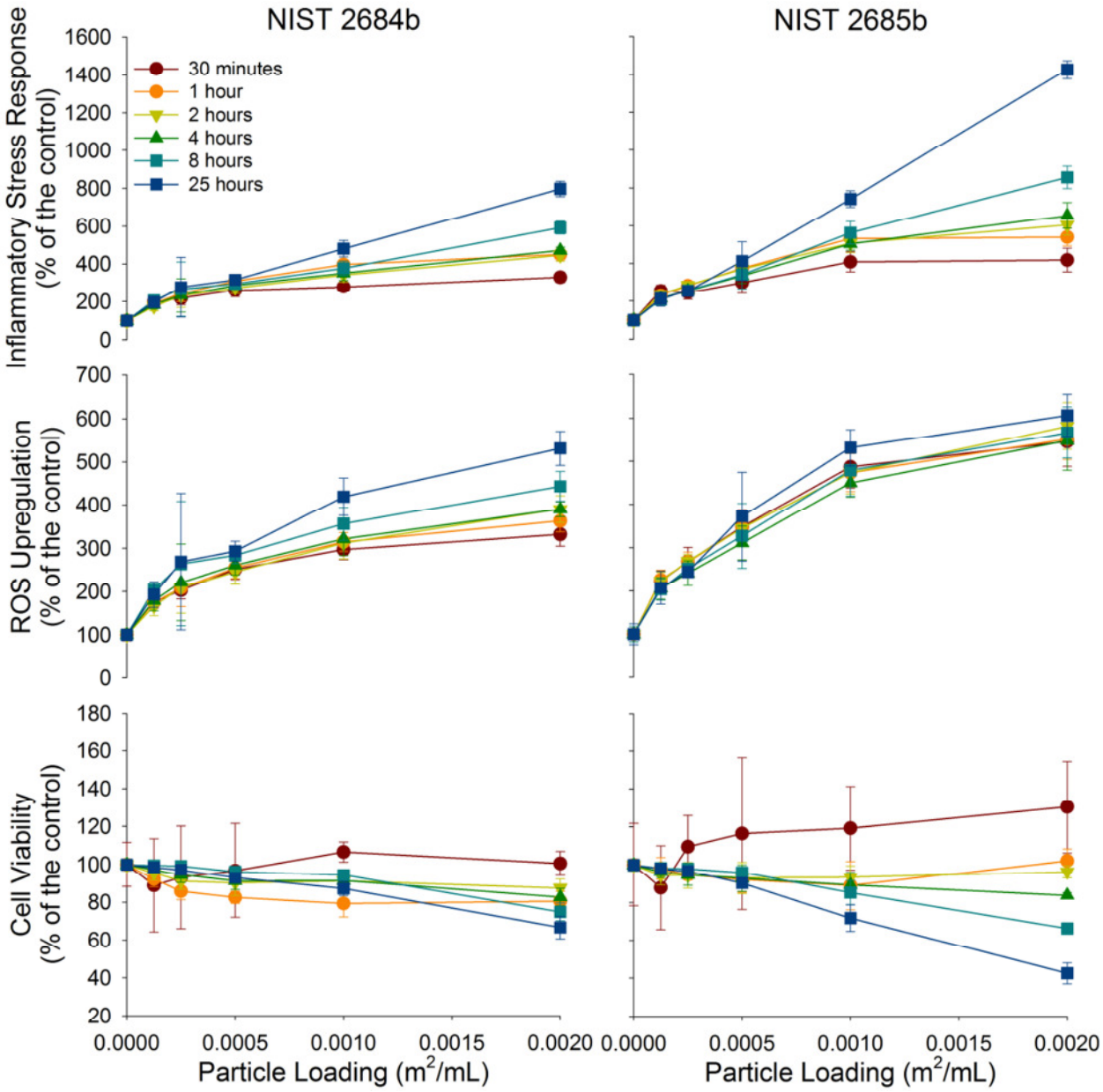

Figure 4.3. ROS upregulation, cell viability and ISR of A549 cells generated by reactive coal samples. The cellular response to the two coal samples with increasing particle loading are presented, all normalized to a control. The samples, NIST 2684b and 2685b have the highest pyritic sulfur contents.

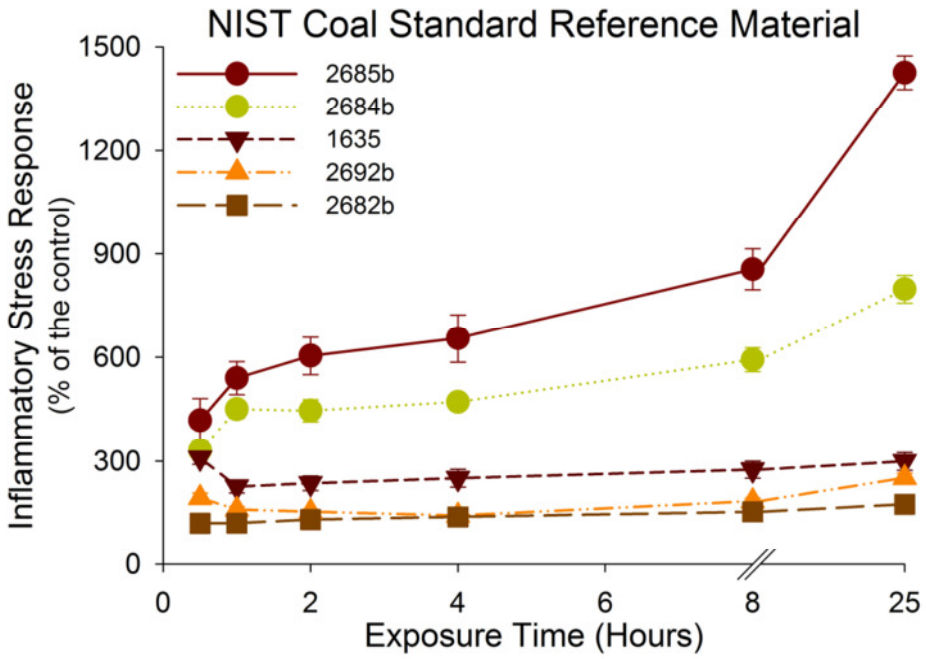

Figure 4.4. Evolution of ISR over time generated by NIST coal samples. The ISR generated over time by all the coal samples at the highest particle loading (0.002 m^2/mL) are represented. For some data points, the error bars are hidden by the symbols.

Chapter 5

Metal-Sulfide Mineral Ores, Fenton Chemistry and Disease: Particle Induced Inflammatory Stress Response in Lung Cells

Andrea D. Harrington[1], Alexander Smirnov[2], Stella E. Tsirka[3] and Martin A.A. Schoonen[1]

[1] Department of Geosciences, Stony Brook University, Stony Brook, NY 11794-2100

[2]Department of Earth and Marine Sciences, Dowling College, Oakdale, NY 11769.

[3]Pharmacological Sciences, Stony Brook University, Stony Brook, NY 11794-8651

5.1. Introduction

From flint in the Neolithic period, gold and silver in the Iron Age, lead during Antiquity, to Rare Earth minerals in the present, mining of mineral resources has enabled important technological advances, fostered trade, as well as provided the raw materials for the creation of art and artifacts. Presently, mining of metals and mineral ores is a multibillion dollar industry, with metals and aggregates/industrial minerals generating a $230 billion annual profit [150]. While a crucial pillar of our society, mining of mineral resources has significant environmental and health issues associated with it. Exposure to mine dust has long been recognized as an occupational health hazard. Historically, exposure to quartz, asbestos particles and coal dust has received considerable attention given the prevalence of silicosis, asbestosis and coal workers' pneumoconiosis worldwide. However, far less is known about the inhalation risks associated with other earth materials that are mined and processed. While there have been some studies about the role of Fenton chemistry in the development or enhancement of disease [151], there is much to be explored. The purpose of this study is to investigate the toxicity of common metal-sulfide minerals (copper-sulfides, copper-iron-sulfides, arsenic-iron-sulfide, lead-sulfide, and zinc-sulfides) that are mined or present in ore deposits as gangue minerals. Each of the materials evaluated is briefly described below.

5.1.1. Selected Metal-sulfides

Sphalerite (ZnS) is the main zinc ore mineral and commonly contains 26 mole % iron in its crystal structure ($Zn_{1-x}Fe_xS$) [152, 153], with reports of up to 56 mole % [154, 155]. Often associated with sphalerite, galena (PbS) is the main lead ore mineral. The cations for both ores are present in the divalent oxidation state. While arsenic is no longer mined, its main ore mineral, arsenopyrite (FeAsS), is often found in gold ores. As a result, a considerable amount of arsenopyrite is processed in the mining of gold. The oxidation state of iron in arsenopyrite is predominantly divalent (i.e., $Fe^{2+}(AsS)^{-2}$) with a minor contribution of trivalent iron (i.e, $Fe^{3+}(AsS)^{3-}$). Although the presence of either an arsenic and sulfur dianionic or trianionic group in the crystal structure is debated, when dispersed in solution, arsenopyrite releases ferrous iron [156]. This suggests that iron in the arsenopyrite crystal structure is mostly in the divalent oxidation state. The oxidation states of copper and iron in chalcopyrite ($CuFeS_2$), the primary copper ore mineral, has been extensively studied. Most studies indicate that the copper present is monovalent, although in oxidized surface layers divalent copper may be prevalent. To balance charge, trivalent iron is formally present in chalcopyrite, but charge transfer between iron and sulfur gives iron a strong divalent character [157, 158]. Furthermore, as with arsenopyrite, chalcopyrite releases ferrous iron into solution, which is important in the context of this study as the release of ferrous iron will allow the Fenton reaction to go forward:

$$H_2O_2 + Fe^{2+}(aq) \rightarrow OH^- + {}^{\cdot}OH + Fe^{3+}(aq) \quad (1)$$

Pyrite (FeS_2), as the most common sulfide mineral on Earth (and a potent reactive oxygen species generator [11, 92, 133]), is often associated in varying abundances with all the ores described above.

Chalcocite (Cu_2S) and bornite (Cu_5FeS_4) are also important copper ores and are common weathering products of chalcopyrite. While copper in chalcocite is monovalent, it is possible that bornite contains a small amount of divalent copper as well. Iron in bornite has a formal trivalent oxidation state [157].

5.1.2. Particle Toxicity

The toxicity of particles can be derived by particle overload or from the reactivity of the material [41, 42, 83]. When particle overload occurs, the alveolar macrophage (AM)-mediated

clearance is impaired, which leads to an accumulation of particles within the lungs. An excessive particle burden can cause an array of pulmonary issues, ranging from chronic inflammation and fibrosis, to the development of tumors [42]. Once inhaled, a mineral particle might undergo surface-mediated reactions, including dissolution reactions [83, 92, 108, 159]. The reactivity of an inhaled particle is a function of its stability in the lung environment, its solubility, and modifications of its surface, such as the presence of defects or surface coatings [83, 92, 159]. The incomplete reduction of oxygen on the surface of the particles or by metals released from the particles will generate reactive oxygen species (ROS) [92]. Furthermore, although tightly regulated, cells also generate ROS when under stress, possibly contributing to the oxidative stress [27, 160, 161]. Apart from oxidative damage, reactive materials also impair AM-mediated clearance at a lower lung burden, thus adding to the inflammation. The concomitant disruption of efferocytosis (clearance of apoptotic cells via phagocytosis) creates a delayed "secondary" necrosis [42, 162, 163]. Unlike apoptosis (programmed cell death), which controls potentially damaging inflammation by not releasing the contents of the cell into the surrounding environment, necrotic cell death adds to the burden on the body and can have a negative cascading effect [162, 164]. Therefore, while exposure to reactive foreign material alone can also generate necrotic cell death [143], inhibition or reduced efficiency in efferocytosis exacerbates the problem.

A number of toxicity markers can be utilized to evaluate the effect of particle exposure on lung cells [160, 165-167]. The approach developed by Harrington et al. (2012) takes into account the possible complexity of immune responses to foreign materials in the body by capturing the immediate and short-term inflammatory stress response (ISR) generated by exposure to a contaminant [143]. The ISR is the normalization of the cellular upregulation of ROS with respect to the cell viability. It not only allows for overall stress levels to be evaluated but each component as well. Due to the relatively short time course of the exposure, the cell viability is a measure of necrotic cell death. Whereas the amount of cellular ROS upregulation is not only a marker of immediate cellular stress, but also may indicate future apoptotic cell death [168, 169].

By focusing on the ISR, a better understanding of the inflammatory nature of a material can be established, although the specific biological pathways interrupted by the material cannot be resolved without additional studies. In this study, the protocol developed by Harrington and

coworkers is used to compare the ISR for eight common metal-sulfide ore minerals. The results allow for direct comparison between materials, which is the basis for an evaluation whether structure and chemistry of (earth) materials are important determining factors in toxicity.

The cell culture work in this study is complemented by an assessment of the generation of $^{\cdot}OH$ and H_2O_2 by the metal-sulfides when dispersed in water in the absence of an epithelial lung cell line. This acellular test provides insight in purely mineral-driven ROS formation, which can be useful in the interpretation of ISR data. It is hypothesized, that the ability of metal-sulfide minerals to generate ROS when dispersed in water will contribute to elevated ISR. Furthermore, we expect that minerals containing ferrous iron, and to a lesser extent monovalent copper, will produce more ROS when dispersed in water as a result of their ability to promote the Fenton reaction (eq. 1). It should be pointed out, however, that materials that do not form ROS when dispersed in water, e.g. glass beads, will elicit a modest cellular upregulation of ROS within epithelial cells [143]. This is the result of the immune response of epithelial cells to any foreign substance. Metals released from the mineral particles may also lead to interference of biochemical processes in the cell and contribute to a loss of cell viability [18], which would lead to higher ISR values independent of the ability of the mineral to generate ROS when dispersed in water.

5.2. Materials and Methods

5.2.1. Mineral sample preparation

Eight natural metal-sulfide ore minerals, obtained from Wards (Rochester, NY), were investigated. The samples include three zinc sulfides with variable iron contents, one copper sulfide, two copper iron sulfides, a lead sulfide, and an iron arsenic sulfide (Table 1). All samples were ground and sieved to obtain a suitable respirable fraction. The materials were characterized using a suite of complementary techniques.

The mineralogical composition of samples was determined by X-Ray Diffractometry (XRD) using a Scintag PAD X diffractometer under the following conditions: $CuK_{\alpha 1}$, 40kV, 25 mA, 5° – 75° 2Θ, step 0.02° 2Θ and counting times of 5-10 seconds per step. The mineralogy of the materials used in this study is summarized in Table 1. Trace metal composition of the materials was determined using X-ray Fluorescence (XRF). An aliquot of the ground material was pressed into an 18mm tablet with high-purity cellulose as binder. The XRF analysis was

conducted on a Brüker Pioneer wavelength-dispersive XRF spectrometer in standardless mode, which means that the XRF intensities were converted to concentrations on the basis of a physical X-ray absorption model provided with the instrument. The XRF results are summarized in Table 2 along with nominal major element concentrations based on ideal mineral compositions. It is important to note that the pressed tablet method is not suitable for major element determination, hence the inclusion of nominal major element concentrations in this table.

Specific surface area was determined for each material, because the exposure experiments are normalized with respect to surface area. Specific surface area (m^2/g) of each sample after grinding was determined using gas adsorption measurements. The measurements were conducted on a Quantachrome NOVA 2200e BET instrument, employing a 5-point BET isotherm ($r^2 = 0.999$), with Ultra-High Purity N_2 as adsorbate. The specific surface area of all metal-sulfides evaluated in this study are summarize in Table 1.

5.2.2. Acellular Hydroxyl radical and Hydrogen Peroxide Formation

The formation of ˙OH and H_2O_2 was determined using the protocol developed by Cohn et al. (2009) [57]. The protocol is based on the conversion of non-fluorescent 3 '-(p-Aminophenyl) fluorescein (APF) to fluorescein, which is strongly fluorescent. The APF probe reacts with ˙OH but not with H_2O_2; however, with the addition of horseradish peroxidase (HRP), H_2O_2 becomes reactive and can be quantified using APF. Hence, by conducting two complementary experiments, one without HRP and one with HRP, both ˙OH and ˙OH + H_2O_2 formation can be determined. It is important to note that the APF probe records the cumulative formation of either ˙OH (without HRP) or ˙OH + H_2O_2 (with HRP) over the duration of the experiment. Hence, the APF protocol does not provide an analysis of the concentration of these ROS at any given time during the experiment. Furthermore, fluorescein formed in the experiment will be (partially) degraded if the production of either ˙OH or H_2O_2 exceeds the available amount of APF in the experiment. Therefore, insufficient amounts of APF probe in the experiment will lead to an underestimation of the amount of ˙OH or ˙OH + H_2O_2 formed.

Two sets of experiments with APF were conducted. In a first set, an appropriate amount of each of the sulfides were weighed into 3 mL polyethylene snap-top tubes to provide a surface loading of about 10 m^2/L. Water kept in an amber plastic bottle for at least 30 days to minimize background H_2O_2 levels was added to the minerals by micropipette (2964 µL in experiments

without HRP or 2844 µL in experiments with HRP). Subsequently, 30 µL of phosphate buffer was added, followed by 6 µL of APF. In the experiments with HRP, 120 µL of HRP was added as a final reagent. The tubes were capped, placed on a vortex mixer for 15 second to mix the reagents, and then transferred to a Labquake orbital shaker, which continuously mixed the mineral slurries by rotating end-over-end. The entire orbital shaker was kept in the dark to prevent photochemical degradation of the APF probe or fluorescein. After 26 hours of mixing, the tubes were removed from the orbital shaker, filtered over Teflon micro-membrane filters with a pore size of 0.22 µm, and the fluorescence was measured on a Turner Design instrument, equipped with 490 (excitation) and 520 (emission) filters. A calibration curve made by diluting a 1 mM H_2O_2 stock solution and reacting it with APF and HRP [57]. The fluorescence values recorded for the mineral slurries was converted to H_2O_2 equivalents and expressed as nM/m^2.

Three minerals, chalcopyrite, galena, and arsenopyrite were studied further by conducting a series of shorter duration experiments to determine the evolution of $^{\cdot}OH + H_2O_2$ over time. In these experiments, the volume of APF probe molecule added was increased to 12 µL and the amount of water added was lowered by 6 µL. The volumes of buffer and HRP remained the same. The same volume adjustments were made for the experiments to determine the calibration curve. The additional volume of APF was needed to prevent the probe molecule from becoming exhausted as a result of high amounts of $^{\cdot}OH + H_2O_2$ formed in some experiments. Details on the preparation of the various stock solutions are provided in previous work [57].

5.2.3. Culturing and Plating the A549 Human Lung Epithelial Cell Line

A previously published protocol was utilized for the culture of the A549 human lung epithelial cell line [143]. The cell were maintained in 10% Fetal Bovine Serum (FBS) and 1% 1X Penicillin/Streptomycin in Ham's F12K Media. Cell work was performed in a sterile hood. The cells were kept in an incubator at standard conditions (37˚C, 95% and 5% CO_2 in air, respectively). For passage and counting purposes, once confluent, the cells were detached using trypsin with ethylenediaminetetraactic acid (EDTA). Trypan blue was the staining agent used in conjunction with a hemocytometer for cell quantification. Cells were loaded into 96-well microplates at 8 x 10^4 cells/mL. However, columns 1, 2, 11, and 12 were kept cell free for normalization purposes. When not in the hood, a lid was kept on the microplate.

5.2.4. Inflammatory Stress Response Measurements

To determine the ISR generated in the A549 cells by mineral samples a protocol developed by Harrington et al. was used [143]. In brief, 2',7'-dichlorofluoroscein-diacetate (DCFH-DA) assay from Sigma Aldrich and 3-(4,5-dimethylthiazol-2-yl)-5-(3-carboxymethoxyphenyl)-2-(4-sulfophenyl)-2H-tetrazolium (MTS) from Promega were utilized concomitantly for cellular ROS upregulation and viability quantification, respectively. All mineral slurries were normalized to surface area with the stock solution containing 0.002 m^2 mineral contaminant /mL Hank's Buffered Salt Solution (HBSS). Each experiment was replicated by using two identically prepared 96-well plates; therefore for each mineral contaminant there were eight wells for each particle loading allowing for a robust data set. Particle loadings were elevated to highlight differences in reactivity and do not necessarily represent typical exposure concentrations. Given ambient air and occupational health standards, the lower loadings utilized in the study (i.e. 0.00025 m^2/mL) better represent actual exposure concentrations [170, 171].

The first analysis occurred after a 30 minute exposure, followed by 1 hour, 2 hours, 4 hours, 8 hours and 24 hours. ROS upregulation measurements were made using Thermo Scientific's Fluoroskan Ascent and cell viability measurements were made on a Molecular Devices' SpectraMax 340PC384, since DCFH-DA is a fluorometric assay, while MTS is a colorimetric probe. The microplates were covered with foil during transport to minimize exposure to light.

5.3. Results

The metal-sulfides studied here show a wide range of results in terms of both acellular ROS formation and ISR. The results of the acellular and cellular work are presented in two separate sections for clarity.

5.3.1. Acellular ROS formation

Of the metal-sulfides tested here, chalcopyrite, galena, and arsenopyrite show significant amounts of $^{\cdot}OH + H_2O_2$ formation when dispersed in water compared to all other sulfides studied (Table 3). A subsequent set of experiments aimed at determining the $^{\cdot}OH + H_2O_2$ production within shorter time frames showed that the recorded value for the 26-hour production

of ˙OH + H_2O_2 in the chalcopyrite slurry is an underestimate because the ˙OH + H_2O_2 production exceeded the amount of APF probe available for reaction. Of the sulfides studied, chalcopyrite also produces the highest amounts of ˙OH. Two of the sphalerite samples did not produce a high enough fluorescence signal to quantify the amount of ˙OH formed. The sphalerite from China was also below the detection limit for ˙OH + H_2O_2. The sphalerite sample from the United States recorded very low values for both ˙OH and ˙OH + H_2O_2 despite its high iron content.

The results of a second set of experiments with chalcopyrite, galena, and arsenopyrite in which the amount of APF was increased and the reaction time shortened are presented in Figure 1. The results with chalcopyrite showed that the production of ˙OH + H_2O_2 started immediately and led to the generation of µM levels of ˙OH + H_2O_2 within an hour. By contrast, the buildup of ˙OH + H_2O_2 was slower in galena and arsenopyrite slurries and the levels attained were well below those attained in chalcopyrite slurries. These data indicate that chalcopyrite, when dispersed in water, will trigger a burst of H_2O_2, a part of which will convert to ˙OH.

5.3.2. Cellular Response

The ISR and cell viability data of all eight natural metal-sulfide ore minerals are presented in Figure 2. The three different sphalerite samples had little or no effect on cell viability and low levels of ROS upregulation, resulting in low ISR values. In fact, their response was comparable to glass beads and anatase, which are considered relatively inert or unreactive (Table 4). By contrast, the copper sulfide minerals bornite, chalcopyrite, and to a lesser extent chalcocite showed a significant loss in cell viability combined with ROS upregulation in the remaining viable cells, leading to high ISR values. Galena also showed a significant loss of cell viability, but the ISR values were comparable to those of chalcocite. Arsenopyrite generated a modest loss of viability combined with little ROS upregulation, as a result the ISR values were comparable with materials that are considered inert or unreactive, such as glass beads and anatase. The experimental design allows for not only a range of particle loadings to be evaluated but, by taking reading between 30 minutes after exposure to 24 hours, it is possible to evaluate the changes in ISR over time. These temporal variations as well as more details for each type of metal-sulfide are presented below. To place the results obtained in this study into context, the results were compared to standard reference materials as well as relatively inert material and pyrite that have been evaluated using the same protocol [143], see Table 4. Below, the results for

each of the materials tested are described. Unless otherwise stated, the ISR values mentioned below refer to those associated with experiments at the highest particle loading (0.002 m^2/mL).

5.3.2.1. Zinc Sulfides

The three sphalerite samples contain different amounts of iron (Spain-Picos de Europa, 0.154 wt. %; China-Yu Chen, 0.189 wt. %; and USA-Balmat, 6.603 wt. %) and represent a compositional variation that is well within the range of iron content recorded for natural sphalerite. Overall, as mentioned above, these three sphalerite samples do not elicit a strong inflammatory response, nor do they elicit a significant sustained loss of cell viability. However, they do show a difference in how they respond through time (Figure 3). The maximum ISR occurred at 1 hour for the Yu Chen sample, compared to 4 hours for the Picos de Europa sample, and 24 hours for the Balmat sample. Of the three sphalerite samples, the sample from Picos de Europa generated the greatest ISR of the sphalerite samples at 362 % of the control. Given that the cell viability does not drop below 85%, the ISR is mostly a result of the upregulation of ROS within the cells. However, the upregulation is modest compared to the copper sulfides and on par with that seen for glass beads.

5.3.2.2. Copper Sulfides

Chalcocite, the only iron-free copper sulfide investigated, generated the lowest ISR of the group at 3,408 % of the control. This high stress response was caused by both a drop in cell viability (39 % of the control at 24 hours) and a high ROS upregulation. Chalcopyrite, the most reactive mineral of the copper sulfides and all metal-sulfides tested here, generated an ISR of 86,024 % of the control at the 2 hour time point. However, by 24 hours the ISR decreased to 27,370 % of the control (Figure 3). While there was significant ROS upregulation, these ISR values are driven to extremes given the low cell viabilities (1.7 % of the control at 2 hours and 3.3 % at 24 hours). Bornite, generating an ISR value of 40,918 % of the control at the 8 hour time point, also resulted in extremely low viability (2.8 % of the control). Since exceedingly low cell viabilities at the highest particle loadings distort the ISR values, it is more meaningful to focus on the response at lower loadings. All copper sulfides cause high ISRs under moderate (0.001 m^2/mL) particle loadings (Figure 4). The inflammatory stress generated by chalcocite and bornite increased with time, generating ISR values of 1,079 and 1,727 % of the control,

respectively; while the toxicity of chalcopyrite decreased with time (3,168 % of the control at 30 minutes and 888 % of the control after 24 hours).

5.3.2.3. Lead Sulfide

Galena generated a maximum ISR after 30 minutes of exposure (3,194 % of the control for highest loading). This ISR was caused by the immediate and dramatic drop in cell viability (down to 3.5 % of the control), while the ROS upregulation remained essentially unaffected (110 % of the control). After this initial high ISR value, a steady decrease in ISR was observed over the first 8 hours period as a result of recovery of cell viability (27 % of the control at 8 hours). However, at 24 hours the ISR increased slightly (405 % of the control) with the decrease in cell viability (20 % of the control). Given the low viability of the cells at the 30 minutes time point at the highest particle loading, the moderate particle loading was also examined. With a cell viability of 73 % of the control and an ROS upregulation of 115 % of the control, the ISR was only at 157 % of the control. However, the viability decreased to 44 % of the control at 24 hours.

5.3.2.4. Iron Arsenic Sulfide

The arsenopyrite tested here elicited only a modest inflammatory response. The response was more pronounced than that for the three sphalerite samples but comparable with a NIST San Joaquin Valley soil with baseline trace metal contents (Table 4). The highest ISR generated by the arsenopyrite was 476 % of the control at 24 hours. The ISR did not increase steadily with time. The ROS upregulation and cell viability consistently decreased with increasing exposure time. The viability ranged from 102 % of the control at 30 minutes and 37 % of the control at 24 hours. Under moderate particle loading, the ISR generated by arsenopyrite was slightly higher than that generated by galena, although the cell viability was nearly twice as high (73 % of the control) at 24 hours.

5.4. Discussion

The metal-sulfide ore minerals investigated in this study generated a wide range of ISR values and only chalcopyrite produced both substantial amounts of H_2O_2 and $^{\cdot}OH$ when dispersed in water. Since the ISR is derived by normalizing the cellular upregulation of ROS by the cell viability, it can be elevated by not only high ROS upregulation but also low viability.

While this study focuses on evaluating ISR generated by the exposure to common ore minerals, the origin of the stress is important because it can point to different mechanisms by which exposure to these types of materials may affect human health. Furthermore, understanding the type of cell death generated can make a difference in treatment [164].

The copper sulfides elicit by far the most pronounced cellular response. The recorded ISR values are predominately driven by necrotic cell death. In fact, the loss of cell viability generated by bornite and chalcopyrite is so immediate and resounding at the highest particle loading (0.002 m^2/mL) that the cells are not able to recover at all during the 24 hour period (Figure 2). In fact the ISR values for chalcopyrite are higher than those seen in experiments with pyrite that was not acid washed (Table 4) [143]. When experiments with moderate particle loadings (0.001 m^2/mL) of chalcopyrite or bornite are considered, the viability among cells exposed to chalcopyrite actually increases with time (from 17% to 78% confluence), while the viability of cells exposed to bornite stays relatively stable (75±7%). In other words, at the 0.001 m^2/mL loading level, exposure to chalcopyrite leads to a significant immediate loss of cell viability followed by a rebound, while such an effect is not seen in the experiments with bornite.

It is possible that the difference in cell viability is related to the spontaneous generation of ROS by chalcopyrite when dispersed in water (Figure 1). Unlike chalcopyrite, bornite shows little or no ROS generation when dispersed in water (Table 3). Although low cellular viabilities, particularly at the highest concentration, drive up the ISR values, the chalcopyrite and bornite particles also generate a strong upregulation of ROS within the cells. This indicates that the remaining cells are likely in the early stages of apoptosis. At a loading of 0.001 m^2/mL, the ISR values for bornite in the first 4 hours are similar to those determined for chalcocite, galena, and arsenopyrite (Figure 4). After 8 to 24 hours, there is no longer a significant difference in ISR values between bornite and chalcopyrite (Figure 3 and 4), suggesting that the toxicity of bornite is related to a slower process than ROS generation upon dispersion in water. One possibility is that it takes a few hours for copper and iron released from the bornite surface to build up to concentration levels that start to impair biological functions in the cells. In fact, after 24 hours the ISR of bornite was higher at a loading of 0.001 m^2/mL than that of chalcopyrite, and the ISR of chalcocite was comparable with that of chalcopyrite (demonstrated a similar trend to bornite). If the ISR is compared for low particle loadings (0.00025 m^2/mL), that are more relevant to actual single exposure levels [170, 171], the effect of cell death is negligible. At this lower

loading the ISR generated by bornite was the greatest, followed by chalcocite and chalcopyrite (Figure 5). These results are not unexpected since at the higher loadings the ISR generated by bornite and chalcocite are predominately increased by an upregulation of ROS within the cells. The ISR derived by chalcopyrite, on the other hand, is predominately driven by cell death. While the Fenton reaction is often presented with iron as the metal, copper is also a Fenton metal [18, 172] and it may also interfere with other processes in the cell. The simultaneous release of copper and iron leads to particularly high ISR as exemplified by chalcopyrite and bornite at the highest loading level and bornite and the 0.001 m^2/mL loading level.

After the copper sulfides, galena generated the highest ISR. However, galena exhibits an immediate spike in ISR driven by a drastic loss in cell viability, followed by a recovery of the system and lower ISR values. This temporal trend, which is very different from the other sulfides studied here, may be due to a change in surface properties over time or the initial generation of $^{\cdot}OH + H_2O_2$ (Figure 1). Oxidation products of galena are relatively insoluble and due to the increase in surface coating that occurs during the dissolution, the rate of dissolution decreases with time [173]. It must be noted that anglesite, the lead sulfate dissolution product, is toxic if allowed to accumulate in the body. However, since it is a cumulative poison, the small amount of anglesite that may be present in this study would not be expected to cause damage. The ISR generated by galena can be attributed to extensive necrotic cell death. The upregulation of ROS stays predominantly stable when compared to control wells and even decreases with time. This trend in behavior is interesting, given the overall increase in viability with time (3.5% to 20%).

The ISR values generated by arsenopyrite are perhaps surprisingly low given that the mineral contains ferrous iron and generates H_2O_2 when dispersed in water (Figure 1). It is possible that the dissolution and release of iron is limited in the more complex fluids used in the cellular studies, similar to earlier results with pyrite, which showed a reduction in dissolution rate [108]. Furthermore, at a neutral pH, ferric iron-hydroxide coatings dominate the surface of arsenopyrite and sulfur, not iron, is readily released into solution [156]. Although the ISR for arsenopyrite is low and falls within the range generated by relatively inert materials (e.g. glass bead and anatase, Table 4), the cell viability data indicate that arsenopyrite does affect epithelial cells. Characteristic response of cells exposed to relatively inert material (e.g., glass beads) is to upregulate ROS and maintain a steady, if not increasing, cell viability when compared to a control [143]. However, the cell viability data for arsenopyrite indicate significant necrotic cell

death after 24 hours (Figure 2). Unlike glass beads, arsenopyrite does not upregulate ROS; hence, the resulting ISR value is low. A similar pattern is observed in a study utilizing small cell lung carcinoma (SCLC) cells, with arsenic generating predominately necrotic and not apoptotic cell death [174]. This divergent behavior is similar to that seen by galena, where the ISR is driven up primarily by cell death and not by a cellular upregulation of ROS. Unlike other metals in this study, both arsenic and lead are known immunosuppressants which might explain the limited upregulation of ROS [175, 176].

The ISR generated by the sphalerite samples are the lowest among the sulfide mineral studied here. The ISR among the sphalerite samples generally decreased with increasing iron content, which suggests that Fenton-driven chemistry with iron does not play a role. In fact, the presence of structural iron appears to limit the cytotoxicity. As reported for iron-coated quartz [159], a large amount of structural iron within the sphalerite may lead to the formation of a ferric oxide coating that may render the material less cytotoxic. The iron oxy-hydroxide patches also limit the dissolution rate. Similar to arsenopyrite, the ISR generated by all the sphalerite samples fall within the range generated by inert material[143]. However, unlike arsenopyrite, for the most part the ISR values are driven by an upregulation of ROS. Trace metals other than iron, such as mercury, may also play a role in the differentiation between the three sphalerite samples. Unlike any of the other sulfides tested here, the sample of Picos de Europa contained measurable amounts of mercury (1300 ppm). Furthermore, it is important to note that although the Balmat sphalerite did not generate a high ISR, the cell viability did decrease with time (95% versus 82%). A decrease in viability over time is not seen in inert material and indicates the inflammation generated by the Balmat sphalerite is likely to continue to increase with time.

5.5. Conclusions

The ISR is used to evaluate the toxicity of ore and/or associated ore minerals. Except in the case of chalcopyrite, there is no clear correlation between the metal-sulfides ability to generate ROS when dispersed in water and generate an ISR. The minerals containing ferrous iron and copper generated the greatest ISR values, driven by both an upregulation of ROS and necrotic cell death. Minerals containing lead, arsenic and ferric iron generated ISR values based on pronounced necrotic cell death combined with minimal ROS upregulation. The importance of evaluating the ISR and its individual components is highlighted in this study. While the actual

biological pathways interrupted are unknown, understanding the inflammatory response generated by a material and the type of cell death that results is important in determining not only the deleterious nature of the material but also a first step in a developing a better understanding of the pathogenesis and designing possibly treatments.

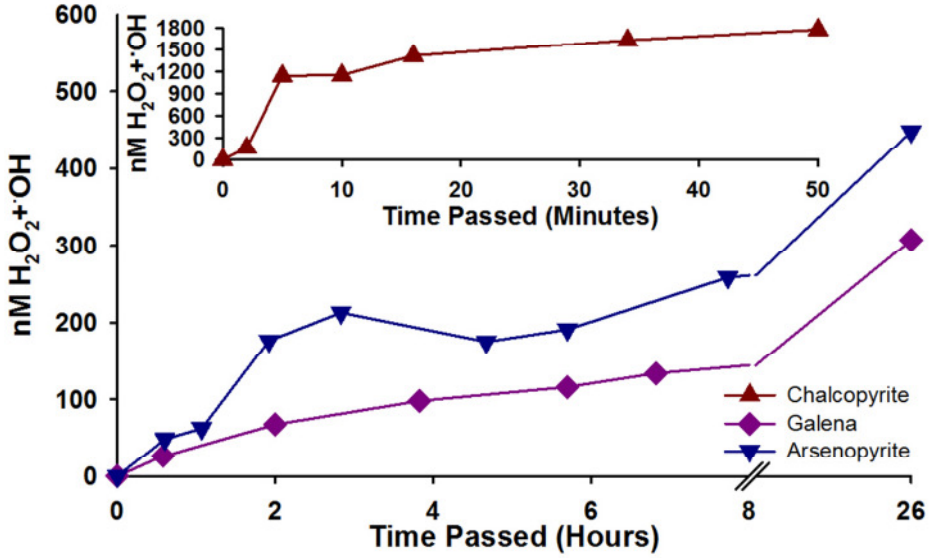

Figure 5.1. Kinetic analysis of reactive metal-sulfide ore minerals. Fluorescence measurements quantifying H_2O_2 + ·OH production in an acellular system (phosphate buffered solution at a pH of 7.4) taken as a function of time for galena, arsenopyrite and chalcopyrite are represented. Material loading was at 10 m^2/L

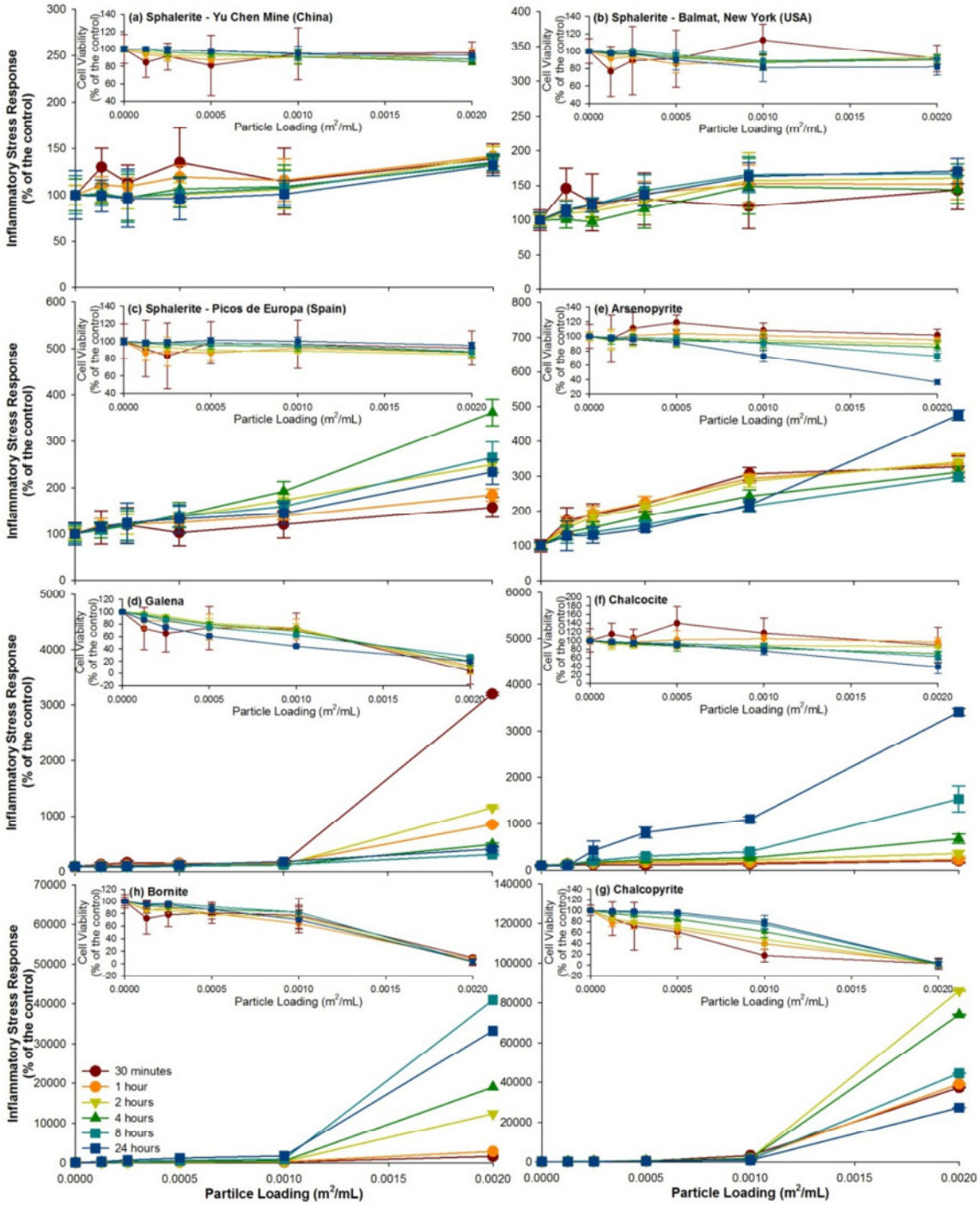

Figure 5.2. ISR of A549 cells generated by eight metal-sulfide ore minerals. The ISR generated by the eight study materials are represented, with cell viability for each in the inset. (a) Sphalerite – Yu Chen Mine (China), (b) sphalerite – Balmat, New York (USA), (c) sphalerite – Picos de Europa (Spain), (d) arsenopyrite, (e) galena, (f) chalcopyrite, (g) bornite, and (h) chalcopyrite. For some data points, the error bars (representing standard deviation of eight replicates) are obscured by the symbols.

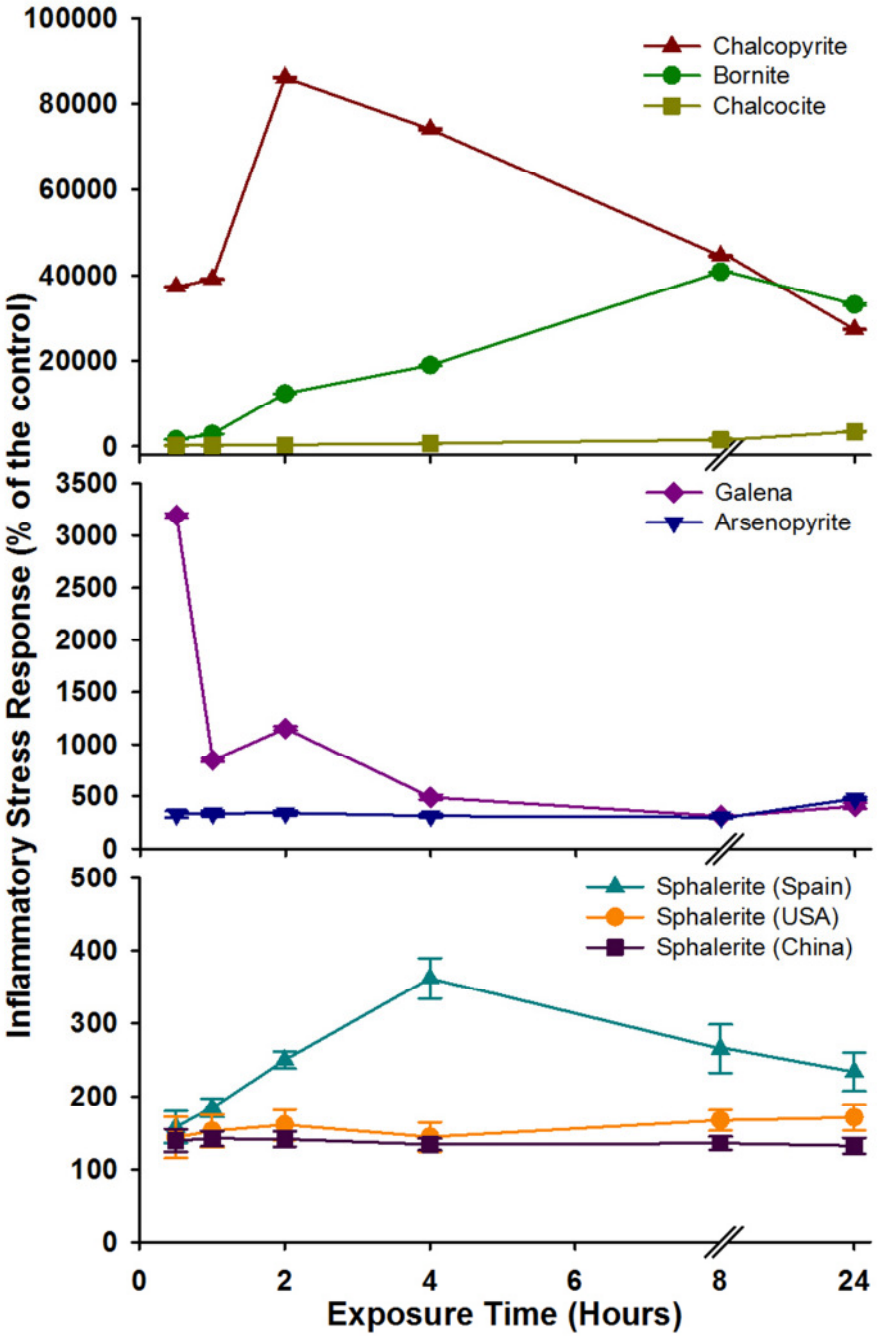

Figure 5.3. Evolution of ISR over time generated by the highest ore mineral particle loadings. The ISR generated over time by all the metal-sulfide ore minerals tested at the highest particle loading (0.002 m^2/mL) is represented. For some data points, the error bars (representing standard deviation of eight replicates) are obscured by the symbols.

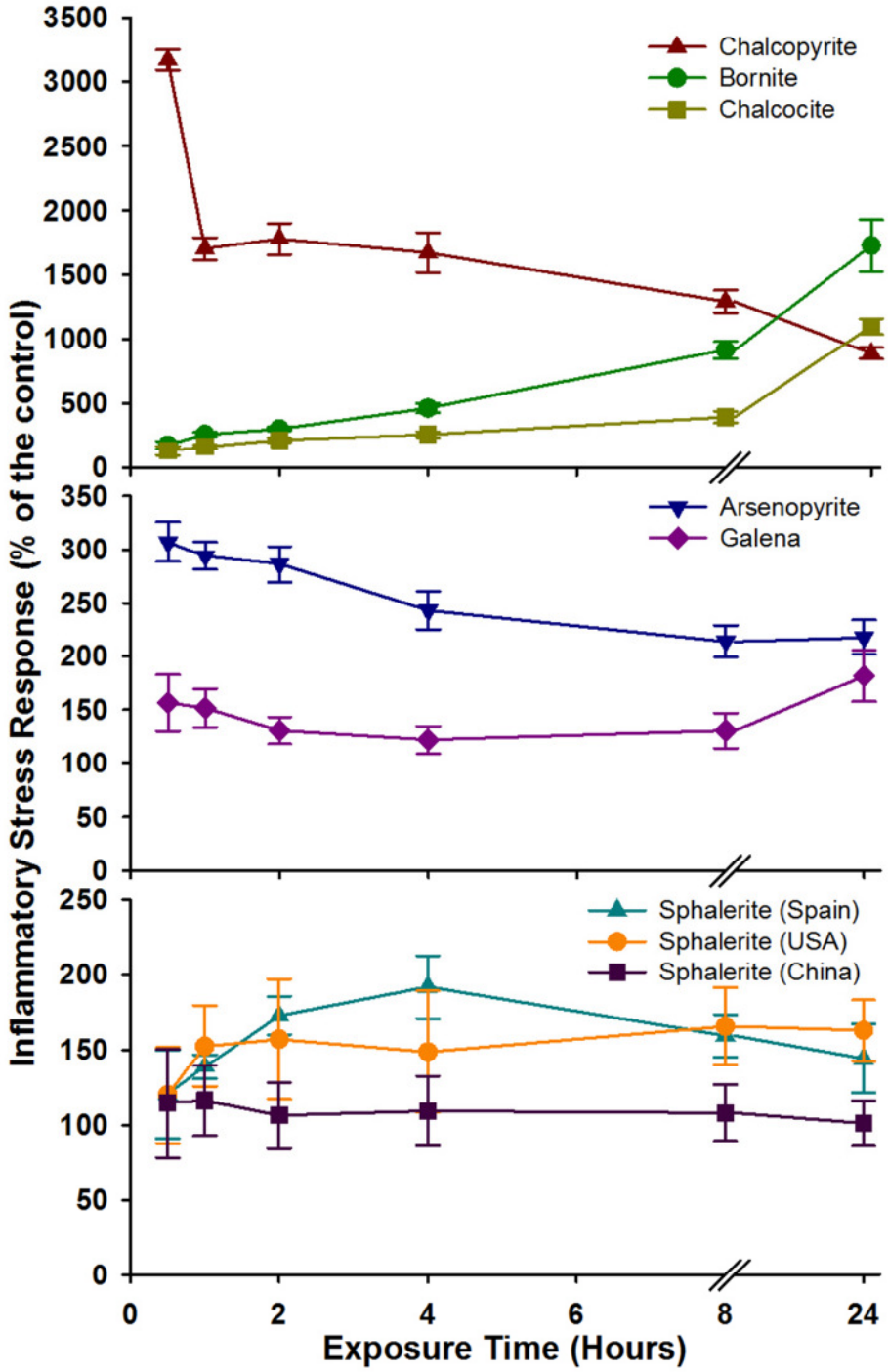

Figure 5.4. Evolution of ISR over time generated by the moderate ore mineral particle loadings. The ISR generated over time by all the metal-sulfide ore minerals tested at the moderate particle loading (0.001 m^2/mL) is represented. For some data points, the error bars (representing standard deviation of eight replicates) are obscured by the symbols.

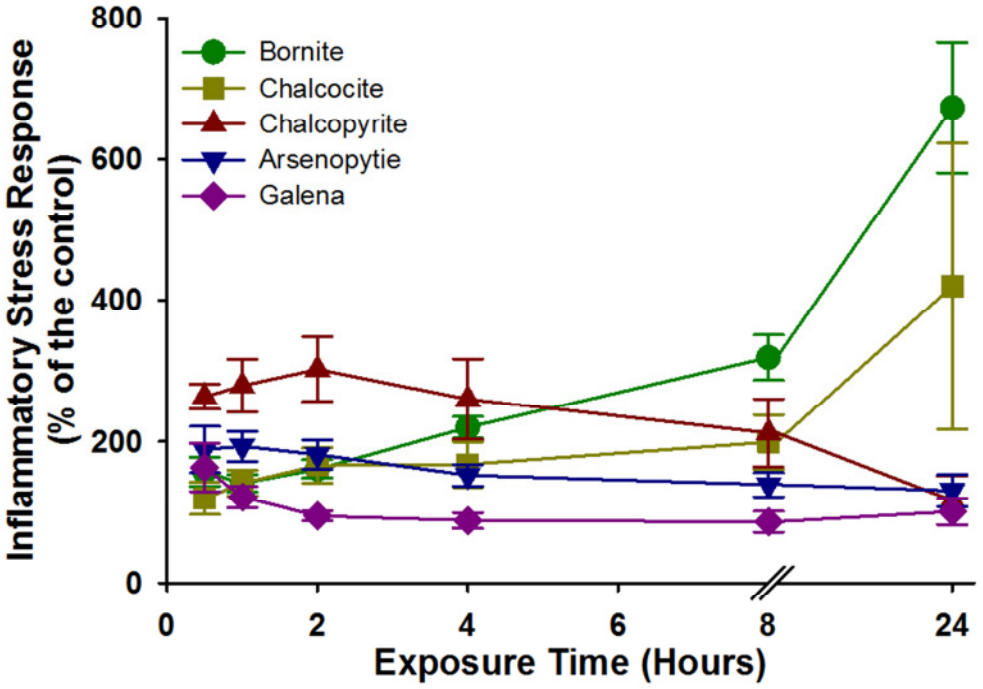

Figure 5.5. Evolution of ISR over time generated by the low ore mineral particle loadings. The ISR generated over time by selected metal-sulfide ore minerals tested at a low particle loading (0.00025 m^2/mL) is represented. For some data points, the error bars (representing standard deviation of eight replicates) are obscured by the symbols.

Chapter 6

Manganese, Fenton Chemistry and Disease: Particle Induced Inflammatory Stress Response in Lung Cells

Andrea D. Harrington[a*], Jasmeet Kaur[a], Alexander Smirnov[b], Stella E. Tsirka[c] and Martin A.A. Schoonen[a]

[a] Department of Geosciences, Stony Brook University, Stony Brook, NY 11784-2100

[b] Department of Earth and Marine Sciences, Dowling College, Oakdale, NY 11769.

[c] Pharmacological Sciences, Stony Brook University, Stony Brook, NY 11794-8651

6.1. Introduction

Historically, particle inhalation toxicity studies focus on occupational settings with high exposure levels and a clear link to a lung disease (i.e. coal workers' pneumoconiosis among coal miners, silicosis among stoneworkers, and asbestosis in mining and manufacturing) [2, 3, 177]. More recently, the scope of inhalation toxicological research has expanded to nano materials as well as to low-dose exposures outside of occupational settings in the form of inhalation of aerosols. Iron oxyhydroxides are a common component of aerosols. While there have been studies on pure iron oxides, iron oxyhydroxides have received far less attention. Furthermore, it is important to recognize that natural iron oxyhydroxides typically contain other elements. One of the major substitutes for iron in iron oxyhydroxides is manganese.

Manganese is of interest from a health perspective because it is an essential micronutrient, but excessive manganese accumulation in the body can cause irreversible neurodegenerative damage, which results in a range of neurological disorders from learning deficiencies in children to syndromes similar to idiopathic Parkinson's disease [178-182]. Most of what is known about manganese toxicity is derived from studies in occupational settings. For example, overexposure to manganese is observed in drycell battery factory workers, manganese dioxide miners, smelters, and welders [180]. At high exposures, manganese accumulates in the

brain and induces neurological diseases [183]. However, since manganese use is pervasive, non-occupation exposures are also common. The general population is exposed to manganese via fungicide, pesticide, fertilizer, electronics, aluminum cans, production of steel, gasoline additive, mine runoff, and even street drugs [180, 181, 184-187]. Apart from anthropogenic sources, manganese is the third most common metal in natural soils and dust [188]. However, little is known about the effect of manganese at low exposure dose, such as through inhalation of natural aerosol or urban dust particles. Given that manganese is a Fenton metal there is the potential that manganese-containing particles cause oxidative stress upon inhalation. The aim of this study is to study the effect of manganese-containing iron oxyhydroxide particles in comparison to dissolved manganese ions and a pure manganese oxide.

6.2. Background

Recent data indicates the amount of material accumulated in the lungs is less important than the type of particles being inhaled [121-123]. Size, aspect ratio, chemical composition and structure are factors that may contribute to the toxicity of a particle. Cellular uptake, subcellular localization, and ability to catalyze the production of reactive oxygen species (ROS) (or generate these species directly) [189] are all dependent on the latter two, lesser understood particle properties. For example, rutile (TiO_2) has been shown to generate oxidative damage, whereas anatase of the same size and chemical composition, but structurally different from rutile, does not [190]. The oxidation state of a material can also be a determinant of toxicity, as is evidenced by the relatively inert Cr(III) versus the highly toxic Cr(VI) [191, 192].

The ability of a material to take part in Fenton chemistry is important in determining its ability to generate hydroxyl radical. To date, only five metals (iron, copper, vanadium, chromium and manganese) have been shown to facilitate the Fenton reaction to varying degrees (Equations 1-4, where M represents a Fenton metal) [18, 24, 25]. The ability of Fenton metals to generate ROS is likely a key factor to their deleterious nature [7, 21, 92, 108, 143, 193]. While a cyclic process, Fenton chemistry is driven by the reduced oxidation state of the aforementioned metals [92].

$$M^{n+} + O_2 \rightarrow M^{(n+1)+} + O_2^{\cdot -} \qquad \text{Eqn. 1}$$

$$M^{n+} + O_2^{\cdot -} + 2H^+ \rightarrow M^{(n+1)+} + H_2O_2 \qquad \text{Eqn. 2}$$

$$H_2O_2 + M^{n+} \rightarrow M^{(n+1)+} + {}^{\cdot}OH + {}^{-}OH \qquad \text{Eqn. 3}$$

$$2H_2O_2 + 2M^{(n+1)+} \rightarrow 2M^{n+} + 2H_2O + 2O_2 + 2H^+ \qquad \text{Eqn. 4}$$

Normally occurring together, iron and manganese are among the most common metals in mineral dust, particularly in soil dust. Yet, there are no reports on the generation of ROS when both iron and manganese are both present. Given the abundance of iron and manganese and the fact that they are both Fenton metals, it is important to evaluate the impact of iron and manganese exposure as well as their combined exposure on human health. Here, we evaluate the effect of manganese substituted goethite, a common iron oxy-hydroxide mineral (FeOOH) on epithelial lung cells.

Since the immediate reaction of the body to manganese needs to be assessed, the protocol quantifying an inflammatory stress response (ISR) is utilized [143]. By allowing for direct comparison between study materials and the evolution of stress to be observed over a 24 hour period, the geochemical mechanics of toxicity can be better understood. Furthermore, while the interruption of specific biological pathways cannot be determined, the normalization of cellularly derived ROS (indicator of apoptosis) by cell viability (necrotic cellular death) not only allows for overall stress levels to be evaluated, but inferences can be made when each component is evaluated as well [168, 169]. By comparing the ISR with the ability of manganese to generate ROS, the mechanism behind pathogenesis can be better understood.

6.3. Materials and Methods

6.3.1. Mineral Synthesis and Sample Preparation

Dissolved metals and metal-bearing mineral phases were investigated (Table 1). The minerals were synthesized to eliminate impurities typical of naturally occurring phases and also to attain a range of manganese contents in the iron oxyhydroxide. The synthesis techniques used were based on a previously published protocol [194]. Briefly, solutions of 0.53 M $Fe(NO_3)_3 \bullet 9H_2O$ and $Mn(NO_3)_2 \bullet 4H_2O$ were mixed to specific Mn/(Mn+Fe) mole ratios (Table 1). 2 M NaOH was then added and the precipitate was centrifuged, supernatant removed and 0.3 M NaOH was added. After vortexing to re-suspend the solids, the material was dried at 60˚C for 24 hours. The samples were washed, dried and gently ground. Manganese oxides and ferrihydrite admixtures were removed via oxalate extraction [195]. The concentrations of manganese are similar to the iron/manganese ratio in Earth's upper crust [196]. The phase composition of samples (e.g., purity) was determined by X-Ray Diffractometry (XRD) using a Scintag PAD X diffractometer under the following conditions: CuKα1, 40kV, 25 mA, 5° – 75° 2Θ, step 0.02° 2Θ

and counting times of 5-10 seconds per step (Figure 1). While the goethite phases are pure, the hausmannite sample contains oxalate from the oxalate extraction performed on all the mineral samples. This is not expected to affect results. The specific surface areas were determined using a Quantachrome NOVA 5-point BET analyzer. The summary of synthesized phases used in this study is presented in Table 1.

6.3.2. Reactive Oxygen Species Formation

6.3.2.1. Adenine decomposition

Adenine was used as a proxy for hydroxyl radical formation by the manganese-doped goethite ($Fe^{III}OOH$) and hausmannite ($Mn^{II}Mn^{III}_2O_4$) [133, 197]. Adenine is stable in the presence of dilute hydrogen peroxide, but is converted to 8-oxoadenine, 2-hydroxyadenine (isoguanine), and 6-N-hydroxyaminopurine (HAP) in the presence of hydroxyl radical [197-199]. To verify that the adenine decomposition was due to hydroxyl radical formation, 4% ethanol (a radical scavenger) was added to a set of control experiments with each of the materials [197]. Two types of batch experiments were conducted. In one set, solids were suspended in 10 mL potassium phosphate buffer (10 mM) at a pH of 7.4 with 100µM Adenine. The suspensions were contained in 15 mL Falcon centrifuge tubes. The tubes were wrapped in Al-foil to avoid possible photochemical reactions. The mineral slurries were incubated for at least 19 days on orbital shakers with periodic sampling. In order to assess adenine decomposition, the tubes were centrifuged at 2,000 rpm for 25 minutes, 2 mL of the supernatant removed and placed in a 1 cm quartz cuvette for UV analysis. After analysis, the supernatant was placed back in the foil covered tube, vortexed to suspend the material, and placed back on an orbital shaker. To directly test whether the manganese-doped goethite ($Fe^{III}OOH$) and hausmannite ($Mn^{II}Mn^{III}_2O_4$) can facilitate the Fenton reaction, as second set of experiments were performed with 1 mM H_2O_2 added to the mineral suspension in the same buffer solution. Adenine degradation was quantified by absorbance at 260 nm using a Hach DR/4000 UV-Vis spectrometer. All reagents were procured from Sigma-Aldrich and used without further purification. Particle-free control experiments were performed to determine the stability of adenine at a pH of 7.4. All solutions were prepared form 18.2 MΩ-cm, UV-irradiated, ultra-pure water.

6.3.2.2. APF

The 3'-(p-Aminophenyl) fluorescein (APF) probe was also utilized to quantify the formation of not only hydroxyl radical, but also hydrogen peroxide by the manganese species in water. While the APF probe is highly specific for hydroxyl radical, the addition of horseradish peroxidase (HRP) converts the probe to the fluorescent fluorescein in the presence of hydrogen peroxide. This allows for both hydroxyl radical and hydroxyl radical plus hydrogen peroxide to be quantified. Originally developed by Setsukinai et al. [200], the protocol used in the present study was adapted and is outlined by Cohn et al. [57]. These experiments complement the experiments performed with adenine.

6.3.3. Culturing and Plating the A549 Human Lung Epithelial Cell Line

A previously published protocol was employed in the culturing and plating of the A549 human lung epithelial cell line [143]. The cell growth media was comprised of 10% Fetal Bovine Serum (FBS) and 1% 1X Penicillin/Streptomycin in Ham's F12K Media. The cells were detached using trypsin with ethylenediaminetetraactic acid (EDTA) in cases of passage and counting. Cells were quantified using a hemocytometer and trypan blue staining agent and then loaded into 96-well microplates at 8 x 10^4 cells/mL. Columns 1, 2, 11, and 12 were kept cell free for normalization purposes. Cell work was performed in a sterile hood and when not in the hood, a lid was kept on the microplate. An incubator kept the temperature, relative humidity and carbon dioxide concentration in air constant (37˚C, 95% and 5% CO_2 in air, respectively).

6.3.4. Inflammatory Stress Response Measurements

A previously published protocol was utilized for *in vitro* inflammatory measurements on the A549 human lung epithelial cell line [143]. Two different assays were used in tandem and administered *in situ*: 2',7'-dichlorfluorescein-diacetate (DCFH-DA) assay, which is a probe for cellularly generated ROS [119] and the cell viability assay 3-(4,5-dimethylthiazol-2-yl)-5-(3-carboxymethoxyphenyl)-2-(4-sulfophenyl)-2H-tetrazolium (MTS). When analyzed concomitantly, the ROS upregulation can be normalized to cell viability, allowing for the contaminant derived inflammatory stress response (ISR) to be determined.

The salts and minerals were administered at different loadings, generated via serial dilutions. Loadings for mineral samples were normalized by weight (given similar surface areas),

while solution salts were normalized by molarity. ROS upregulation measurements were made using Thermo Scientific's Fluoroskan Ascent and cell viability measurements were made on a Molecular Devices' SpectraMax 340PC384 since DCFH-DA is a fluorometric assay and MTS is colorimetric probe.

6.4. Results

The ISR generated by iron and manganese in solution, manganese-substituted goethite, and hausmannite is presented in Figures 2-5. The solutions containing moderate (1 mM) concentrations of iron and manganese generated a similar ISR after 24 hours (1641 and 1605 % of the control, respectively) (Figure 2). Manganese generated a steadier rate of ISR increase, whereas there was a significant increase in ISR after 30 minutes followed by a steady increase in ISR value for the experiment with dissolved iron (Figure 3). At the highest concentration (2 mM) the experiment with dissolved manganese generated a greater ISR value than the experiment with dissolved iron. Similar to moderate concentrations, the ISR generated in the experiment with dissolved manganese steadily increased with time while there was an immediate spike in the ISR value for the experiment with iron followed by a slow increase. However, unlike the ISR generated in the experiment with 1 mM iron, the ISR generated in the experiment with 2 mM iron peaked at the 8 hour time point and then decreased after 24 hours. Generally, the ISR generated by dissolved manganese was due to an upregulation in cellular ROS, whereas the ISR generated by dissolved iron was due to a dramatic decrease in cell viability. For the solutions in which manganese and iron were mixed, the ISR exhibited trends that were similar to those of the iron solution.

For the goethite, manganese-substituted goethite and hausmannite, the ISR increased with increasing manganese content (Figure 4). While low, the ISR generated in experiments with G1 (pure goethite) and G2 (5% manganese substituted goethite) increased with time and reached 141 and 183% of the control, respectively (Figure 5). The ISR generated in experiments with G3 (10% manganese substituted goethite) was highest at the 8 hour time point (592 % of the control) and decreased to 505 % of the control at 24 hours. Cells exposed to G4 and G5 exhibited the same pattern of behavior with the highest ISR generated occurring at the 4 hour time points (3320 and 8795 % of the control, respectively). After this peak value, the ISR generated by both samples gradually decreased at the 8 and 24 hour time points. The results of experiments with

G4 and G5 differ from those with samples G1through G3 in that lower cell viabilities contributed to the increasing ISR, while in experiments with G1 through G3 the ISR value were solely attributable to an upregulation in cellularly derived ROS. Specifically, the viability of cells exposed to G4 dropped from 94.3 % viability compared to the control at the 1 hour time point, to 85.2 % at 4 hours, followed by 72.1% viability after 24 hours. G5 (hausmannite) generated more extensive cell death, as viability immediately dropped to 66.4 % after 30 minutes and then reached 48.6 % of the control at 1 hour. The cell viability slowly increased with time to 59.8 % at 24 hours.

The ability of goethite, manganese-doped goethite and hausmannite to generate hydroxyl radicals was also determined via adenine decomposition and APF. Not only was there no fluorescein generated in the APF experiments, there was also no appreciable decay of adenine for experiments performed in phosphate buffer alone or those spiked with hydrogen peroxide for G1-G3 (Figure 6). While there was appreciable fluorescein generation by hausmannite (4 μM after 8 days) and G4 (932 nM after 8 days) in the APF experiments, it is not clear if this fluorescence was due to ROS generation or a false positive due to an interaction between manganese and the APF probe [201]. Adenine showed a slight decrease in concentration in experiments with G4 and G5; however, the decrease in concentration was similar to those observed in experiments with ethanol. Furthermore, in batch experiments in which hydrogen peroxide was added there was no appreciable loss of adenine. Taken together the results of the APF experiments and the adenine experiments suggest that the solids tested here do not produce significant amounts of hydroxyl radical when dispersed in phosphate saline solutions.

6.5. Discussion

The ISR, a measure of the inflammatory nature of a material, is derived by normalizing the cellular ROS upregulation by A549 human lung epithelial cells to the viability of the cells. This study demonstrates the importance of assessing ROS upregulation and measuring cell viability in parallel. While the ISR generated by manganese in solution is predominately driven by the upregulate ROS production in cells; dissolved iron, on the other hand, does not lead to significant ROS upregulation, yet results in extensive necrotic cell death. The different cellular reactions to the metal salts suggest different biological responses to the two Fenton metals. Furthermore, the effect of mineral structure is demonstrated when the reaction of the cells to iron

salt is compared to the reaction of the cells to pyrite (FeS_2) [143]. In the study by Harrington et al. [143], the ISR is 50 times greater than the highest ISR generated by iron salt and originated from significant ROS upregulation and dramatic cellular death.

Unlike with the iron salt solution, the manganese solution generated an increase in ISR with not only time but also loading. It is likely that this is related to a difference in stability of dissolved manganese compared to dissolved iron rather than a difference in reactivity between the two metals. Since the redox environment in biological systems ranges from -50 to -300 mV at a pH of 7.4, Mn^{II} will stay in solution, while iron hydroxide will precipitate out [202]. The precipitation of iron hydroxide is observed at the higher loadings and also increases with time. Therefore, while the Mn^{II} in solution continues to generate oxidative stress, the stable, relatively inert, iron precipitate does not. However, in the body, if engulfed by macrophages, the 4.5 pH of the lysosomal fluid would likely favor the more reduced, Fe^{II}. The experiments in which the cells were exposed to mixtures of iron and manganese salts tended to give ISR values similar to those with iron salts alone. This result is likely due to precipitation of iron hydroxide and co-precipitation of manganese, leading to the removal of manganese and iron from solution.

The results with pure goethite corroborate earlier work that showed that this iron oxyhydroxide does not illicit an inflammatory response in human lung cells. Because goethite is essentially inert, it is a useful material to study the effect of trivalent manganese on epithelial cells. While intuitively Mn^{II} might be considered a stronger reductant than Mn^{III}, trivalent manganese species are more toxic than Mn^{II} because they tend to directly oxidize biological molecules [180, 203]. While there is not a significant ISR at 5% manganese content (G2), once doped with 10% (G3) and 15% manganese (G4), the ISR generated by the goethite increased steadily and linearly with loading. However, unlike with the manganese salt solution, but similar to other reactive minerals, the ISR generated did not increase with time [143]. Similar to the manganese salt solution, the ISR generated by manganese doped goethite is predominately driven by an upregulation of ROS. Hausmannite (G5), the only pure manganese oxide studied, not only generated the greatest ISR, it also generated both an upregulation of ROS and significant necrotic cell death. The extensive necrotic cell is likely due to cellular derived ROS generation, resulting in sever oxidative damage [204]. Although the pure phase manganese mineral generated significantly higher ISR values than manganese-doped goethite, when normalized on a manganese basis, the toxicity of all the manganese bearing minerals are similar.

The extremely slow oxidation rate of divalent manganese in solution helps explain the lack of substantial hydroxyl radical formation [205]. Given that the reaction rate of manganese increases at non-biologically applicable pH ranges [205] and that there was no quantifiable ROS generated by the manganese-doped goethite or hausmannite, it is likely that the oxidative stress caused by manganese exposure is not driven by its ability to directly generate ROS in solution (at least on the time scale of the present study) but rather due to its direct interaction with biomolecules [203]. Therefore, although they are both Fenton metals, the mode of oxidative stress for manganese and iron differs. This difference is observed in the causes underlying the high ISR values for experiments performed with iron and manganese salts. While the vast necrotic cellular death observed with Fe^{II} in solution is likely attributable to its known ROS generating potential [57, 92], the upregulation of cellular ROS caused by the manganese originates elsewhere. Even though the mechanisms behind manganese trafficking and oxidative stress are beginning to be understood in neurodegenerative diseases [206], further experiments need to be performed to determine if the specific biological pathway interrupted by manganese in the lungs are the same.

6.6. Conclusions

Breaking down natural soils into individual components can provide a deeper insight into the origin of oxidative damage and therefore disease. The extreme reactivity of Fe^{II} generates an immediate cellular response of necrotic cellular death which drives up the ISR at relatively low concentrations. The higher solubility of manganese compared to iron, which precipitates out into a relatively inert iron hydroxide phase under these biologically applicable conditions, allows for a considerably steady ISR over time and a response that increases smoothly with loading. The ISR generated by goethite increased with manganese content. The only pure manganese solid phase studied, hausmannite, generated the greatest ISR and is the only manganese species that generated significant cellular death. The insignificant hydroxyl radical formation by manganese doped goethite and hausmannite indicates that the oxidative damage is likely derived by direct interaction with biomolecules rather than its ability to generate ROS in solution. However, given the low proportion of manganese in goethite that generated an ISR, it is important to keep in mind trace components in minerals when discussing and assessing toxicity.

Table 6.1. Metal salts and minerals investigated.

Group	Experimental Designation	Metal Form	Maximum Concentration	
			Iron	Manganese
Metal Salts	Fe Salt	Iron sulfate heptahydrate	2 mM	---
	Mn Salt	Manganese sulfate monohydrate	---	2 mM
	FeMn Salt	Iron and Manganese sulfate	1 mM	1 mM
Mineral Species	G1	Goethite	$Fe(III)OOH$	
	G2	Manganese Substituted Goethite	$Fe(III)_{0.95}Mn(III)_{0.05}OOH$*	
	G3		$Fe(III)_{0.9}Mn(III)_{0.1}OOH$*	
	G4		$Fe(III)_{0.85}Mn(III)_{0.15}OOH$*	
	G5	Hausmannite	$Mn(II)Mn(III)_2O_4$*	

*Idealized stoichiometry

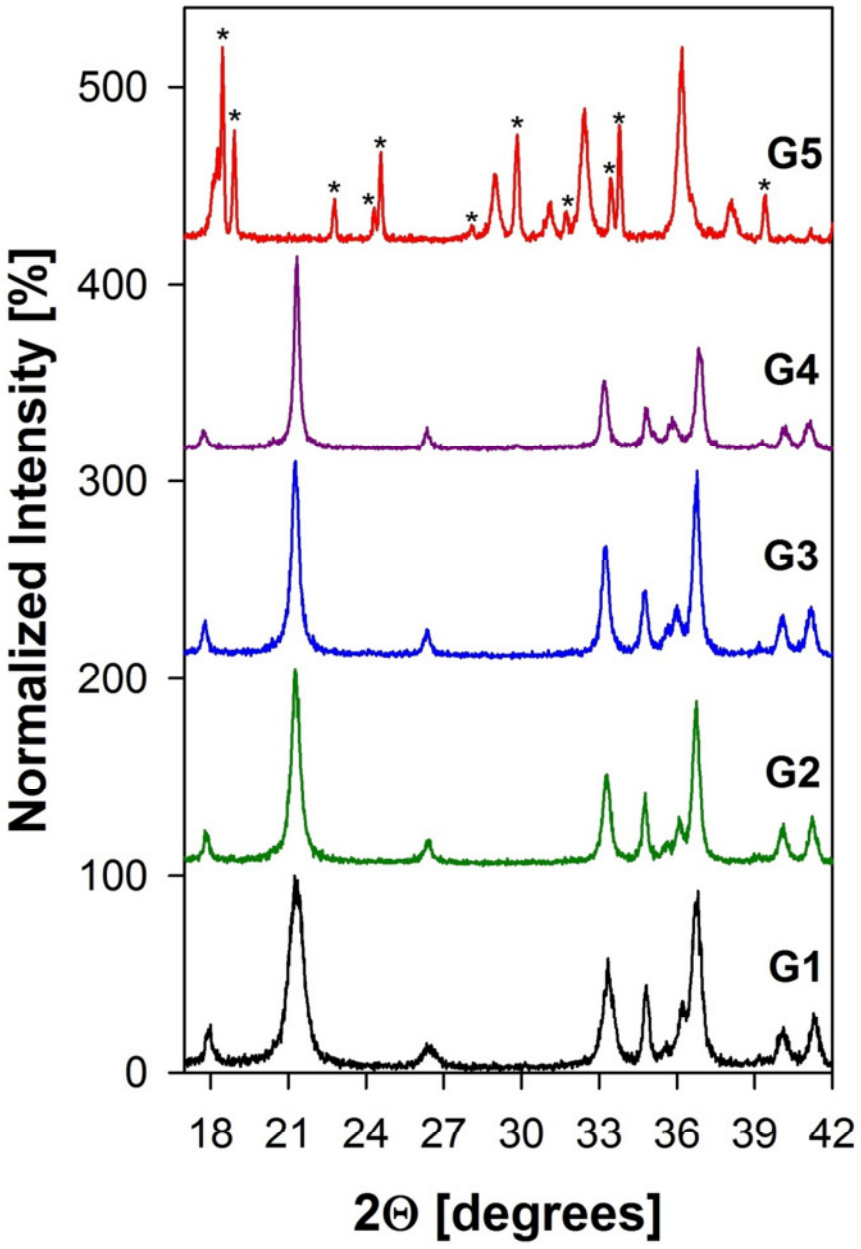

Figure 6.1. XRD data of iron and manganese oxide minerals. XRD data of manganese, iron phases investigated in this study. Normalized intensity is offset for clarity along the y-axis. Phases G1 through G4 correspond to pure goethite with increasing manganese content in the structure (0%, 5%, 10% and 15% Mn for G1 through G4, respectively). The structural changes resulted from the increasing Mn content can be documented by the decreasing FWHM of the peaks located around 21.3 and 26.4˚ 2Q, as well as increased separation of the peak dublet between 36 and 37 degrees 2theta from 0.53 degrees in sample G1 (36.25 and 36.78˚ 2Q) to 1.04˚ in sample G4 (35.84 and 36.88˚ 2Q). Sample G5 is a mixture of hausmannite and a manganese oxalate artifact from the synthesis procedure. Oxalate peaks are marked with an asterisk.

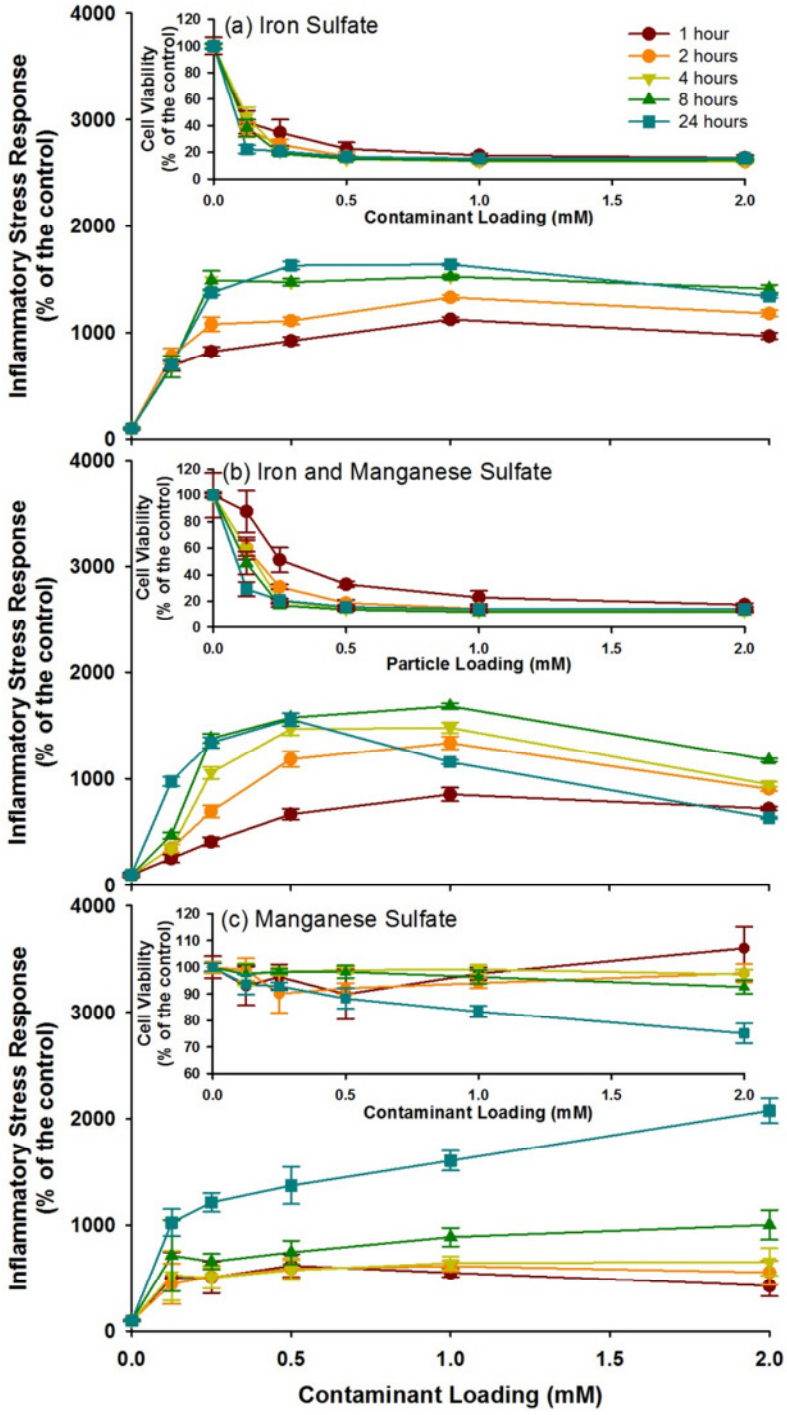

Figure 6.2. ISR of A549 cells generated by metal salt solutions. The ISR generated by the three metal salt solutions are represented, with cell viability for each in the inset. (a) Iron sulfate, (b) iron and manganese sulfate, and (c) manganese sulfate. For some data points, the error bars (representing standard deviation of eight replicates) are obscured by the symbols.

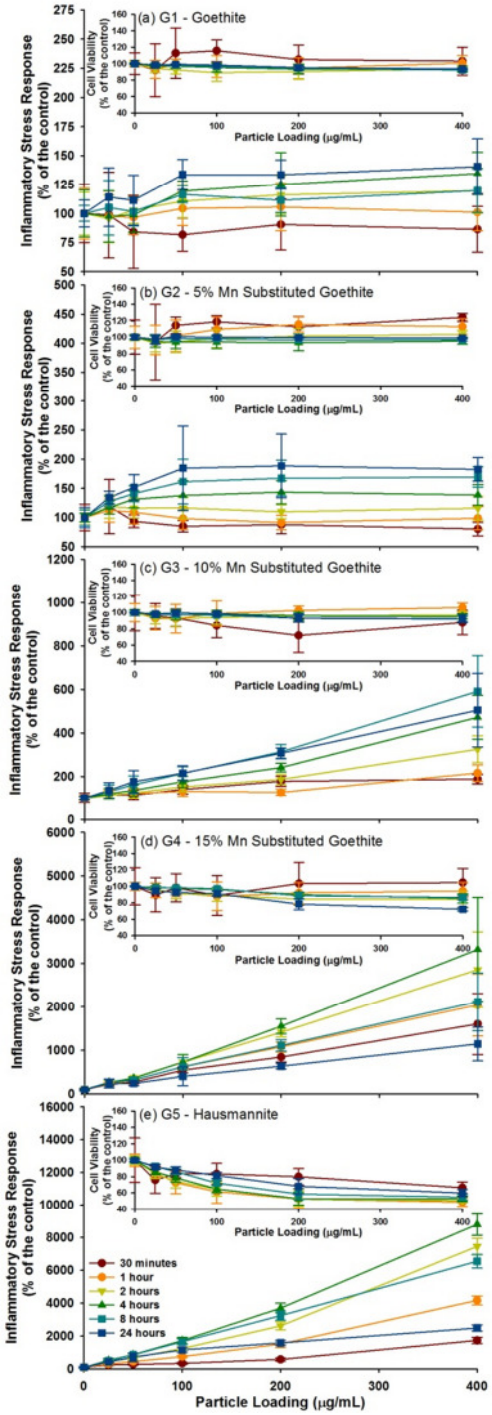

Figure 6.3. ISR of A549 cells generated by synthetic iron and manganese oxide minerals. The ISR generated by the five synthetic iron and manganese oxide mineral species are represented, with cell viability for each in the inset. (a) G1 – goethite, (b) G2 – 5% manganese in goethite, (c) G3 – 10% manganese in goethite, (d) G4 – 15% manganese in goethite, and (e) G5 – hausmannite. For some data points, the error bars (representing standard deviation of eight replicates) are obscured by the symbols.

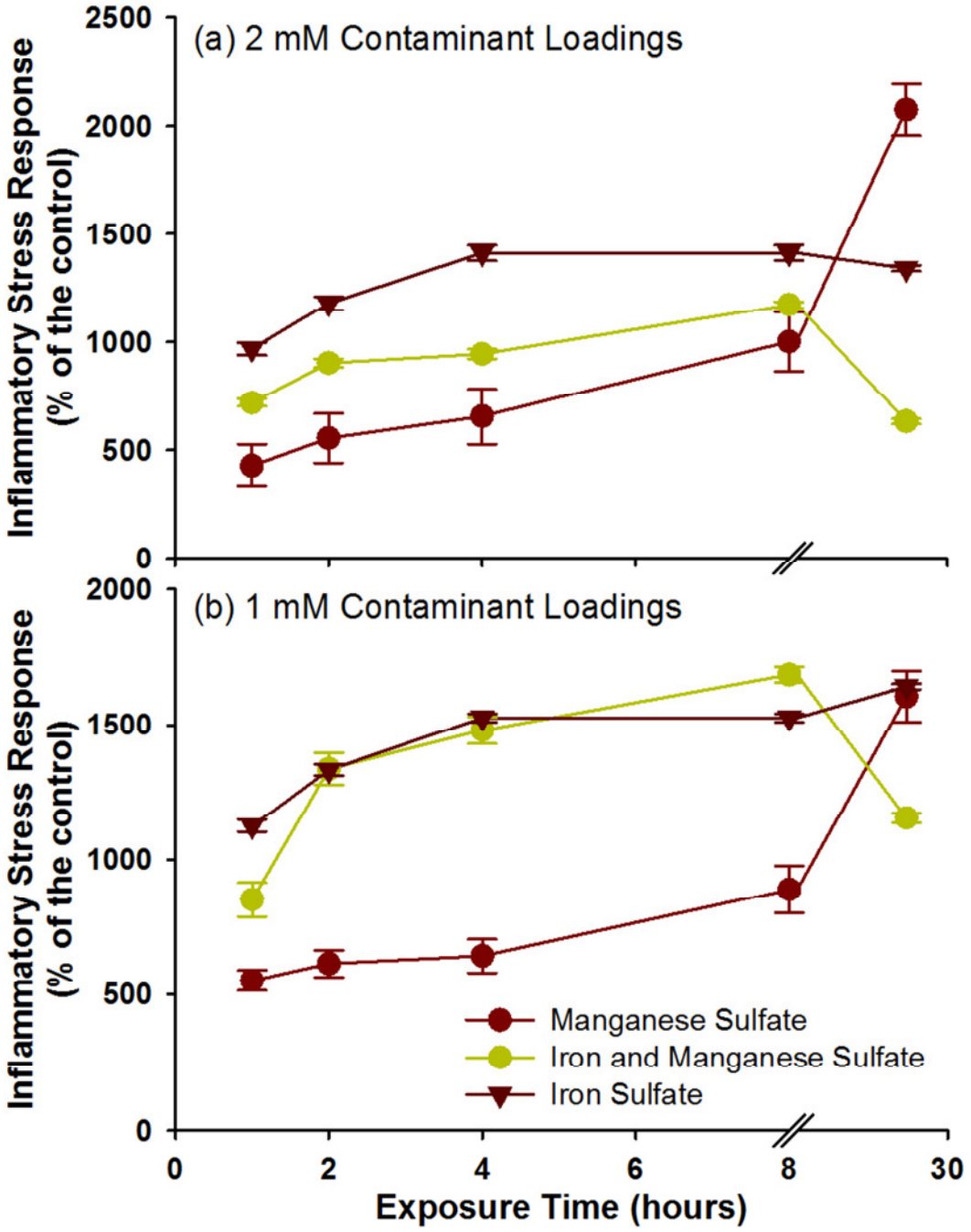

Figure 6.4. Evolution of ISR over time generated by metal salt solutions. The ISR generated over time by the metal salt solutions at two contaminant concentrations are represented. (a) 2 mM and (b) 1 mM concentrations of iron sulfate, iron and manganese sulfate, and manganese sulfate. For some data points, the error bars (representing standard deviation of eight replicates) are obscured by the symbols.

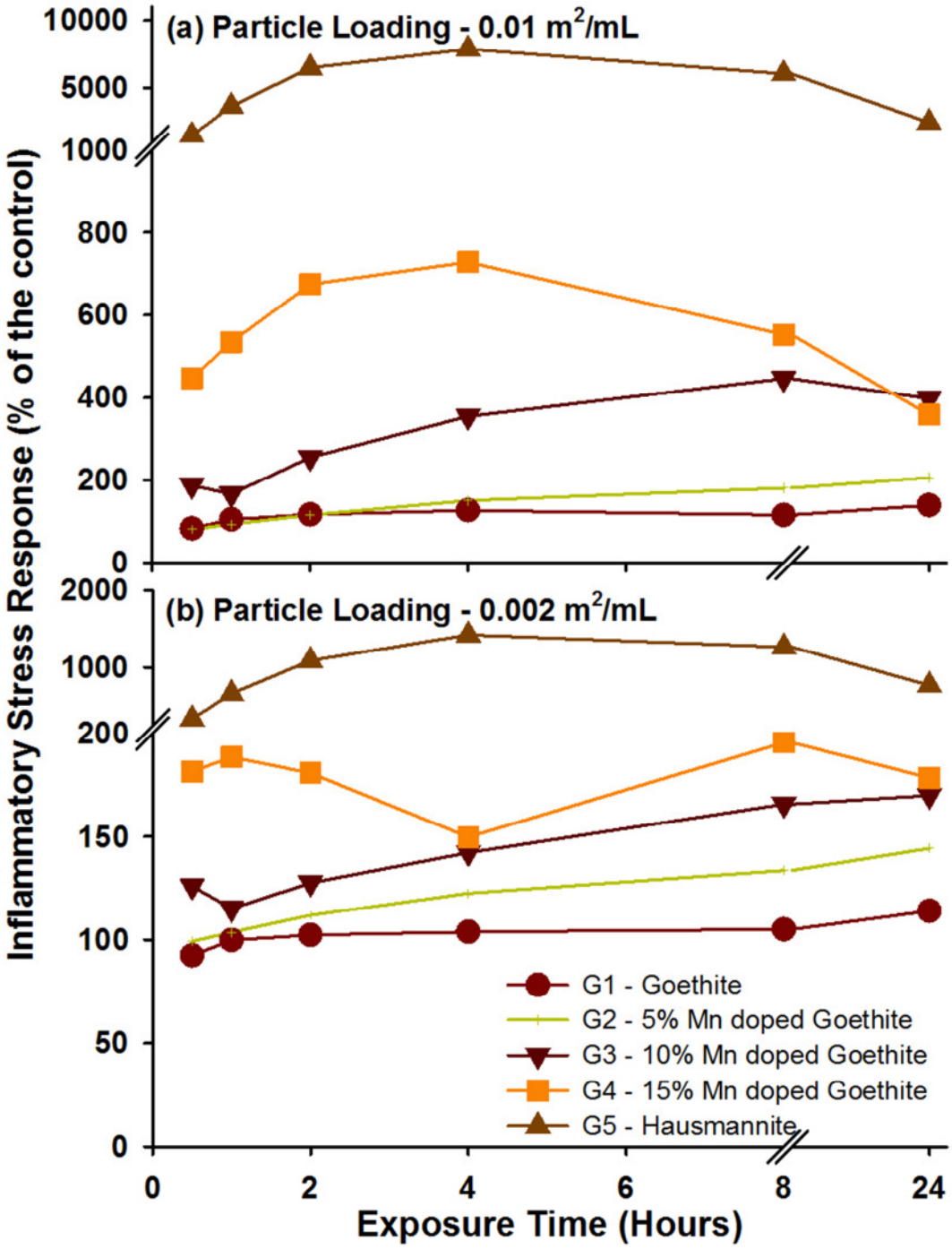

Figure 6.5. Evolution of ISR over time generated by synthetic iron and manganese oxide minerals. The ISR generated over time by the five synthetic iron and manganese oxide mineral species at two contaminant concentrations. (a) 0.01 m^2/mL and (b) 0.002 m^2/mL concentrations of goethite, 5% manganese in goethite, 10% manganese in goethite, 15% manganese in goethite, and hausmannite. For some data points, the error bars (representing standard deviation of eight replicates) are obscured by the symbols.

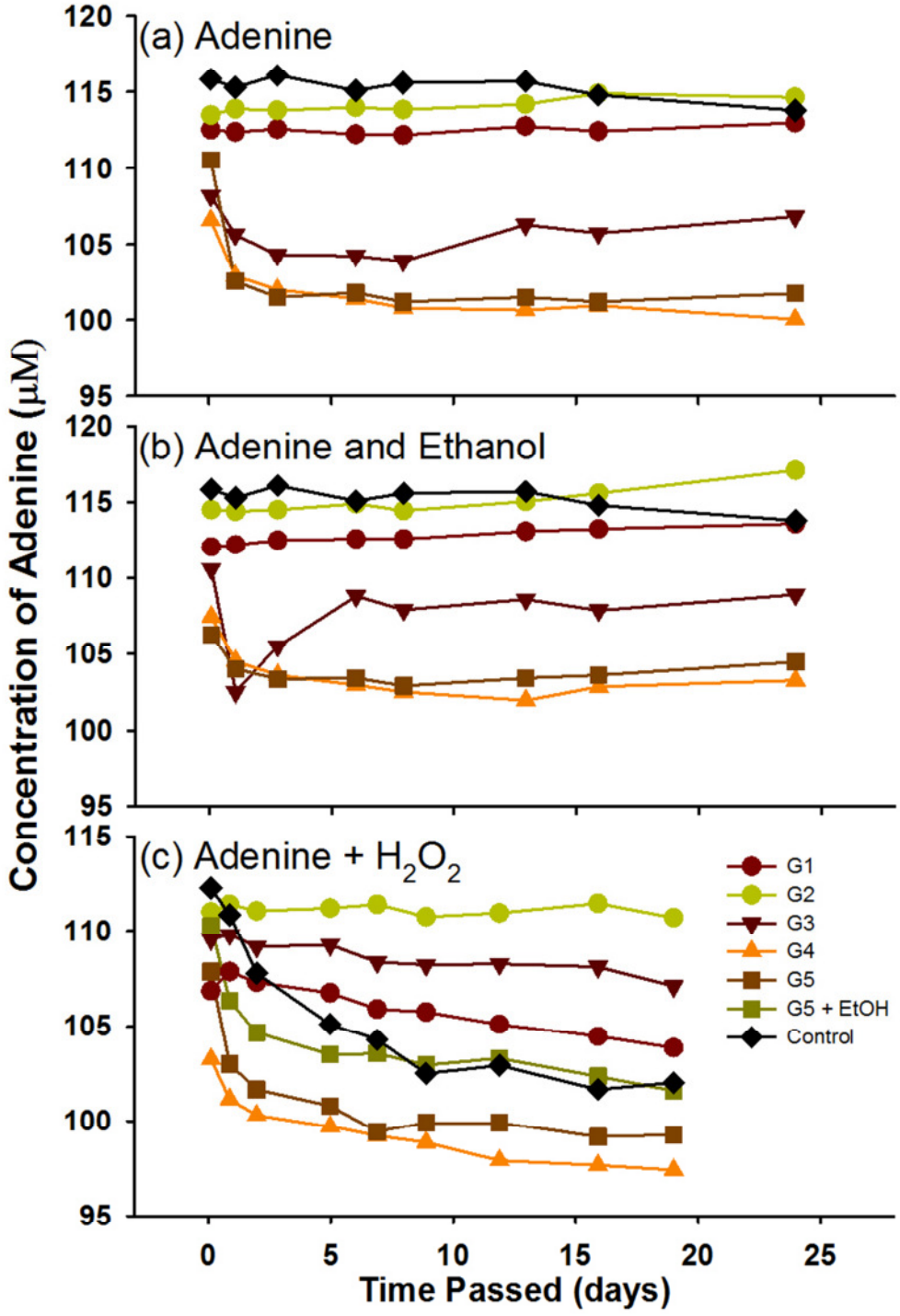

Figure 6.6. Degradation of adenine by synthetic iron and manganese oxide minerals. The degradation of adenine (absorbance at 260 nm) by synthetic iron and manganese oxide minerals is used as a proxy for hydroxyl radical formation are represented. (a) adenine, (b) adenine and ethanol and (c) adenine and hydrogen peroxide.

Chapter 7

The role of Iraqi dust in inducing lung injury in United States soldiers: Initial findings of an *in vitro* study

Andrea D. Harrington[1], Millicent P. Schmidt[1], Anthony M. Szema[2,3], Stella E. Tsirka[4], and Martin A.A. Schoonen[1]

[1] Department of Geosciences, Stony Brook University, Stony Brook, NY 11794-2100

[2] Stony Brook University School of Medicine, Stony Brook, NY 11794

[3] Veterans Affairs Medical Center, Northport, NY 11768

[4] Pharmacological Sciences, Stony Brook University, Stony Brook, NY 11794-8651

7.1. Introduction

The last United States combat troops were withdrawn from Iraq by 2012. However, many soldiers are experiencing lingering health effects associated with their deployment to Iraq. Apart from combat-related injuries, a significant number of soldiers returning from the Greater Middle East have lung illnesses ranging from new onset asthma to constrictive bronchiolitis. The rate of asthma development among soldiers is higher for troops that have been deployed in Iraq than those remaining stateside (6.6% vs. 4.3%, respectively) [16, 207]. In fact, 14% of medic visits in Iraq were due to respiratory complaints [208]. The lung illnesses observed are inflammatory in nature and, therefore, more indicative of an overabundance of reactive oxygen species (ROS) within lungs rather than a disruption in cellular replication (mutagenicity) [209].

The conditions in the Greater Middle East are dramatically different from the usual conditions that soldiers are exposed to in the United States. Average rainfall in Iraq is low (216 mm per annum versus 715 mm per annum for Iraq and United States, respectively), leading to dry soil and dust-filled air [210, 211] . Specifically, the average PM_{10} and $PM_{2.5}$ mass in the Greater Middle East is an order of magnitude higher than in the southwest United States [212]. Recurrent dust storms can place as much as 10,000 $\mu g/m^3$ of PM_{10} in the air, which is 154 times

higher than the exposure standard for soldiers [212, 213]. Inhalation of PM_{10} particulate dust can trigger asthma, even in the absence of allergic sensitization [214]. Possible exposure sources are natural mineral dust (soil and sand), as well as dust originating from burn pits located within camps. These burn pits were used to incinerate organic and inorganic waste, including spent ammunition and jet fuel.

In general, a material can generate inflammation within the body in a number of ways. One common pathway to inflammation is particle-induced formation of ROS via reactions with surface defects and/or particle-mediated Fenton chemistry [92]. In Fenton chemistry, dissolved molecular oxygen is reduced step-wise by dissolved ferrous iron, leading to the formation of superoxide, hydrogen peroxide, and hydroxyl radical. In particle-mediated Fenton chemistry the reduction of dissolved molecular oxygen can take place at iron atoms exposed on particle surfaces or in solution with iron released by the particle. It is now widely recognized that metals other than iron, such as chromium, manganese, vanadium, and copper, can also facilitate Fenton chemistry. Apart from directly increasing the ROS level in cells, particle-derived metals may also affect the homeostasis between pro- and anti-oxidants within cells by reacting with anti-oxidants, thereby tipping the balance in favor of pro-oxidants.

A second pathway to particle-induced inflammation is driven by the mere exposure to particulate matter, regardless of its reactivity. Particle exposures leading to a lung burden in excess of 1µg/L impairs alveolar macrophage (AM)-mediated lung clearance. This condition, called particle overload, leads to a decrease or even cessation of the phagocytosis of particles. This particle-induced suppression of phagocytosis can also diminish the ability to clear dead or dying cells from the lung through phagocytosis, a process referred to as efferocytosis. A lack of efficient efferocytosis exacerbates the inflammation by generating secondary necrotic cellular death. If the particulate material is cytotoxic, phagocytosis may be compromised at exposure levels below the threshold triggering impairment when exposed to unreactive material. [42]

In this study we evaluate the response of epithelial lung cells to a dust sample collected in Iraq. Cell viability and ROS up-regulation have been measured to determine whether this material elicits an unusually strong ISR compared to soil dust collected at an arid location in the United States and standard reference soils.

7.2. Materials and Methods

7.2.1. Dust sample acquisition, characterization and treatment

Two natural dust samples were investigated. The primary dust sample came from Camp Victory, Iraq (CVD) and was collected near a burn pit. For comparison, a second dust sample was collected from Fort Irwin, California, (FID). Fort Irwin is located in the Mojave Desert, midway between Las Vegas, Nevada, and Los Angeles, California. Silica glass beads from Corpuscular and two National Institute of Standards and Technology (NIST) soils (San Joaquin #2709 and Montana #2710) were evaluated along with the two dust samples. The San Joaquin soil contains baseline trace elements whereas the Montana sample contains elevated trace elements. Full descriptions of the two soil reference materials is provided by NIST [136, 137].

Both CVD and FID dust samples were fully characterized. Morphology was examined using the LEO Gemini 1550 (Figure 1). The mineralogy of each dust samples was determined using a Scintag PAD X diffractometer under the following conditions: CuKα1, 40kV, 25 mA, 5° – 75° 2Θ, step 0.02° 2Θ and counting times of 5-10 seconds per step. Complete chemical analyses were performed using XRF at the Geoanalytical Laboratory at Washington State University. The XRF analysis is based on a lithium borate fused glass bead of the sample. In order to determine the origin of toxicity within the dust, carbonate phases were dissolved by exposing a subsample of each dust to a 1.0M HCl solution for about 12 hours. The acid-treated material was reanalyzed in house with a Bruker S4Pioneer XRF using the pressed pellet method. For normalization of exposure experiments, the surface area was determined using a Quantachrome NOVA 5-point BET analyzer using UHP N_2 gas.

7.2.2. Particle-derived reactive oxygen species formation

The formation of hydroxyl radical (˙OH) and hydroxyl radical plus hydrogen peroxide (˙OH+H_2O_2) was determined upon dispersal of the dust in water. The analysis for ˙OH and ˙OH+H_2O_2 was conducted using a protocol developed by Cohn et al. [57] which is based on the reaction of 3' -(p-Aminophenyl) fluorescein (APF) with ˙OH forming fluorescein [200]. The APF probe has a very high specificity for ˙OH. By adding horse radish peroxidase (HRP) any H_2O_2 with be converted and leads also to the formation of fluorescein. Hence, by adding HRP the concentration of ˙OH+H_2O_2 is determined. Following the protocol outlined in Cohn et al. (2009) we measured both the production of ˙OH and ˙OH+H_2O_2 after 24 hours of incubation.

7.2.3. Culturing and Plating the A549 Human Lung Epithelial Cell Line

The A549 human lung epithelial cell line was utilized. The cells were cultured and plated using a previous published protocol [143]. The cell growth media consisted of predominately Ham's F12K Media with 10% fetal bovine serum and 1% 1X penicillin/streptomycin. Trypsin with ethylenediaminetetraacetic acid (EDTA) was used to detach the cells for passage and plating. Cell quantification was determined with Trypan blue stain on a hemocytometer.

To maximize replicates and experimental conditions, 96-well microplates were utilized. When plating, columns 3 through 10 were loaded with 8 x 10^4 cells/mL, covered with a microplate lid, and allowed to incubate at 37˚C in culturing media until confluent (approximately two days). Columns 1, 2, 11, and 12 were kept cell free for normalization. In order to avoid airborne bacteria, sterile hoods were always employed when working with the cells and microplate lids were utilized when not in the hood. Temperature, relative humidity and carbon dioxide (CO_2) concentration in air were kept constant (37˚C, 95% and 5% CO_2 in air, respectively) in the incubator.

7.2.4. Inflammatory stress response measurements

A previously published protocol was used to determine the inflammatory stress response generated by particle contaminates [143]. Cell growth media was discarded upon experimental initiation and columns 1-6 were filled with 200 µL 50 µM 2',7'-dichlorofluoroscein-diacetate (DCFH-DA) from Sigma Aldrich in Hank's Buffered Salt Solution (HBSS) and columns 7-12 were filled with 200 µL HBSS, and then placed in the incubator for 20 minutes. All liquid contents were again discarded and 200 µL of the contaminant slurry was added to selected wells. The range in dust particle loadings was derived from serial dilutions of two stock solutions. Initial experiments were performed using a stock solution of 0.002 m^2/mL and follow up experiments were performed using a stock solution of 0.05 m^2/mL. A row of wells were kept contaminant free for normalization (control). After the addition of the contaminant slurry, 20 µL of 3-(4,5-dimethylthiazol-2-yl)-5-(3-carboxymethoxyphenyl)-2-(4-sulfophenyl)-2H-tetrazolium (MTS) from Promega was added to wells in columns 7-12. Plates were then placed in the incubator for 30 minutes until the first analysis. Duplicate plates allowed for eight wells in each experimental condition.

Since each plate contained fluorometric (DCFH-DA) and colorimetric (MTS) probes, two plate readers were utilized. A Thermo Scientific's Fluoroskan Ascent was used to determine the fluorescence developed as a result of the addition of DCFH-DA, while a Molecular Devices' SpectraMax 340PC384 was used to determine the color associated with the MTS probe. Plates were analyzed systematically over 24 hours. For all times outside of incubator, the microplates were kept in foil to keep out light. The pH of the plate wells was determined with a Sensorex Combination pH Electrode (½ inch in diameter) attached to a Fisher Scientific Accumet Portable pH meter.

7.3. Results

The two dust samples were predominately composed of the same mineral assemblage with quartz, calcite and feldspar representing the bulk mineralogy (Table 1). Camp Victory dust (CVD) also contained aragonite and dolomite and Fort Irwin dust also contained chlorite and illite. The elemental analysis of each dust sample did not show any anonymously high heavy metals concentrations. In fact, except for the elevated chromium and nickel concentrations in CVD, these soils are not too dissimilar from NIST standard reference material #2709A, which is a soil collected in San Joaquin Valley, California. The slightly elevated chromium and nickel levels might be related to the presence of a suite of accessory minerals derived from igneous rocks. By treating dust samples with 1 M HCl overnight and removing dissolved constituents, manganese was determined to be mostly associated with the carbonate phases in both dusts, see Table 1. The surface areas of both dust samples were high at 26.429 m^2/g and 16.335 m^2/g (CVD and FID, respectively).

CVD generated 25% the $^{\cdot}OH$ and 28% the $^{\cdot}OH+H_2O_2$ of FID when dispersed in solution for 24 hours (Figures 2 and 3). When normalized to surface area these values dropped, with CVD having generated 16 % the $^{\cdot}OH$ and 17% the $^{\cdot}OH+H_2O_2$ of FID.

The initial particle loading utilized for this study was 0.002 m^2/mL. This loading was chosen for comparison with other inflammatory stress response studies [143]. At the highest loading for this particle loading range, the greatest ISR generated by CVD was 159% of the control. FID generated an ISR 220% higher than the control. Given that there was no significant loss of cell viability the increase in ISR compared to the control was derived by the upregulation of ROS. Both of these ISR values were within the range caused by inert glass beads and anatase

[143]. Besides the standard particle loading, we also conducted a set of experiments at higher loadings to simulate the high exposure burden encountered by personnel in the Middle East theater of operations. The ISR resulting from exposure to CVD dust increased to 3,312% of the control at a particle loading of 0.05 m^2/mL (Figure 4). The ISR generated by FID dust increased to 2,433% of the control. The ISR generated by both dust samples generally increased with time and was predominately attributed to an upregulation in ROS. The ISR generated by the acid treated CVD and FID was 288 and 550% of the control, respectively, both occurring early into exposure (20 minutes and 1 hour, respectively). Unlike with the untreated dust samples, the ISR was predominately driven by necrotic cellular death.

For comparison, ISR experiments were performed on glass beads and two NIST soil standards using the elevated loading of 0.05 m^2/mL. Due to extreme loss of cell viability at the 0.05 m^2/mL loading for both NIST standards, the 0.025 m^2/mL loading was used for comparison with the dust samples. The ISR generated by the Montana NIST soil was 36,600% of the control at the 24 hour time point, progressively increasing with time (Figures 5 and 6). The ISR generated by the San Joaquin NIST soil was 2,952% of the control at the eight hour time point, and decreased to 1,954% of the control at 24 hours. The ISR values for both NIST soils were driven up both cellular ROS upregulation and extreme cell death at the highest particle loadings. The ISR generated by the inert glass beads was the highest at 8 hours (280% of the control) and exhibited only a small amount of cellular death. The ISR generated by CVD and FID at the lower loading of 0.025 m^2/mL was 1,967 and 1,412% of the control, respectively (Figure 7 and 8).

7.4. Discussion

The CVD sample investigated in this study is similar to other dust samples collected throughout the Greater Middle East; containing the same characteristic elevation in calcium carbonate respective to worldwide dust [212]. The FID, while similar to CVD, is composed of higher proportions of silica. Based on this *in vitro* technique and comparison with other standard samples, the dust is considered non-toxic in small doses. However, it must be noted that the elevated loading of 0.05 m^2/mL generates a loading of 1,982 $\mu g/m^3$, 20% the PM10 value present in a single dust storm [212, 213]. Therefore while this particle loading is elevated relative to previous ISR experiments, the total particle burden in the lungs is likely underrepresented.

The soil dust collected at Fort Irwin appears to elicit a stronger cellular response than the Iraqi soil dust, but both are far less reactive than the two soil reference materials that were also tested. Both the CVD and FID soil show little loss of cell viability. The higher ISR value for FID is likely related to the higher ROS formation in experiments with FID. While ROS formation upon dispersal in water in cell-free experiments does not always translate to ROS upregulation within epithelial cells, it is noted that FID showed a significantly higher production of ROS in water compared to CVD. However, the ISR values determined for FID and CVD are lower than those determined for either of the NIST soils when the results for the experiments with 0.025 m^2/L loadings are compared (near-complete loss of cell viability in experiments with the Montana NIST soil prevents a comparison at 0.05 m^2/L loading). For example, CVD dust generates an ISR that is twenty fold lower than that measured for the Montana soil (NIST 2710).

Besides the magnitude of the cellular response to the challenge, it is also useful to evaluate the temporal changes in ISR values. Changes in ISR over time provide insight into how cells respond to the exposure. For example, although exposure to chalcopyrite ($CuFeS_2$) leads to an significant loss of cell viability initially, the cell survival increased over time and the ISR values drop [215]. As noted above, the ISR generated by CVD was lower than the NIST soil with baseline trace elements (2709), but, unlike this NIST soil, the ISR steadily increased with time over 24 hours. This rising response indicates that the inflammation is likely to continue to increase, whereas cells challenged with the NIST 2709 manage to adapt to the challenge. Furthermore, CVD generates an ISR value that is nearly seven fold that for glass beads at their peak ISR value. Therefore, the CVD is not inert and we conclude, on the basis of the experiments described here, that the material is considered slightly cytotoxic; on par with the average natural dust or soil. It is also noted that while the majority of the ISR is generated by the carbonate phases and metals incorporated in carbonates (e.g., manganese), the origin of the ISR between the untreated and acid treated material differs. The ISR generated by the untreated dust samples is driven by the upregulation of ROS, probably related to the ROS generated by the material. Whereas the minimal ISR generated by the acid treated material is driven by cellular death, indicating other immunosuppressive properties.

The small particle size and complex morphology of CVD is likely an important contributing factor to the illnesses seen among service personnel. The specific surface area of CVD is a factor of 2.5 higher than both NIST reference materials utilized in the present study.

The fine particle size could lead to a deeper deposition of the particles in the human lung than many other soils or dusts. Furthermore, the particles appear to be aggregated into clumps. It is not clear whether this aggregation persists after deposition in the lung. Should the aggregates remain intact then many may be too large for phagocytosis. Due to the high PM_{10} values in the Greater Middle East, particle overload likely contributes to the observed illnesses and the small particle size of individual particles will exacerbate the disruption of AM-mediated phagocytosis and efferocytosis. Furthermore, the porous aggregates may harbor a plethora of bacterial, fungal and viral colonies as indicated by other work on Iraqi dust samples [213].

While only based on a single sample characteristic of the region, there is nothing unusual about the dust in terms of its chemistry, mineralogy, ability to generate ROS upon dispersal in water, or induce cellular inflammation or cytotoxicity. Given the highly elevated PM_{10} and $PM_{2.5}$ levels in the Middle East, it is likely that particle overload is the underlying cause for the health problems among United States personnel who served in Iraq; consistent with Paracelsus' postulate that the dose makes the poison [216].

7.5. Conclusions

The CVD is slightly cytotoxic and generated an ISR that increases with increasing particle loading and time. The slight inflammatory nature that exists is likely attributable to the carbonate phases and elements associated with the carbonate phases, which includes manganese. Its composition, mineralogy and morphology are non-unique and relatively inert. However, while it is possible that this dust does not represent the bulk dust present in Iraq, it is likely that the high dust exposure, and not the reactivity of the dust itself, is the hazard.

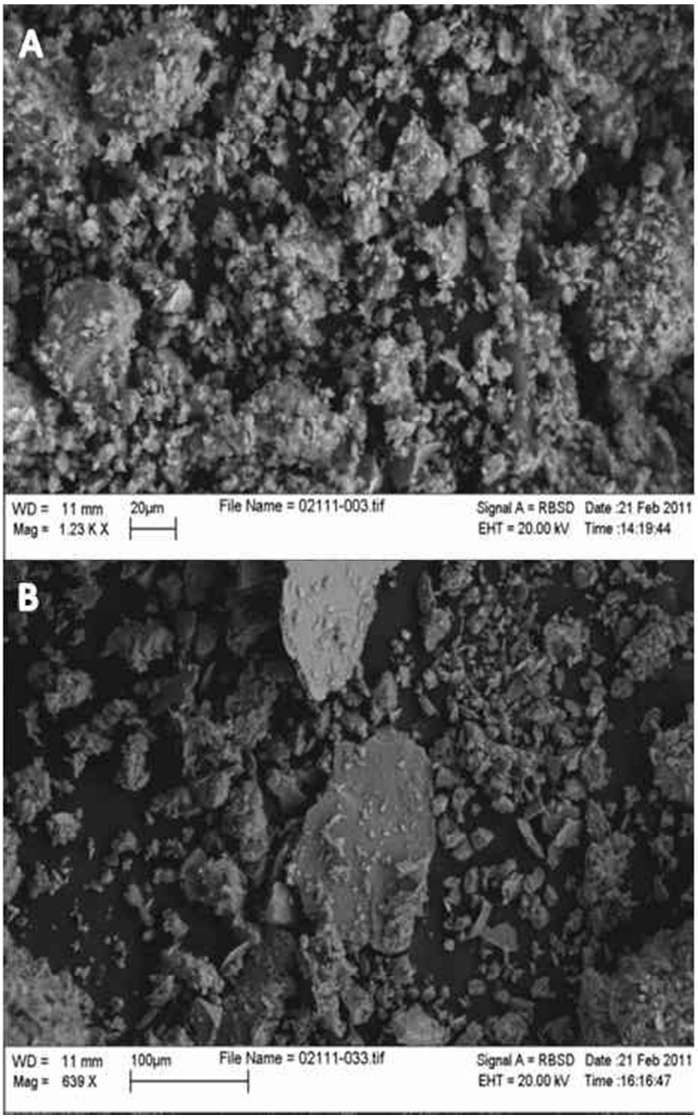

Figure 7.1. SEM images of dust samples. Scanning electron microscope images of (a) Irradiated Camp Victory, Iraq, dust and (b) Fort Irwin, CA, dust

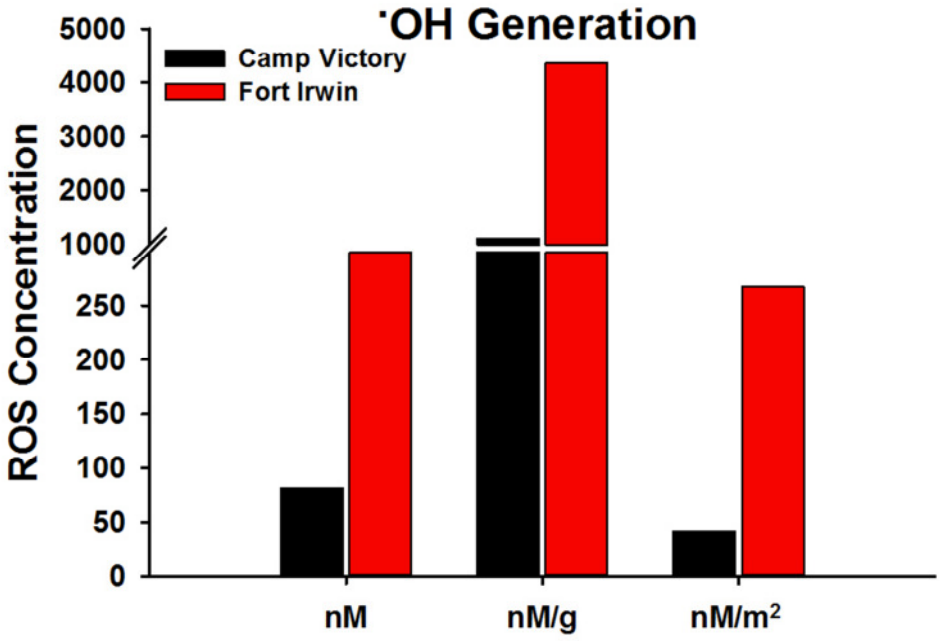

Figure 7.2. ·OH generated by dust samples. ·OH generated by Camp Victory, Iraq dust and Fort Irwin, CA dust. Concentrations are based on a 24 hour incubation in phosphate buffered solution at a pH of 7.4 with APF. Data represented as total ·OH formed and also normalized by weight and surface area of the particles.

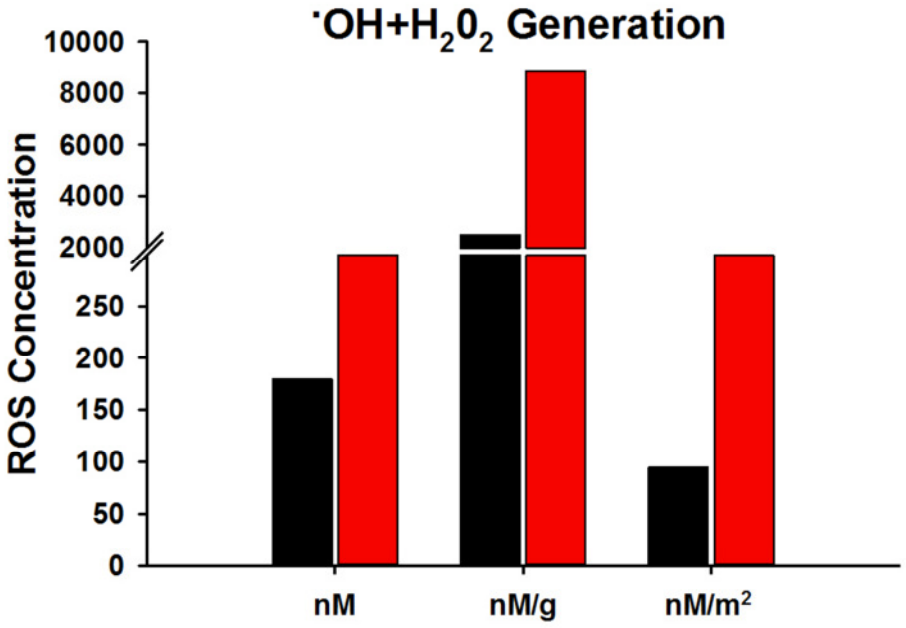

Figure 7.3. ·OH+H_2O_2 generated by dust samples. ·OH+H_2O_2 generated by Camp Victory, Iraq dust and Fort Irwin, CA dust. Concentrations based on a 24 hour incubation in phosphate buffered solution at a pH of 7.4 with APF and HRP. Data represented as total ·OH + H_2O_2 formed and also normalized by weight and surface area of the particles.

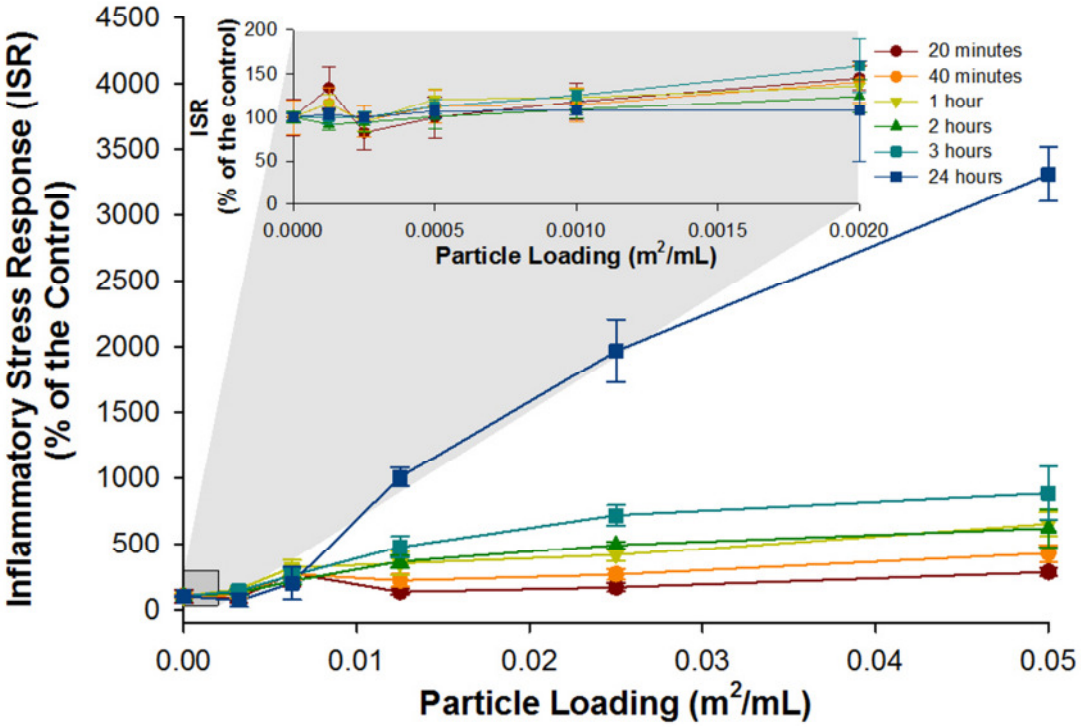

Figure 7.4. ISR of A549 cells generated by Camp Victory, Iraq dust sample. The ISR generated by Camp Victory, Iraq dust over a range of particle loadings and times points. Inset displays the ISR generated by Camp Victory dust at low particle loadings. For some data points, the error bars are hidden by the symbols.

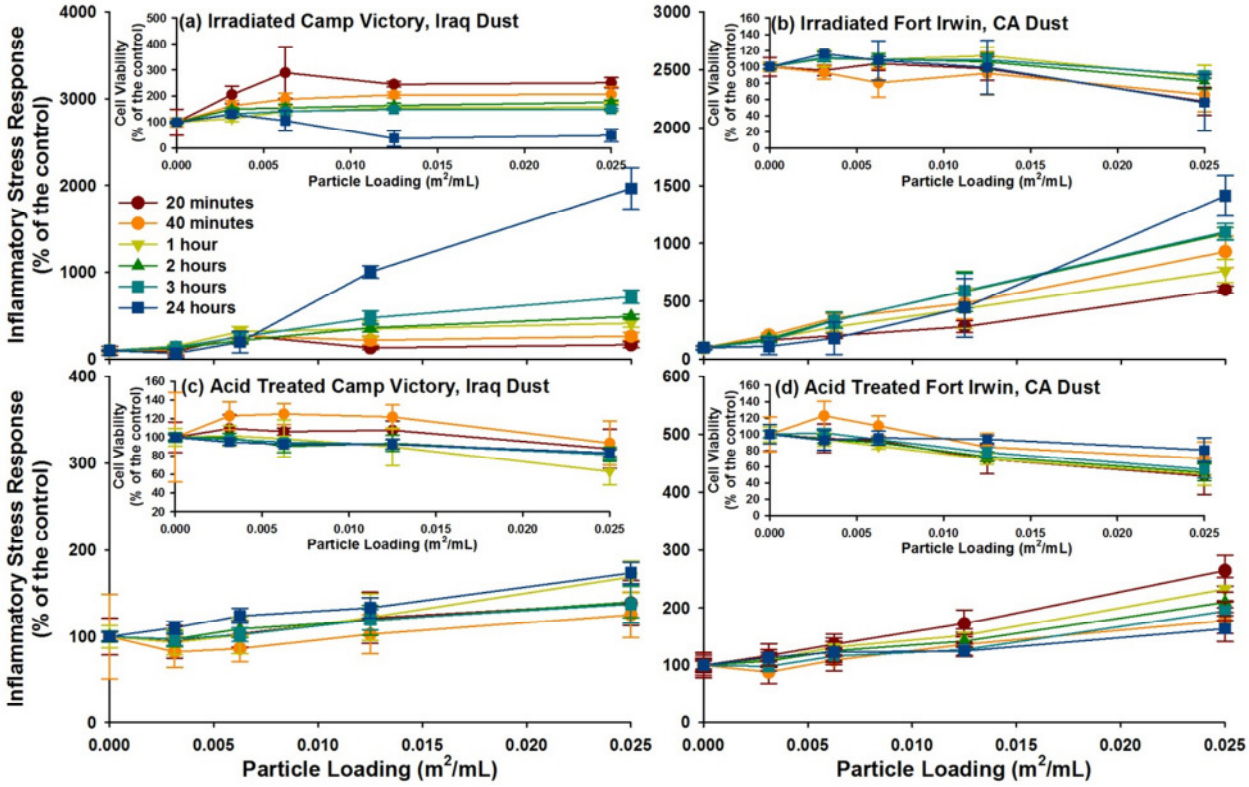

Figure 7.5. ISR of A549 cells generated by the irradiated and acid treated dust samples. ISR generated by the four study materials are represented, with the cell viability for each in the inset. (a) Irradiate Camp Victory, Iraq dust, (b) Irradiated Fort Irwin, CA dust, (c) Acid Treated Camp Victory, Iraq dust, and (d) Acid Treated Fort Irwin, CA dust. For some data point, the error bars are hidden by the symbols.

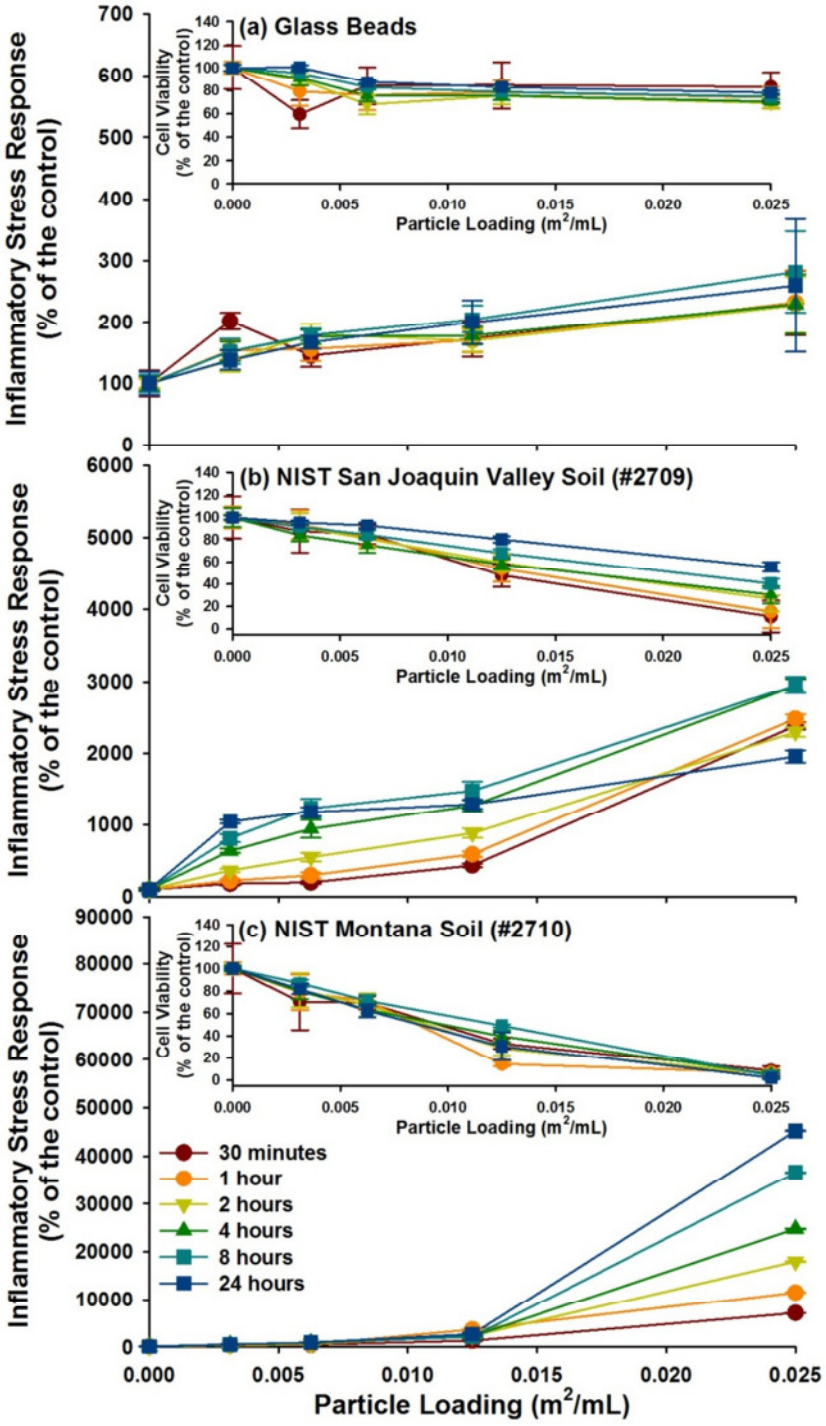

Figure 7.6. ISR of A549 cells generated by standard reference material. ISR generated by the three reference materials are represented, with the cell viability for each in the inset. (a) Glass beads, (b) NIST San Joaquin Valley soil (#2709), and (c) NIST Montana soil (#2710). For some data point, the error bars are hidden by the symbols.

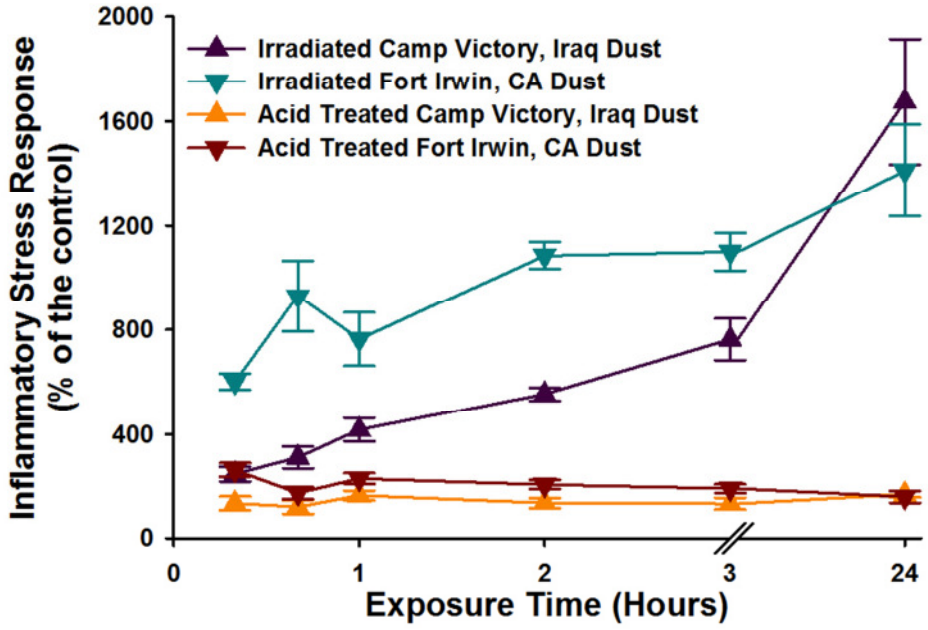

Figure 7.7. Evolution of ISR over time generated by elevated dust loadings. The temporal evolution of the ISR generated by elevated particle loadings (0.025 m^2/mL) for Camp Victory and Fort Irwin dust samples. Also represented are the dust samples there were treated with acid to remove carbonate phases. For some data points, the error bars are hidden by the symbols.

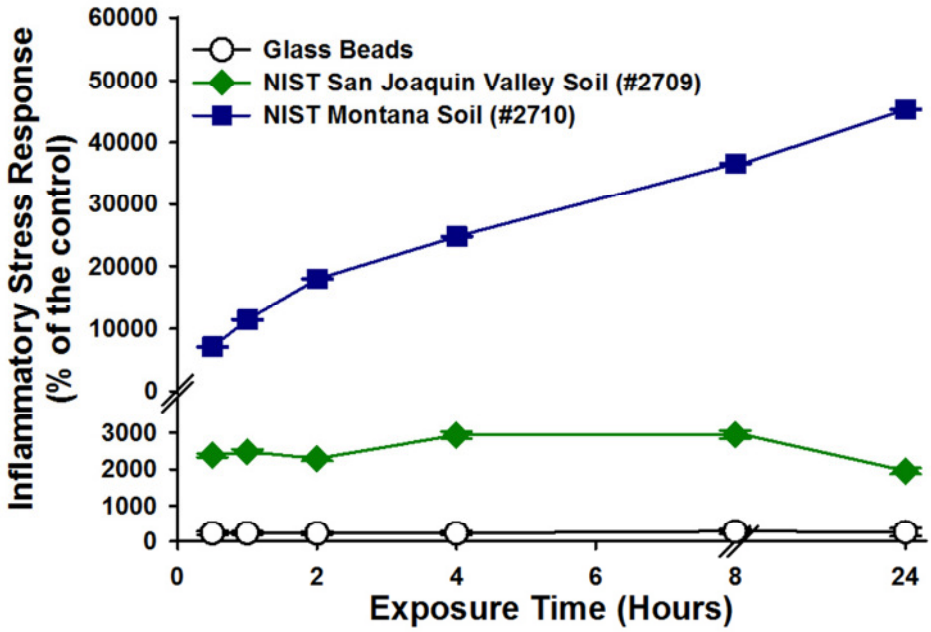

Figure 7.8. Evolution of ISR over time generated by elevated standard reference material loadings. The temporal evolution of the ISR generated by elevated particle loadings (0.025 m^2/mL) for reference material samples: glass beads, NIST San Joaquin Valley Soil (#2709) and NIST Montana Soil (#2710). For some data points, the error bars are hidden by the symbols.

Chapter 8

General Conclusions and Future Directions

When trying to determine the deleterious nature of a material, be it natural or synthetic, experiments must be performed under more complex conditions than is common when using traditional geochemical approaches. As is evidenced in Chapter 2, the modification of surface properties is possible with the mere addition of phosphate to the reaction media (water) and the addition of simple organic acids disrupts hydroxyl radical formation in solution. While the principal conclusions pertaining to pyrite's role in Coal Workers' Pneumoconiosis may not have differed if the experiments were only performed in water, the added clarification of pyrite behavior under biological conditions helped increase our understanding of disease etiology.

The addition of the inflammatory stress response (ISR) cellular experiments increased our understanding of the biological response to contaminants and Fenton metals in particular. It had been hypothesized that there would be a linear increase in ISR with increasing particle derived reactive oxygen species (ROS) production. However, while overall there is a general upward trend in ISR values with increasing particle derived ROS generation (evidenced in Chapters 3 and 4), in the end, there is no direct correlation between particle derived ROS formation and cellular ISR. There are likely two main reasons for this. If the ISR is lower than expected, it is likely that there was a change in the Fenton reaction mechanisms due to the use of more complex fluids. If higher than expected, it is likely due to the direct oxidation of biomolecules by Fenton metals. For instance, the Fenton reaction mechanism of manganese is extremely slow compared to iron and does not generate significant ROS under biologically applicable conditions over the course of 24 days (Chapter 6). Given this, no manganese derived ROS is expected to form over the 24 hours in which the ISR experiments occur (Chapter 6). However, there is significant cellular oxidative stress generated by the manganese species, indicating that the ability of manganese to directly oxidize biomolecules exceeds that of iron. The direct oxidation of biomolecules also demonstrates the ability of cells to take up manganese (and other metals) and cause other forms of dysregulation without direct ROS formation by the contaminant species. Given the complexity of the biological response to manganese and iron

alone, it can be concluded that experiments in simple aqueous solutions cannot predict the potential for a material to generate oxidative stress.

The cellular research also highlights the importance of proper normalization and controls. Given that cells generate ROS in the absence of a contaminant species, it is important to normalize the increase in cellular derived ROS caused by interaction with a contaminant species by the baseline cellular ROS formation. This normalized value is referred to as the upregulation of ROS. Furthermore, since cells will react to the mere presence of a foreign material, inert species are needed to evaluate the toxicity of reactive material. While there is no normalization to the cellular response to inert material, it offers an insight into the deleterious nature of other materials.

Besides highlighting the importance of experimental media complexity, the characterization of the materials investigated is emphasized as well. Most notable, due to its significant effect on particle reactivity and the generation of oxidative stress, is the oxidation state of the metals in mineral species. Evidenced with iron, manganese and copper, Fenton metals in their reduced state generate more ROS and also generate greater ISR values than when in their oxidized state. While Fenton chemistry is cyclic, the environment in the body is, for the most part oxidizing which limits the metals from returning to their reduced state. Apart from stability, which also relates to mineral structure, this explains why species containing trivalent iron do not generate an ISR. However, if phagocytosis occurs, the low pH of the lysosomal fluid would allow for a reducing environment which may lead to the formation of ROS.

While the reactivity of Fenton metals and their ability to generate stress in the body has long been studied, the possible exacerbation of this stress through synergistic behavior between Fenton metals has not. The natural and synthetic mixed and single metal mineral species examined generated interesting but inconclusive results. However, the importance of mineral structure is highlighted in a number of ways. The initial findings indicate there may be increased toxicity associated with copper and iron together. Nonetheless, the likelihood of surface defects on chalcopyrite and, and possibly bornite, and resulting particle derived ROS may have a greater effect on the high ISR values for these species than the presence of the two metals alone.

In a different way, the systematic investigation into the role of coupled manganese and iron has also been inconclusive. The experiments were performed with metal salts, manganese substituted goethite and hausmannite. Based on the results (Chapter 6), the role of particle

structure seems to be more important than the interactions between these two metals. While the iron in the pure goethite is stable and unreactive, the mineral structure allows for the prolonged stability of the highly reactive trivalent manganese, which is the driver for an increased ISR. Whereas, in salt solutions the toxicity of the ferrous iron dominates and there are no observable additive effects of divalent manganese. Although divalent manganese is less reactive, perhaps using a ferrous iron mineral species, such as siderite, would help clarify any synergistic behavior between the two metals. Additionally, experiments in which the divalent and trivalent mineral species are combined might help resolve the problem.

Though progressive, the research in this dissertation only represents the initial steps in investigating biological responses to geochemical processes. In order to allow for a more accurate assessment of toxicity, exposure experiments need to be performed on a wider range of cells (e.g. primary epithelial and macrophages) and on tissue samples (e.g. lung tissue of mice). The ISR method, while offering an immediate and short term assessment of a materials potential for generating oxidative stress in epithelial cells, is limited by time and relative lack of complexity. By performing *ex vivo* exposure experiments, not only can numerous exposure periods be evaluated but a more holistic biological response to a contaminant can be determined.

Apart from diversifying the exposure medium, more markers of inflammation and toxicity should be used. Lipid peroxidation experiments would complement the ISR experiments by helping to clarify the role of geomaterial (directly or indirectly) induced ROS in toxicity (Figure 8.1). For example, the presence of elevated RNS in the lungs has been implicated in COPD and their presence in exposure studies may indicate a deleterious material [1]. Additionally, the use of long standing toxicology and pharmacology techniques such as Immuno Blot Analysis and RT-PCR should be utilized in order to determine protein and DNA damage, respectively. Not only can overall protein damage be determined through Western Blot Analysis, specific proteins can be targeted which can help elucidate the origin of toxicity.

Finally, the investigation into the origin of geomaterial derived toxicity also should be examined. If the pathway to inflammation can be understood, perhaps a better treatment method could be determined. In aqueous experiments, catalase or ethanol are used to remove particle derived ROS from the solution. However, neither of these approaches is viable for cellular or tissue experiments since catalase would limit overall inflammation and ethanol would stress or even kill the cells or tissues depending on the concentration. A more viable way to determine

how a Fenton metal, or geomaterial, is harming the body could be by the use of a metal chelator, such as EDTA, although because it limits ROS production through binding, it may also limit direct biomolecule oxidations as well.

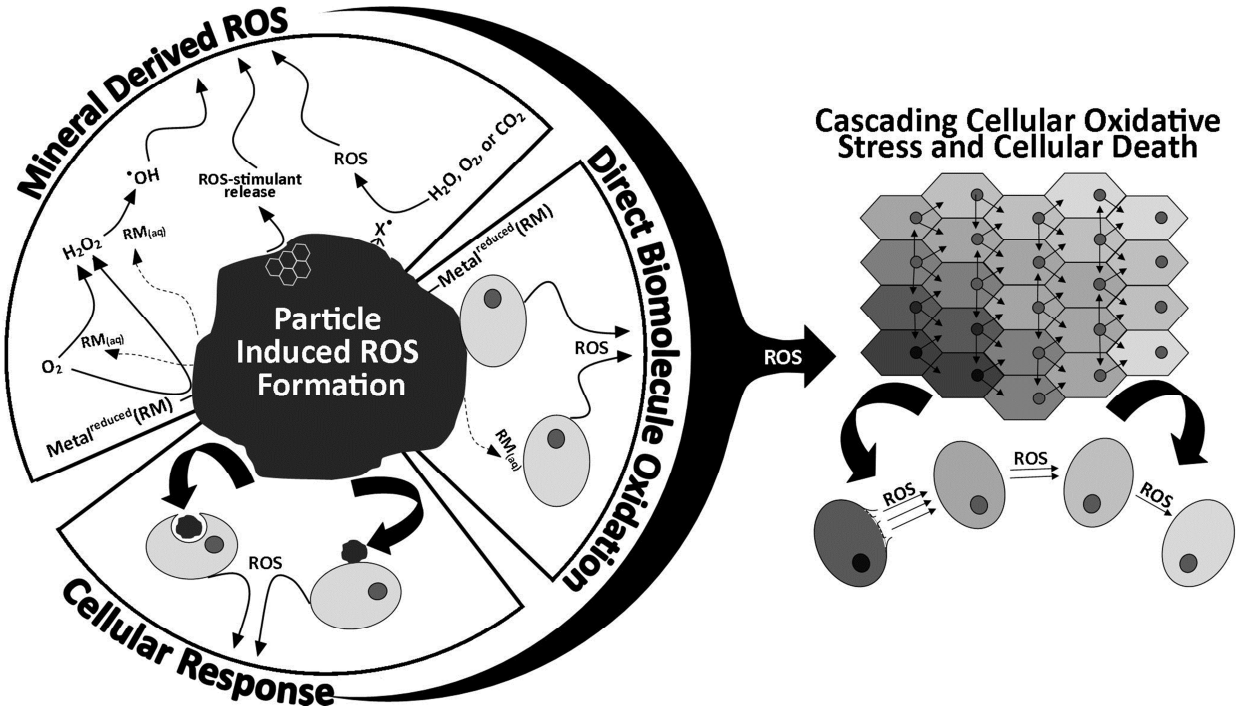

Figure 8.1. Particle Induced ROS formation. A schematic representing a particle's ability to directly and/or indirectly generate ROS in the body.

References

1. Bunnell JE, Finkelman RB, Centeno JA, Selinus O: **Medical Geology: a globally emerging discipline**. *Geol Acta* 2007, **5**(3):273-281.
2. Ramazzini B: **De morbis artificum diatriba diseases of workers . 1713**. *Am J Public Health* 2001, **91**(9):1380-1382.
3. Gochfeld M: **Chronologic history of occupational medicine**. *Journal of Occupational and Environmental Medicine* 2005, **47**(2):96-114.
4. Castranova V: **From coal mine dust to quartz: Mechanisms of pulmonary pathogenicity**. *Inhalation Toxicology* 2000, **12**:7-14.
5. Castranova V, Dalal NS, Vallyathan V: **Role of surface free radicals in the pathogenicity of silica**. Boca Raton, FL: CRC Press; 1996.
6. Castranova V, Vallyathan V: **Silicosis and coal workers' pneumoconiosis**. *Environmental Health Perspectives* 2000, **108**:675-684.
7. Castranova V, Vallyathan V, Ramsey DM, McLaurin JL, Pack D, Leonard S, Barger MW, Ma JYC, Dalal NS, Teass A: **Augmentation of pulmonary reactions to quartz inhalation by trace amounts of iron-containing particles**. *Environmental Health Perspectives* 1997, **105**:1319-1324.
8. Ding M, Dong Z, Chen F, Pack D, Ma W, Ye J, Shi X, Castranova V, Vallyathan V: **Asbestos induces activator protein-1 transactivation in transgenic mice**. *Cancer Res* 1999, **59**:1884 - 1889.
9. Finkelman RB, Orem W, Castranova V, Tatu CA, Belkin HE, Zheng BS, Lerch HE, Maharaj SV, Bates AL: **Health impacts of coal and coal use: possible solutions**. *International Journal of Coal Geology* 2002, **50**(1-4):425-443.
10. Bauer J, Mattson SM, Eastes W: **In-vitro acellular method for determining fiber durability in simulated lung fluid**. *Unpublished report* 1997, **Available electronically at: http://fiberscience.owenscorning.com/prokdis/prokdis.html.**(http://fiberscience.owenscorning.com/prokdis/prokdis.html.).
11. Cohn CA, Laffers R, Simon SR, O'Riordan T, Schoonen MAA: **Role of pyrite in formation of hydroxyl radicals in coal: possible implications for human health**. *Part Fibre Toxicol* 2006, **3**(1):16.
12. Schoonen MAA, Cohn CA, Roemer E, Laffers R, Simon SR, O'Riordan T: **Mineral-induced formation of reactive oxygen species**. In: *Medical Mineraology and Geochemistry. Volume 64*, edn.; 2006: 179-221.
13. Alessandrini F, Semmler-Behnke M, Jakob T, Schulz H, Behrendt H, Kreyling W: **Total and regional deposition of ultrafine particles in a mouse model of allergic inflammation of the lung**. *Inhalation Toxicology* 2008, **20**:585 - 593.
14. Maier KL, Alessandrini F, Beck-Speier I, Hofer TPJ, Diabate S, Bitterle E, Stoger T, Jakob T, Behrendt H, Horsch M *et al*: **Health effects of ambient particulate matter - Biological mechanisms and inflammatory responses to in vitro and in vivo particle exposures**. *Inhalation Toxicology* 2008, **20**(3):319-337.
15. Huang X, Li WH, Attfield MD, Nadas A, Frenkel K, Finkelman RB: **Mapping and prediction of coal workers' pneumoconiosis with bioavailable iron content in the bituminous coals**. *Environmental Health Perspectives* 2005, **113**(8):964-968.
16. Szema AM, Schmidt MP, Lanzirotti A, Harrington AD, Lyubsky S, Reeder RJ, Schoonen MAA: **Titanium and Iron in Lung of a Soldier With Nonspecific Interstitial Pneumonitis and Bronchiolitis After Returning From Iraq**. *Journal of Occupational and Environmental Medicine* 2012, **54**(1):1-2.

17. Jomova K, Valko M: **Advances in metal-induced oxidative stress and human disease**. *Toxicology* 2011, **283**(2–3):65-87.
18. Valko M, Morris H, Cronin MTD: **Metals, toxicity and oxidative stress**. *Curr Med Chem* 2005, **12**(10):1161-1208.
19. Fenton HJH: **Oxidation of tartaric acid in presence of iron**. *Journal of the Chemical Society, Transactions* 1894, **65**(65):899-911.
20. Haber F., Weiss J: **The catalytic decomposition of hydrogen peroxide by iron salts**. *Proceedings of the Royal Society of London, Series A* 1934, **147**:332-351.
21. Barbusinski K: **Fenton Reaction - Controversy Concerning the Chemistry**. *Ecological Chemistry and Engineering S-Chemia I Inzynieria Ekologiczna S* 2009, **16**(3):347-358.
22. Wink DA, Nims RW, Saavedra JE, Utermahlen WE, Ford PC: **The Fenton Oxidation Mechanism - Reactivities of Biologically Relevant Substrates with 2 Oxidizing Intermediates Differ from those Predicted for the Hydroxyl Radical**. *Proc Natl Acad Sci U S A* 1994, **91**(14):6604-6608.
23. Prousek J: **Fenton Reaction After a Century**. *Chemicke Listy* 1995, **89**(1):11-21.
24. Pierre JL, Fontecave M: **Iron and activated oxygen species in biology: The basic chemistry**. *Biometals* 1999, **12**(3):195-199.
25. Srivastava S, Dubey RS: **Manganese-excess induces oxidative stress, lowers the pool of antioxidants and elevates activities of key antioxidative enzymes in rice seedlings**. *Plant Growth Regul* 2011, **64**(1):1-16.
26. Kohchi C, Inagawa H, Nishizawa T, Soma GI: **ROS and Innate Immunity**. *Anticancer Research* 2009, **29**(3):817-821.
27. Knight JA: **Review: Free radicals, antioxidants, and the immune system**. *Annals of Clinical and Laboratory Science* 2000, **30**(2):145-158.
28. Ovrevik J, Hetland RB, Schins RP, Myran T, Schwarze PE: **Iron release and ROS generation from mineral particles are not related to cytokine release or apoptosis in exposed A549 cells**. *Toxicology Letters* 2006, **165**(1):31-38.
29. (USEIA) USEIA: **What is the role of coal in the United States?** *Engery in Brief - What everyone should know about energy* 2011, **http://www.eia.gov/cfapps/energy_in_brief/role_coal_us.cfm**.
30. USEIA USEIA: **International Energy Outlook**. *http://wwweiadoegov/oiaf/ieo/highlightshtml* 2009, **DOE/EIA-0484(2009)**.
31. NIOSH: **Work-Related Lung Disease Surveillance Report 2002. Cincinnati, OH**. *National Occupational Safety and Health* 2003.
32. Huang X, Fournier J, Koenig K, Chen LC: **Buffering capacity of coal and its acid-soluble Fe2+ content: Possible role in coal workers' pneumoconiosis**. *Chem Res Toxicol* 1998, **11**(7):722-729.
33. Bergman I, Casswell C: **Lung dust and lung iron contents of coal workers in different coal fields in Great Britain**. *British Journal of Industrial Medicine* 1972, **29**(2):160-168.
34. Cohn CA, Pak A, Strongin D, Schoonen MA: **Quantifying hydrogen peroxide in iron-containing solutions using leuco crystal violet**. *Geochemical Transactions* 2005, **6**(3):47-51.
35. Cohn CA, Mueller S, Wimmer E, Leifer N, Greenbaum S, Strongin DR, Schoonen MAA: **Pyrite-induced hydroxyl radical formation and its effect on nucleic acids**. *Geochemical Transactions* 2006, **7**:3-11.
36. Eastes W, Morris KJ, Morgan A, Launder KA, Collier CG, Davis JA, Mattson SM, Hadley JG: **Dissolution of glass fibers in the rat lung following intratracheal instillation**. *Inhalation Toxicology* 1995, **7**(2):197-213.
37. Mattson SM: **Glass fiber dissolution in simulated lung fluid and measures needed to improve consistency and correspondence to in vivo dissolution**. *Environmental Health Perspectives* 1994, **102**:87-90.

38. Potter RM, Mattson SM: **Glass-fiber dissolution in a physiological saline solution**. *Glastech Ber-Glass Sci Technol* 1991, **64**(1):16-28.
39. Cannon GJ, Swanson JA: **The macrophage capacity for phagocytosis**. *J Cell Sci* 1992, **101**:907-913.
40. Renwick LC, Donaldson K, Clouter A: **Impairment of Alveolar Macrophage Phagocytosis by Ultrafine Particles**. *Toxicology and Applied Pharmacology* 2001, **172**(2):119-127.
41. Morrow PE: **Possible mechanisms to explain dust overloading of the lungs**. *Fundam Appl Toxicol* 1988, **10**(3):369-384.
42. Oberdorster G: **Lung Particle Overload: Implications for Occupational Exposures to Particles**. *Regulatory Toxicology and Pharmacology* 1995, **21**(1):123-135.
43. Gamble JL: **Chemical Anatomy, Physiology, and Pathology of Extracellular Fluid: A Lecture Syllabus**, 6th edn. Cambridge, Massachusetts: Harvard Universty Press; 1942.
44. Lehuede P, deMeringo A, Bernstein DM: **Comparison of the chemical evolution of MMVF following inhalation exposure in rats and acellular in vitro dissolution**. *Inhalation Toxicology* 1997, **9**(6):495-523.
45. Wragg J, Klinck B: **The bioaccessibility of lead from Welsh mine waste using a respiratory uptake test**. *J Environ Sci Health Part A-Toxic/Hazard Subst Environ Eng* 2007, **42**(9):1223-1231.
46. de Meringo A, Morscheidt C, Thelohan S, Tiesler H: **In vitro assessment of biodurability: Acellular systems**. *Environmental Health Perspectives* 1994, **102**:47-53.
47. Berlinger B, Ellingsen DG, Naray M, Zaray G, Thomassen Y: **A study of the bio-accessibility of welding fumes**. *Journal of Environmental Monitoring* 2008, **10**(12):1448-1453.
48. Oze C, Solt K: **Biodurability of chrysotile and tremolite asbestos in simulated lung and gastric fluids**. *Am Miner* 2010, **95**(5-6):825-831.
49. Metzger R, Wichers D, Vaselin J, Velasquez P: **Solubility characterization of airborne uranium from an in situ uranium processing plant**. *Health Physics* 1997, **72**(3):418-422.
50. Jurinski JB, Rimstidt JD: **Biodurability of talc**. *Am Miner* 2001, **86**:8.
51. Kanapilly GM: **Alveolar microenvironment and its relationship to retention and transport into blood of aerosols deposited in alveoli**. *Health Physics* 1977, **32**(2):89-100.
52. Schoonen MAA, Harrington AD, Laffers R, Strongin DR: **Role of hydrogen peroxide and hydroxyl radical in pyrite oxidation by molecular oxygen** *Geochemical Cosmochemical Acta* 2010, **74**(17):4971-4987.
53. Elsetinow AR, Schoonen MAA, Strongin DR: **Aqueous geochemical and surface science investigation of the effect of phosphate on pyrite oxidation**. *Environ Sci Technol* 2001, **35**(11):2252-2257.
54. Bebie J, Schoonen MAA: **Pyrite surface interaction with selected organic aqueous species under anoxic conditions**. *Geochemical Transactions* 2000, **1**:7.
55. Schoonen MAA, Elsetinow AR, Borda M, Strongin DR: **Effect of temperature and illumination on pyrite oxidation between pH 2 and 6**. *Geochemical Transactions* 2000, **1**:23.
56. Wang LY, Castranova V, Mishra A, Chen B, Mercer RR, Schwegler-Berry D, Rojanasakul Y: **Dispersion of single-walled carbon nanotubes by a natural lung surfactant for pulmonary in vitro and in vivo toxicity studies**. *Part Fibre Toxicol* 2010, **7**.
57. Cohn CA, Pedigo CE, Hylton SN, Simon SR, Schoonen MAA: **Evaluating the use of 3 '-(p-Aminophenyl) fluorescein for determining the formation of highly reactive oxygen species in particle suspensions**. *Geochemical Transactions* 2009, **10**:8-16.
58. Dorr M, Kassbohrer J, Grunert R, Kreisel G, Brand WA, Werner RA, Geilmann H, Apfel C, Robl C, Weigand W: **A possible prebiotic formation of ammonia from dinitrogen on iron sulfide surfaces**. *Angewandte Chemie-International Edition* 2003, **42**(13):1540-1543.

59. Nair NN, Schreiner E, Marx D: **Glycine at the pyrite-water interface: The role of surface defects**. *Journal of the American Chemical Society* 2006, **128**(42):13815-13826.
60. Bebie J, Schoonen MAA, Fuhrmann M, Strongin DR: **Surface charge development on transition metal sulfides: An electrokinetic study**. *Geochimica et Cosmochimica Acta* 1998, **62**(4):633-642.
61. Ramprakash Y, Koch DFA, Woods R: **The interaction of iron species with pyrite surfaces**. *Journal of Applied Electrochemistry* 1991, **21**(6):531-536.
62. Rosso KM, Becker U, Hochella MF: **The interaction of pyrite {100} surfaces with O^{-2} and H_2O: Fundamental oxidation mechanisms**. *Am Miner* 1999, **84**:13.
63. Jaegermann W, Tributsch H: **Interfacial properties of semiconduting transition metal chalcogenides**. *Progress in Surface Science* 1988, **29**:167.
64. Parkhurst DL, Appelo CAJ: **User's guide to PHREEQC (Version 2)—A computer program for speciation, batch-reaction, one-dimensional transport, and inverse geochemical calculations**. *US Geological Survey Water-Resources Investigations Report* 1999, **99**(4259):1.
65. Taniguchi H, Fukui K, Ohnishi S, Hatano H, Hasegawa H, Maruyama T: **Free-radical intermediates in the reaction of the hydroxyl radical with amino acids**. *The Journal of Physical Chemistry* 1968, **72**(6):1926-1931.
66. Berger P, Leitner NKV, Dore M, Legube B: **Ozone and hydroxyl radicals induced oxidation of glycine**. *Water Research* 1999, **33**(2):433-441.
67. Lasaga AC: **Chemical-kinetics of water-rock interactions**. *Journal of Geophysical Research* 1984, **89**(NB6):4009-4025.
68. Seixas NS, Hewett P, Robins TG, Haney R: **Variability of particle size-specific fractions of personal coal-mine dust exposures**. *Am Ind Hyg Assoc J* 1995, **56**(3):243-250.
69. Frankie KA, Hower JC: **Variation in pyrite size, form, and microlithotype association in the Springfield (no-9) and Herrin (no-11) coals, Western Kentucky**. *International Journal of Coal Geology* 1987, **7**(4):349-364.
70. Wiese RG, Fyfe WS: **Occurences of iron sulfides in Ohio coals**. *International Journal of Coal Geology* 1986, **6**(3):251-276.
71. Cohn CA, Laffers R, Schoonen MAA: **Using yeast RNA as a probe for generation of hydroxyl radicals by earth materials**. *Environ Sci Technol* 2006, **40**(8):2838-2843.
72. Drugs.com: **Survanta**. In: *http://wwwdrugscom/pro/survantahtml*. Updated: 2011 Sepember 19; Cited 2011 September 20].
73. Rimstidt JD, Barnes HL: **The kinetics of silica-water reactions**. *Geochemical Cosmochemical Acta* 1980, **44**:17.
74. Grandstaff DE: **The dissolution rate of forsterite olivine from Hawaiian beach sand**. *Third International Symposium on Water-Rock Interaction; Proceedings* 1980:3.
75. Schott J, Berner RA, Sjoberg EL: **Mechanism of pyroxene and amphibole weathering, I, Experimental studies of iron-free minerals**. *Geochemical Cosmochemical Acta* 1981, **45**:13.
76. Fleer VN: **The dissolution kinetics of anorthite ($CaAl_2SiO_8$) and synthetic strontium feldspar ($SrAl_2Si_2O_8$) in aqueous solutions at temperatures below 100 ^oC: With applications to the geological disposal of radioactive nuclear wastes**. *PhD thesis* 1982, **Pa. State University**(University Park).
77. Plumlee GS, Ziegler TL: **The medical geochemistry of dusts, soils and other earth materials**. In: *Treatise on Geochemistry. Volume 9*, edn. Edited by Lollar SB. San Diego: Elsevier Inc.; 2004: 263-310.
78. Bunnell JE, Finkelman RB, Centeno JA, Selinus O: **Medical Geology: a globally emerging discipline**. *Geologica Acta* 2007, **5**:273-281.
79. Ross MH, Murray J: **Occupational respiratory disease in mining**. *Occupational Medicine-Oxford* 2004, **54**(5):304-310.

80. Borm PJA: **Particle toxicology: From coal mining to nanotechnology**. *Inhalation Toxicology* 2002, **14**(3):311-324.
81. Skinner CW, Ross M, Frondel C: **Asbestos and Other Fibrous Materials: Mineralogy, Chrystal Chemistry and Health Effects**. New York: Oxford University Press; 1988.
82. Skinner HCW: **The earth, source of health and hazards: An introduction to medical geology**. *Annual Review of Earth and Planetary Sciences* 2007, **35**:177-213.
83. Fubini B: **Surface reactivity in the pathogenic response to particulates**. *Environ Health Perspect* 1997, **105 Suppl 5**:1013 - 1020.
84. Davies CN: **Pneumoconiosis, Silicosis, and the Physics and Chemistry of Dust**. *Annual Review of Medicine* 1957, **8**:323-348.
85. King EJ: **Solubility Theory of Silicosis - a Critical Study**. *Occupational Medicine* 1947, **4**(1):26-49.
86. Fubini B, Hubbard A: **Reactive oxygen species (ROS) and reactive nitrogen species (RNS) generation by silica in inflammation and fibrosis**. *Free Radical Biology and Medicine* 2003, **34**(12):1507-1516.
87. Otero Areán C, Barceló F, Fenoglio I, Fubini B, Llabrés i Xamena FX, Tomatis M: **Free radical activity of natural and heat treated amphibole asbestos**. *J Inorg Biochem* 2001, **83**(2-3):211 - 216.
88. Fenoglio I, Prandi L, Tomatis M, Fubini B: **Free radical generation in the toxicity of inhaled mineral particles: the role of iron speciation at the surface of asbestos and silica**. *Redox Rep* 2001, **6**(4):235-241.
89. Vallyathan V, Shi XL, Castranova V: **Reactive oxygen species: Their relation to pneumoconiosis and carcinogenesis**. *Environmental Health Perspectives* 1998, **106**:1151-1155.
90. Kamp D, Graceffa P, Pryor W, Weitzman S: **The role of free radicals in asbestos-induced diseases**. *Free Radical Biology and Medicine* 1992, **12**:293 - 315.
91. Shi XL, Castranova V, Halliwell B, Vallyathan V: **Reactive oxygen species and silica-induced carcinogenesis**. *J Toxicol Env Health-Pt b-Crit Rev* 1998, **1**(3):181-197.
92. Schoonen MAA, Cohn CA, Roemer E, Laffers R, Simon SR, O'Riordan T: **Mineral-induced formation of reactive oxygen species**. In: *Medical Mineralogy and Geochemistry. Volume 64*, edn. Edited by Sahai N, Schoonen MAA: Mineralogical Society of America; 2006: 179-221.
93. Taniyama Y, Griendling KK: **Reactive oxygen species in the vasculature - Molecular and cellular mechanisms**. *Hypertension* 2003, **42**(6):1075-1081.
94. Poli G, Parola M: **Oxidative damage and fibrogenesis**. *Free Radical Biology and Medicine* 1997, **22**(1-2):287-305.
95. Babior BM: **Phagocytes and oxidative stress**. *American Journal of Medicine* 2000, **109**:33-44.
96. Horwell CJ, Fenoglio I, Vala Ragnarsdottir K, Sparks RSJ, Fubini B: **Surface reactivity of volcanic ash from the eruption of Soufriere Hills volcano, Montserrat, West Indies with implications for health hazards**. *Environmental Research* 2003, **93**(2):202-215.
97. Norton MR, Gunter ME: **Relationships between respiratory diseases and quartz-rich dust in Idaho, USA**. *Am Miner* 1999, **84**(7-8):1009-1019.
98. Riojas-Rodriguez H, Solis-Vivanco R, Schilmann A, Montes S, Rodriguez S, Rios C, Rodriguez-Agudelo Y: **Intellectual Function in Mexican Children Living in a Mining Area and Environmentally Exposed to Manganese**. *Environmental Health Perspectives* 2010, **118**(10):1465-1470.
99. Hong Y-C, Hwang S-S, Kim JH, Lee K-H, Lee H-J, Lee K-H, Yu S-D, D-S. K: **Metals in Particulate Pollutants Affect Peak Expiratory Flow of Schoolchildren**. *Environ Health Perspect* 2007, **115**:430–434
100. Ghio AJ, Cohen MD: **Disruption of iron homeostasis as a mechanism of biologic effect by ambient air pollution particles**. *Inhalation Toxicology* 2005, **17**:709–716.

101. Gurgueira S, Lawrence J, Coull B, Murthy G, Gonzalez- Flecha B: **Rapid increases in the steady-state concentration of reactive oxygen species in the lungs and heart after particulate air pollution inhalation**. *Environ Health Perspect* 2002, **110**:749–755.
102. Mossman BT, Churg A: **Mechanisms in the Pathogenesis of Asbestosis and Silicosis**. *Am J Respir Crit Care Med* 1998, **157**(5):1666-1680.
103. Hu W, Zhang Q, Su W, Feng Z, Rom W, Chen L, Tang M, Huang X: **Gene expression of primary human bronchial epithelial cells in response to coal dusts with different prevalence of coal workers' pneumoconiosis**. *J Toxicol Environ Health - Part A* 2003, **66**(13):1249 - 1265.
104. Cohn C, Simon S, Schoonen M: **Comparison of fluorescence-based techniques for the quantification of particle-induced hydroxyl radicals**. *Particle and Fibre Toxicology* 2008, **5**(1):2.
105. Cohn C, Laffers R, Simon S, O'Riordan T, Schoonen M: **Role of pyrite in formation of hydroxyl radicals in coal: possible implications for human health**. *Particle and Fibre Toxicology* 2006, **3**(1):16.
106. Hurowitz JA, Tosca NJ, McLennan SM, Schoonen MAA: **Production of hydrogen peroxide in Martian and lunar soils**. *Earth and Planetary Science Letters* 2007, **255**(1-2):41-52.
107. Fubini B, Mollo L, Giamello E: **Free radical generation at the solid/liquid interface in iron containing minerals**. *Free Radical Research* 1995, **23**(6):593-614.
108. Harrington AD, Hylton S, Schoonen MAA: **Pyrite-driven reactive oxygen species formation in simulated lung fluid: implications for coal workers' pneumoconiosis**. *Environmental Geochemistry and Health* 2012, **34**(4):527-538.
109. Lebel CP, Ischiropoulos H, Bondy SC: **Evaluation of the probe 2',7'-dichlorofluorescin as an indicator of reactive oxygen species formation and oxidative stress**. *Chem Res Toxicol* 1992, **5**(2):227-231.
110. Salnikow K, Su WC, Blagosklonny MV, Costa M: **Carcinogenic metals induce hypoxia-inducible factor-stimulated transcription by reactive oxygen species-independent mechanism**. *Cancer Research* 2000, **60**(13):3375-3378.
111. Rada Bz, Leto TL: **Characterization of hydrogen peroxide production by Duox in bronchial epithelial cells exposed to Pseudomonas aeruginosa**. *FEBS Letters* 2010, **584**(5):917-922.
112. Bleck B, Tse DB, Gordon T, Ahsan MR, Reibman J: **Diesel Exhaust Particle-Treated Human Bronchial Epithelial Cells Upregulate Jagged-1 and OX40 Ligand in Myeloid Dendritic Cells via Thymic Stromal Lymphopoietin**. *Journal of Immunology* 2010, **185**(11):6636-6645.
113. Bitterle E, Karg E, Schroeppel A, Kreyling W, Tippe A, Ferron G, Schmid O, Heyder J, Maier K, Hofer T: **Dose-controlled exposure of A549 epithelial cells at the air-liquid interface to airborne ultrafine carbonaceous particles**. *Chemosphere* 2006, **65**:1784 - 1790.
114. Stringer B, Imrich A, Kobzik L: **Lung epithelial cell (A549) interaction with unopsonized environmental particulates: quantitation of particle-specific binding and IL-8 production**. *Experimental Lung Research* 1996, **22**:495-508.
115. Nardone L, Andrews S: **Cell line A549 as a model of the type II pneumocyte. Phospholipid biosynthesis from native and organometallic precursors**. *Biochim Biophys Acta* 1979, **573**:276-295.
116. Giard D, Aaronson S, Todaro G, Arnstein P, Kersey J, Dosik H, Parks W: **In vitro cultivation of human tumors: establishment of cell lines derived from a series of solid tumors**. *Journal of the National Cancer Institute* 1973, **51**:1417-1423.
117. Tan DF, Zander DS: **Immunohistochemistry for Assessment of Pulmonary and Pleural Neoplasms: A Review and Update**. *International Journal of Clinical and Experimental Pathology* 2008, **1**(1):19-31.
118. (UMMC) UoMMC: **Respiratory Disease - Lung Cancer**. In.: University of Maryland Medical Center; 2011.

119. Huang X, Frenkel K, Klein CB, Costa M: **Nickel Induces Increased Oxidants in Intact Cultured Mammalian Cells as Detected by Dichlorofluorescein Fluorescence**. *Toxicology and Applied Pharmacology* 1993, **120**(1):29-36.
120. Zhang WY, Qiao TK, Zha L: **Inhibition of Heme Oxygenase-1 Enhances the Radiosensitivity in Human Nonsmall Cell Lung Cancer A549 Cells**. *Cancer Biother Radiopharm* 2011, **26**(5):639-645.
121. Lison D, Lardot C, Huaux F, Zanetti G, Fubini B: **Influence of particle surface area on the toxicity of insoluble manganese dioxide dusts**. *Archives of Toxicology* 1997, **71**(12):725-729.
122. Sager T, Castranova V: **Surface area of particle administered versus mass in determining the pulmonary toxicity of ultrafine and fine carbon black: comparison to ultrafine titanium dioxide**. *Part Fibre Toxicol* 2009, **6**(1):15.
123. Duffin R, Tran CL, Clouter A, Brown DM, MacNee W, Stone V, Donaldson K: **The Importance of Surface Area and Specific Reactivity in the Acute Pulmonary Inflammatory Response to Particles**. *Ann Occup Hyg* 2002, **46**(Supplement 1):242-245.
124. Lundholt BK, Scudder KM, Pagliaro L: **A simple technique for reducing edge effect in cell-based assays**. *Journal of Biomolecular Screening* 2003, **8**(5):566-570.
125. **Cell Viability** [http://www.promega.com/resources/product-guides-and-selectors/protocols-and-applications-guide/cell-viability/]
126. Panduri V, Weitzman SA, Chandel N, Kamp DW: **The mitochondria-regulated death pathway mediates asbestos-induced alveolar epithelial cell apoptosis**. *American journal of respiratory cell and molecular biology* 2003, **28**(2):241-248.
127. Sulaymon AH, Ebrahim SE: **Saving amberlite XAD4 by using inert material in adsorption process**. *Desalin Water Treat* 2010, **20**(1-3):234-242.
128. Schins RPF, Duffin R, Hohr D, Knaapen AM, Shi TM, Weishaupt C, Stone V, Donaldson K, Borm PJA: **Surface modification of quartz inhibits toxicity, particle uptake, and oxidative DNA damage in human lung epithelial cells**. *Chem Res Toxicol* 2002, **15**(9):1166-1173.
129. Totsuka Y, Higuchi T, Imai T, Nishikawa A, Nohmi T, Kato T, Masuda S, Kinae N, Hiyoshi K, Ogo S *et al*: **Genotoxicity of nano/microparticles in in vitro micronuclei, in vivo comet and mutation assay systems**. *Part Fibre Toxicol* 2009, **6**(1):23.
130. Stringer B, Kobzik L: **Environmental particulate-mediated cytokine production in lung epithelial cells (A549): Role of preexisting inflammation and oxidant stress**. *Journal of Toxicology and Environmental Health-Part a-Current Issues* 1998, **55**(1):31-44.
131. Jin C, Tang Y, Yang FG, Li XL, Xu S, Fan XY, Huang YY, Yang YJ: **Cellular Toxicity of TiO(2) Nanoparticles in Anatase and Rutile Crystal Phase**. *Biol Trace Elem Res* 2011, **141**(1-3):3-15.
132. Hsiao IL, Huang YJ: **Effects of various physicochemical characteristics on the toxicities of ZnO and TiO(2) nanoparticles toward human lung epithelial cells**. *Sci Total Environ* 2011, **409**(7):1219-1228.
133. Schoonen MAA, Harrington AD, Laffers RA, Strongin DR: **Role of hydrogen peroxide and hydroxyl radical in pyrite oxidation by molecular oxygen**. *Geochimica Et Cosmochimica Acta* 2010, **74**(17):4971-4987.
134. Borda MJ, Strongin DR, Schoonen MA: **A vibrational spectroscopic study of the oxidation of pyrite by ferric iron**. *American Mineralogist* 2003, **88**:1318-1323.
135. Borda MJ, Strongin DR, Schoonen MA: **A vibrational spectroscopic study of the oxidation of pyrite by molecular oxygen**. *Geochimica Et Cosmochimica Acta* 2004, **68**(8):1807-1813.
136. NIST: **Certificate of Analysis - Standard Reference Material 2709 (San Joaquin Soil)**. In. Edited by Commerce Do. Washington, D.C.: National Institute of Standards & Technology; 2002: 3.
137. NIST: **Certificate of Analysis - Standard Reference Materail 2710 (Montana Soil)**. In. Edited by Commerce Do. Washington, D.C.: National Institute of Standards & Technology; 2002: 3.

138. Rosso KM, Becker U, Hochella MF: **Atomically resolved electronic structure of pyrite {100} surfaces: An experimental and theoretical investigation with implications for reactivity**. *Am Miner* 1999, **84**(10):1535-1548.
139. Biegler T, Rand DAJ, Woods R: **Oxygen reduction on sulphide minerals: Part I. Kinetics and mechanism at rotated pyrite electrodes**. *Journal of Electroanalytical Chemistry and Interfacial Electrochemistry* 1975, **60**(2):151-162.
140. Moses CO, Herman JS: **Pyrite oxidation at circumneutral pH**. *Geochimica et Cosmochimica Acta* 1991, **55**(2):471-482.
141. Moses C, Nordstrom D, Herman J, Mills A: **Aqueous pyrite oxidation by dissolved oxygen and by ferric iron**. *Geochimica Cosmochimica Acta* 1987, **51**:161 - 1572.
142. Martin TR, Frevert CW: **Innate Immunity in the Lungs**. *Proceedings of the American Thoracic Society* 2005, **2**(5):403-411.
143. Harrington AD, Tsirka SE, A.A. SM: **Quantification of particle-induced inflammatory stress response: a novel approach for toxicity testing of earth materials**. *Geochemical Transactions* 2012, **13**(4).
144. Spector A: **Review: Oxidative stress and disease**. *Journal of Ocular Pharmacology and Therapeutics* 2000, **16**(2):193-201.
145. NIST: **Certificate of Analysis - Standard Reference Material 1635**. In. Edited by Commerce Do. Gaithersburg: National Institute of Standards & Technology; 2008.
146. NIST: **Certificate of Analysis - Standard Reference Material 2684b**. In. Edited by Commerce Do. Gaithersburg: National Institute of Standards & Technology; 2010.
147. NIST: **Certificate of Analysis - Standard Reference Material 2685b**. In. Edited by Commerce Do. Gaithersburg: National Institute of Standards & Technology; 2007.
148. NIST: **Certificate of Analysis - Standard Reference Material 2692b**. In. Edited by Commerce Do. Gaithersburg: National Institute of Standards & Technology; 2007.
149. NIST: **Certificate of Analysis - Standard Reference Material 2682b**. In. Edited by Commerce Do. Gaithersburg: National Institute of Standards & Technology; 2007.
150. MJO MJO: **Mining Explained**. In: *Knowledge.* Edited by Obasanya A: Aspermont Media; 2012.
151. Winterbourn CC: **Toxicity of iron and hydrogen peroxide: the Fenton reaction**. *Toxicology Letters* 1995, **82–83**(0):969-974.
152. Labrenz M, Druschel GK, Thomsen-Ebert T, Gilbert B, Welch SA, Kemner KM, Logan GA, Summons RE, Stasio GD, Bond PL *et al*: **Formation of Sphalerite (ZnS) Deposits in Natural Biofilms of Sulfate-Reducing Bacteria**. *Science* 2000, **290**(5497):1744-1747.
153. Wright K, Gale JD: **A first principles study of the distribution of iron in sphalerite**. *Geochimica et Cosmochimica Acta* 2010, **74**(12):3514-3520.
154. Di Benedetto F, Andreozzi GB, Bernardini GP, Borgheresi M, Caneschi A, Cipriani C, Gatteschi D, Romanelli M: **Short-range order of Fe2+ in sphalerite by Fe-57 Mossbauer spectroscopy and magnetic susceptibility**. *Physics and Chemistry of Minerals* 2005, **32**(5-6):339-348.
155. Pattrick RAD, Mosselmans JFW, Charnock JM: **An x-ray absorption study of doped sphalerites**. *European Journal of Mineralogy* 1998, **10**(2):239-249.
156. Asta MP, Cama J, Ayora C, Acero P, de Giudici G: **Arsenopyrite dissolution rates in O2-bearing solutions**. *Chemical Geology* 2010, **273**(3–4):272-285.
157. Goh SW, Buckley AN, Lamb RN, Rosenberg RA, Moran D: **The oxidation states of copper and iron in mineral sulfides, and the oxides formed on initial exposure of chalcopyrite and bornite to air**. *Geochimica et Cosmochimica Acta* 2006, **70**(9):2210-2228.
158. Todd EC, Sherman DM, Purton JA: **Surface oxidation of chalcopyrite (CuFeS2) under ambient atmospheric and aqueous (pH 2-10) conditions: Cu, Fe L- and O K-edge X-ray spectroscopy**. *Geochimica et Cosmochimica Acta* 2003, **67**(12):2137-2146.

159. Ghiazza M, Scherbart AM, Fenoglio I, Grendene F, Turci F, Martra G, Albrecht C, Schins RPF, Fubini B: **Surface Iron Inhibits Quartz-Induced Cytotoxic and Inflammatory Responses in Alveolar Macrophages**. *Chem Res Toxicol* 2011, **24**(1):99-110.
160. Gloyne LS, Grant GD, Perkins AV, Powell KL, McDermott CM, Johnson PV, Anderson GJ, Kiefel M, Anoopkumar-Dukie S: **Pyocyanin-induced toxicity in A549 respiratory cells is causally linked to oxidative stress**. *Toxicology in Vitro* 2011, **25**(7):1353-1358.
161. Araujo J, Nel A: **Particulate matter and atherosclerosis: role of particle size, composition and oxidative stress**. *Part Fibre Toxicol* 2009, **6**(1):24.
162. Schmidt EP, Tuder RM: **Role of Apoptosis in Amplifying Inflammatory Responses in Lung Diseases**. *Journal of Cell Death* 2010, **3**(2178-JCD-Role-of-Apoptosis-in-Amplifying-Inflammatory-Responses-in-Lung-Disease.pdf):41-53.
163. Hodge S, Hodge G, Scicchitano R, Reynolds PN, Holmes M: **Alveolar macrophages from subjects with chronic obstructive pulmonary disease are deficient in their ability to phagocytose apoptotic airway epithelial cells**. *Immunology and Cell Biology* 2003, **81**(4):289-296.
164. Nanji AA, Hiller-Sturmhofel S: **Apoptosis and necrosis - Two types of cell death in alcoholic liver disease**. *Alcohol Health & Research World* 1997, **21**(4):325-330.
165. Kida H, Yoshida M, Hoshino S, Inoue K, Yano Y, Yanagita M, Kumagai T, Osaki T, Tachibana I, Saeki Y *et al*: **Protective effect of IL-6 on alveolar epithelial cell death induced by hydrogen peroxide**. *American Journal of Physiology-Lung Cellular and Molecular Physiology* 2005, **288**(2):L342-L349.
166. Antonini JM, Roberts JR, Stone S, Chen BT, Schwegler-Berry D, Frazer DG: **Short-Term Inhalation Exposure to Mild Steel Welding Fume had no Effect on Lung Inflammation and Injury but did Alter Defense Responses to Bacteria in Rats**. *Inhalation Toxicology* 2009, **21**(3):182-192.
167. Chamnongpol S, Dodson W, Cromie MJ, Harris ZL, Groisman EA: **Fe(III)-mediated cellular toxicity**. *Molecular Microbiology* 2002, **45**(3):711-719.
168. Yoo KC, Yoon CH, Kwon D, Hyun KH, Woo SJ, Kim RK, Lim EJ, Suh Y, Kim MJ, Yoon TH *et al*: **Titanium dioxide induces apoptotic cell death through reactive oxygen species-mediated Fas upregulation and Bax activation**. *Int J Nanomed* 2012, **7**:1203-1214.
169. Fleury C, Mignotte B, Vayssiere JL: **Mitochondrial reactive oxygen species in cell death signaling**. *Biochimie* 2002, **84**(2-3):131-141.
170. Aneja VP, Isherwood A, Morgan P: **Characterization of particulate matter (PM10) related to surface coal mining operations in Appalachia**. *Atmospheric Environment* 2012, **54**:496-501.
171. George KV, Patil DD, Alappat BJ: **PM10 in the ambient air of Chandrapur coal mine and its comparison with other environments**. *Environmental Monitoring and Assessment* 2013, **185**(2):1117-1128.
172. Strlic M, Kolar J, Selih VS, Kocar D, Pihlar B: **A comparative study of several transition metals in Fenton-like reaction systems at circum-neutral pH**. *Acta Chimica Slovenica* 2003, **50**(4):619-632.
173. De Giudici G, Zuddas P: **In situ investigation of galena dissolution in oxygen saturated solution: evolution of surface features and kinetic rate**. *Geochimica et Cosmochimica Acta* 2001, **65**(9):1381-1389.
174. Pettersson HM, Pietras A, Persson MM, Karlsson J, Johansson L, Shoshan MC, Pahlman S: **Arsenic trioxide is highly cytotoxic to small cell lung carcinoma cells**. *Molecular Cancer Therapeutics* 2009, **8**(1):160-170.
175. Klaassen C, Watkins JBI: **Casarett & Doull's Essentials of Toxicology**, 2nd edn: McGraw-Hill 2010.
176. Roussel RR, Barchowsky A: **Arsenic inhibits NF-kappa B-mediated gene transcription by blocking I kappa B kinase activity and I kappa B alpha phosphorylation and degradation**. *Archives of Biochemistry and Biophysics* 2000, **377**(1):204-212.

177. Borm P: **Particle toxicology: from coal mining to nanotechnology**. *Inhal Toxicol* 2002, **14**:311 - 324.
178. Barbeau A: **Manganese and extrapyramidal disorders (A critical review and tribute to Dr. George C. Cotzias)**. *Neurotoxicology* 1984, **5**(1):13-35.
179. Mena I, Marin O, Fuenzali.S, Cotzias GC: **Chronic manganese poisoning - Clinical picture and manganese turnover**. *Neurology* 1967, **17**(2):128-&.
180. Crossgrove J, Zheng W: **Manganese toxicity upon overexposure**. *Nmr in Biomedicine* 2004, **17**(8):544-553.
181. Torres-Agustín R, Rodríguez-Agudelo Y, Schilmann A, Solís-Vivanco R, Montes S, Riojas-Rodríguez H, Cortez-Lugo M, Ríos C: **Effect of environmental manganese exposure on verbal learning and memory in Mexican children**. *Environmental Research* 2013, **121**(0):39-44.
182. Woolf A, Wright R, Amarasiriwardena C, Bellinger D: **A child with chronic manganese exposure from drinking water**. *Environmental Health Perspectives* 2002, **110**(6):613-616.
183. Dastur DK, Manghani DK, Raghaven.Kv: **Distribution and fate of 54Mn in Monkey - Studies of different parts of central nervous system and other organs**. *Journal of Clinical Investigation* 1971, **50**(1):9-&.
184. Hudnell HK: **Effects from environmental Mn exposures: A review of the evidence from non-occupational exposure studies**. *Neurotoxicology* 1999, **20**(2-3):379-397.
185. Lynam DR, Roos JW, Pfeifer GD, Fort BF, Pullin TG: **Environmental effects and exposures to manganese from use of methylcyclopentadienyl manganese tricarbonyl (MMT) in gasoline**. *Neurotoxicology* 1999, **20**(2-3):145-150.
186. Ferraz HB, Bertolucci PHF, Pereira JS, Lima JGC, Andrade LAF: **Chronic exposure to the fungicide Maneb my produce symptoms and signs of CNS manganese intoxication**. *Neurology* 1988, **38**(4):550-553.
187. Ensing JG: **Bazooka - Cocaine-base and manganese carbonate**. *Journal of Analytical Toxicology* 1985, **9**(1):45-46.
188. Cox PA: **The Elements on Earth: Inorganic Chemistry in the Environment**. New York: Oxford University Press; 1995.
189. Xia T, Kovochich M, Brant J, Hotze M, Sempf J, Oberley T, Sioutas C, Yeh JI, Wiesner MR, Nel AE: **Comparison of the abilities of ambient and manufactured nanoparticles to induce cellular toxicity according to an oxidative stress paradigm**. *Nano Letters* 2006, **6**(8):1794-1807.
190. Gurr JR, Wang ASS, Chen CH, Jan KY: **Ultrafine titanium dioxide particles in the absence of photoactivation can induce oxidative damage to human bronchial epithelial cells**. *Toxicology* 2005, **213**(1-2):66-73.
191. Group IETE: **Toxicity and Health Effects of Chromium (All Oxidation States)**. In: *Chromium (VI) Handbook.* edn. Edited by Guertin J, Jacobs JA, Avakian CP. Boca Raton: CRC Press; 2004: 213-232.
192. Reeder RJ, Schoonen MAA, Lanzirotti A: **Metal speciation and its role in bioaccessibility and bioavailability**. *Medical Mineraology and Geochemistry* 2006, **64**:59-113.
193. Sawyer DT: **Metal Fe(II), Cu(I), Co(II), Mn(III) hydroperoxide-induced activation of dioxygen (center dot O-2 center dot) for the ketonization of hydrocarbons: oxygenated Fenton Chemistry**. *Coordination Chemistry Reviews* 1997, **165**:297-313.
194. Stiers W, Schwertmann U: **Evidence for manganese substitution in synthetic goethite**. *Geochimica et Cosmochimica Acta* 1985, **49**(9):1909-1911.
195. Blume HP, Schwertm.U: **Genetic evaluation of profile distribution of aluminum, iron, and manganese oxides**. *Soil Science Society of America Proceedings* 1969, **33**(3):438-&.
196. McLennan SM, Taylor SR: **Earth's Continental Crust**. In: *Encyclopedia of Geochemistry.* Edited by Fairbridge CPMaRW. Dordrecht: Kluwer Academic; 1999: 145 - 151.

197. Cohn CA, Fisher SC, Brownawell BJ, Schoonen MAA: **Adenine oxidation by pyrite-generated hydroxyl radicals**. *Geochemical Transactions* 2010, **11**.
198. Simandan T, Sun J, Dix TA: **Oxidation of DNA bases, deoxyribonucleosides and homopolymers by peroxyl radicals**. *Biochemical Journal* 1998, **335**:233-240.
199. Kamiya H: **Mutagenic potentials of damaged nucleic acids produced by reactive oxygen/nitrogen species: approaches using synthetic oligonucleotides and nucleotides**. *Nucleic Acids Research* 2003, **31**(2):517-531.
200. Setsukinai K, Urano Y, Kakinuma K, Majima H, Nagano T: **Development of novel fluorescence probes that can reliably detect reactive oxygen species and distinguish different species**. *J Biol Chem* 2003, **278**:3170 - 3175.
201. Fisher SC: **Phenylalanine as a probe for mineral-mediated hydroxyl radical formation**. Stony Brook: Stony Brook University; 2012.
202. Anderson GM, Crerar DA: **Thermodynamics in Geochemistry: The Equilibrium Model**. New York: Oxford University Press, Inc.; 1993.
203. Chen JY, Tsao GC, Zhao QQ, Zheng W: **Differential cytotoxicity of Mn(II) and Mn(III): Special reference mitochondrial Fe-S containing enzymes**. *Toxicology and Applied Pharmacology* 2001, **175**(2):160-168.
204. Zong W-X, Thompson CB: **Necrotic death as a cell fate**. *Genes & Development* 2006, **20**(1):1-15.
205. Martin ST: **Precipitation and dissolution of iron and manganese oxides**: CRC Press; 2005.
206. Bowman AB, Kwakye GF, Herrero Hernández E, Aschner M: **Role of manganese in neurodegenerative diseases**. *Journal of Trace Elements in Medicine and Biology* 2011, **25**(4):191-203.
207. Szema AM, Salihi W, Savary K, Chen JJ: **Respiratory Symptoms Necessitating Spirometry Among Soldiers With Iraq/Afghanistan War Lung Injury**. *Journal of Occupational and Environmental Medicine* 2011, **53**(9):961-965.
208. Kilpatrick ME: **Deputy Director for Force Health Protection and Readiness Programs in the Office of the Assistant Secretary of Defense for Health Affairs**. In. Edited by Szema AM; 2011.
209. Vandivier RW, Henson PM, Douglas IS: **Burying the Dead*The Impact of Failed Apoptotic Cell Removal (Efferocytosis) on Chronic Inflammatory Lung Disease**. *CHEST Journal* 2006, **129**(6):1673-1682.
210. **Country Studies** [http://countrystudies.us/]
211. **World Development Indictors: Average precipitation in depth (mm per year)** [http://data.worldbank.org/indicator/AG.LND.PRCP.MM]
212. Engelbrecht JP, McDonald EV, Gillies JA, Jayanty RKM, Casuccio G, Gertler AW: **Characterizing Mineral Dusts and Other Aerosols from the Middle EastPart 1: Ambient Sampling**. *Inhalation Toxicology* 2009, **21**(4):297-326.
213. Lyles MB, Fredrickson HL, Bednar AJ, Fannin HB, Griffin D, Sobecki TM: **Medical geology: Dust exposure and potential health risks in the Middle East**. *Geochimica Et Cosmochimica Acta* 2008, **72**(12):A576-A576.
214. Park JW, Lim YH, Kyung SY, An CH, Lee SP, Jeong SH, Ju YS: **Effects of ambient particulate matter on peak expiratory flow rates and respiratory symptoms of asthmatics during Asian dust periods in Korea**. *Respirology* 2005, **10**(4):470-476.
215. Harrington AD, Smirnov A, Tsirka SE, A.A. SM: **Metal-Sulfide Mineral Ores, Fenton Chemistry and Disease – Particle Induced Inflammatory Stress Response in Lung Cells**. *Geochemical Cosmochemical Acta* Submitted.
216. Frank P, Ottoboni MA: **The Dose Makes the Poison: A Plain-Language Guide to Toxicology**, 3 edn. Hoboken: John Wiley & Sons, Inc.; 2011.

217. Ichinose M, Sugiura H, Yamagata S, Koarai A, Shirato K: **Increase in reactive nitrogen species production in chronic obstructive pulmonary disease airways**. *American Journal of Respiratory and Critical Care Medicine* 2000, **162**(2):701-706.